Mechanistic Insights and Improvements in Expansion Microscopy

Inaugural-Dissertation

to obtain the academic degree

Doctor rerum naturalium (Dr. rer. nat.)

submitted to the Department of Biology, Chemistry, Pharmacy
of Freie Universität Berlin

by

Ria Thielhorn

January 2024

This doctorate study was conducted from June 2019 to January 2024 under the supervision of Prof. Dr. Helge Ewers in the department of Biology, Chemistry and Pharmacy of the Freie Universität Berlin.

1st Reviewer: Prof. Dr. Helge Ewers, Freie Universität Berlin
2nd Reviewer: Prof. Dr. Francesca Bottanelli, Freie Universität Berlin

Date of defense: 29.05.2024

Declaration of independent work

Herewith I certify that I have prepared and written my thesis independently and that I have not used any sources and aids other than those indicated by me.

_____

Abstract

Super-resolution microscopy enables the observation of structures below the diffraction limit of light. A relatively new method, Expansion Microscopy (ExM) involves physically expanding a hydrogel-embedded facsimile of a biological structure by tearing it apart. The resultant larger replica permits sub-diffraction imaging with a typical fluorescent microscope. However, there are challenges, such as retaining the fluorescent signal after expansion and the isotropic nature of the expansion procedure, which this study will address. The signal loss is due to the loss of labels, which is mainly caused by gel formation and digestion. To address this issue, an agent was developed in this study that combines targeting, fluorescent labeling, and gel linkage into a single small molecule. The findings presented here suggest that label loss is due to inadequate surface grafting of fluorophores into the hydrogel. In order to gain a mechanistic understanding of dye retention, it is crucial to understand the function of surface grafting in ExM. By delivering monomers directly to the target of interest via nanobodies, the amount of polymerizable units bound to the surface was increased, resulting in retention of the signal. Consequently, the density of local monomers is crucial for retaining signals. In addition to signal retention, it is essential to verify that the expansion was uniform in all directions, i.e. isotropic, since only a facsimile of the original biological structure is detected after expansion. This is necessary to draw accurate conclusions from the results. Therefore, my goal was to develop a ruler that measures the isotropy of the expansion. For this experiment, tobacco mosaic virus (TMV) particles were fluorescently labeled and introduced as an internal standard into cells by coupling them with microtubules. However, the distribution of particle lengths and the loss of signal after expansion proved to be problematic. These obstacles can be resolved in future research. A uniform virus length could be achieved through size exclusion chromatography. Secondly, signal retention could be improved by fluorescently labeling additional amino acids of TMV coat proteins (CPs) and providing particles with polymerizable groups.

Zusammenfassung

Die superauflösende Mikroskopie ermöglicht die Beobachtung von Strukturen unterhalb der Beugungsgrenze des Lichts. Die Expansionsmikroskopie (ExM) ist eine vergleichsweise neue Methode, bei der ein Hydrogel verwendet wird, um eine biologische Struktur zu expandieren. Hierbei werden die Proteine physikalisch auseinander gezogen. Als Ergebnis entsteht ein größeres Faksimile, welches mit einem herkömmlichen beugungsbegrenzten Mikroskop abgebildet werden kann. Herausforderungen der Methode sind die Signalerhaltung der fluoreszenzmarkierten Strukturen nach der Expansion und die isotrope Natur des Expansionsprozesses, die in dieser Studie untersucht werden. Der Signalverlust ist auf den Verlust von Markierungen zurückzuführen, der hauptsächlich durch Gelbildung und Verdauung verursacht wird. Um dieses Problem zu lösen, haben wir ein kleines Molekül entwickelt, das Zielgerichtetheit, Fluoreszenzmarkierung und Gelverknüpfung vereint. Die Ergebnisse dieser Studie legen nahe, dass der Mangel an Markierungen auf eine unzureichende Pfropfung der Fluorophore auf der Oberfläche des Hydrogels zurückzuführen ist. Für ein mechanistisches Verständnis der Farbstoffretention ist es von entscheidender Bedeutung, die Funktion der Oberflächenpfropfung in ExM zu verstehen. Durch die direkte Lieferung von Monomeren über Nanokörper an die Zielstruktur konnte die Menge der Oberflächen-gebundenen polymerisierbaren Einheiten erhöht werden, was die Signalretention zur Folge hatte. Hierfür ist folglich die Dichte der lokalen Monomere entscheidend. Außerdem ist es wichtig zu überprüfen, ob die Ausdehnung isotrop ist, da nach der Expansion nur eine Kopie abgebildet wird. Dies ist notwendig, um korrekte Schlussfolgerungen aus den Ergebnissen ziehen zu können. Mein Ziel war es daher, ein ‚Lineal' zu entwickeln, das die Isotropie der Ausdehnung misst. Hierfür wurden Partikel des Tabakmosaikvirus (TMV) fluoreszenzmarkiert und als interner Standard in Zellen eingebracht, indem sie an Mikrotubuli gekoppelt wurden. Die Verteilung der Partikellängen und der Signalverlust nach der Expansion erwiesen sich jedoch als problematisch. In Zukunft kann eine einheitliche Viruslänge durch Größenausschlusschromatographie erreicht werden. Weiterhin kann die Signalretention durch Fluoreszenzmarkierung zusätzlicher Aminosäuren der TMV-Hüllproteine und durch Ausstattung der Partikel mit polymerisierbaren Gruppen verbessert werden.

Table of contents

Table of contents

Abbreviations

ABBREVIATION	FULL FORM
4-Hydroxy-TEMPO, 4-HT	4-hydroxy-2,2,6,6-tetramethylpiperidin-1-oxyl
AA	Acrylamide
AcX	Acryoyl-X, 6-((acryloyl)amino)hexanoic acid succinimidyl ester
AF	Alexa fluor
AMPS	2-acryla-mido-2-methyl-1-propanesulfonic acid
APS	Ammonium persulfate
B	Biotin
BG	Benzylguanine
BG-NH_2	O6-(4-Aminomethyl-benzyl)guanine
BG-TMR-MA	Benzylguanine-tetramethylrhodamine-methacrylate
BIS	N,N'-methylene-bis-acrylamide
Boc	Tert-butyloxycarbonyl protecting group
BSA	Bovine serum albumin
CCPs	Clathrin-coated pits
CHC	Clathrin heavy chain
ChromExM	Chromatin expansion microscopy
CLC	Clathrin light chain
CP	Coat protein
Cy	Cyanine
DAPI	4’,6-diamidino-2-phenylindole
DiExM	Differential expansion microscopy
DIG	Digitonin
DMAA	N,N-dimethylacrylamide
DMEM	Dulbecco's modified eagle's medium
DNA-PAINT	DNA-based points accumulation for imaging in nanoscale topography
DSC	N,N’-disuccinimidyl carbonate
(*d*)STORM	(direct) stochastic optical reconstruction microscopy
DTT	Dithiothreitol
DyMIN	Dynamic intensity minimum
EBIS	N,N-ethylene-bis-acrylamide
EDTA	Ethylenediaminetetraacetic acid
EExM	Enhanced expansion microscopy
e.g.	Exemplum gratia, ‘for example’
EM	Electron microscopy

et al.	Et alia, 'and others'
ExFISH	Expansion fluorescent in situ hybridization
ExM	Expansion microscopy
ExPath	Expansion pathology
ExR	Expansion revealing
ExSeq	Expansion sequencing
ExSIM	Expansion structured illumination microscopy
Ex-SMLM	Expansion single molecule localization microscopy
ExSTED	Expansion stimulated emission depletion
ExT	Expansion tomography
FCS	Fetal calf serum
FLARE	Fluorescent labeling of abundant reactive entities
FP	Fluorescent protein
GA	Glutaraldehyde
GFP	Green fluorescent protein
HALO	Haloalkane dehalogenase tag
HATU	Hexafluorophosphate azabenzotriazole tetramethyl uronium
HEPES	4-(2-hydroxyethyl)-1-piperazineethanesulfonic acid
HiExM	High-throughput expansion microscopy
i.e	Id est, ,'that is'
iExM	Iterative expansion microscopy
iU-ExM	Iterative ultrastructure expansion microscopy
JF	Janelia fluor
LExM	Lipid expansion microscopy
LLSM	Lattice light sheet microscopy
LMP	Low melting point
LR-ExM	Label-retention expansion microscopy
LSM	Light sheet microscopy
MA	Methacrylate
MA-NHS	Methacrylic acid N-hydroxysuccinimide ester
MAP	Magnified analysis of the proteome
NA	Numerical aperture
NaCl	Sodium chloride
$NaHCO_3$	Sodium bicarbonate
nb	Nanobody
NH_4Cl	Ammoniumchloride
NHS	N-hydroxysuccinimide
NIFS	Ninefold swelling
NPA	4-nitrophenylalanine
NPC	Nuclear pore complex

NRK49F	Normal rat kidney fibroblast cells
NRK52E	Normal rat kidney epithelial cells
NUP	Nucleoporin
ONE	One-step nanoscale expansion
PA	Photoactivatable
PALM	Photoactivated localization microscopy
PBS	Phosphate buffer saline
p-ExM	Plasmon-enhanced expansion microscopy
PFA	Paraformaldehyde
PhASE-ExM	Phototransfer by allyl sulfide exchange-expansion microscopy
PhotoExM	Photoinitiated polymerization of hydrogels for expansion microscopy
proExM	Protein retention expansion microscopy
ProteomEx	Expansion proteomics
PSF	Point spread function
RMS	Root mean square
ROI	Region of interest
S2	Septin 2
SA	Sodium acrylate
SD	Standard deviation
SEM	Standard error of the mean
SIM	Structured illumination microscopy
SIR	Silicon rhodamine
SMAP	Superhydrophobic microwell array plate
SMLM	Single molecule localization microscopy
SRRF	Super-resolution radial fluctuations
STED	Stimulated emission depletion
TEM	Transmission electron microscopy
TEMED	Tetramethylethylenediamine
TFA	Trifluoroacetic acid
TFP	Tetrafluorophenyl
TIRF	Total internal reflection
TMV	Tobacco mosaic virus
T-RevExM	Thermoresponsive reversible expansion microscopy
TREx	Ten-fold robust expansion microscopy
Tris-HCl	Tris hydrochloride
TRITON	TRIvalenT anchOriNg
U-ExM	Ultrastructure expansion microscopy
uniExM	Uniform expansion microscopy
WGA	Wheat germ agglutinin

WT	Wild type
X10ht	10-fold expansion, high-temperature homogenization
YFP	Yellow fluorescent protein
ZOOM	Zoom by hydrOgel cOnversion Microscopy

Figures and Tables

1. Introduction

1.1 Fluorescence microscopy and the diffraction limit of light

Microscopy has been a milestone in the life sciences for understanding the structure and function of biological systems. The study of biological samples and the spatial arrangements of their components through microscopic imaging offers the possibility of gaining insight into biological systems at the nanoscopic scale that would otherwise remain hidden. At the same time, imaging of biological samples is challenging because of their low refractive index, which results in lower contrast and light scattering. Therefore, fluorescence microscopy has become an indispensable tool in the life sciences, because it makes it possible to label certain proteins or structures and increase the contrast. When light is absorbed by a fluorescent molecule, electrons are excited from the ground state (S0) to a higher energy state (S1). In the excited state, vibrational relaxation to the lowest vibrational state occurs, leading to emission of energy with lower energy and longer wavelength compared to the excitation wavelength (Figure 1a). Thus, it is red-shifted and this process is called fluorescence. The first fluorescence microscope was invented in 1911 by Oskar Heimstaedt and Heinrich Lehmann (Heimstaedt, 1911). In the simplest form of a fluorescent microscope, excitation and emission occur on the same side of the specimen, a technique known as epi-illumination (Figure 1b). However, the broad illumination causes a lot of out-of-focus light to be collected and detected, thus leading to a high signal-to-noise ratio and a lowered resolution. This problem was eliminated by placing a pinhole between the excitation and emission paths so that only light from one focal plane is collected. Therefore, this technology is called confocal microscopy (Minsky, 1957). The sample can be imaged in scanning mode by using a single pinhole (laser scanning confocal microscopy) (Davidovits and Egger, 1969) or through a rotating disc with multiple pinholes (spinning disc confocal microscopy) (Nipkow, 1884; David Egger and Petran, 1967). Another method for reducing the signal-to-noise ratio is through the use of total internal reflection (TIRF) microscopy. This technique takes advantage of the differing refractive indices of the cover glass and the sample, causing light of a certain angle to be completely reflected. This reflection generates an evanescent field that illuminates only a small area of a few hundred

nanometers in the *z* direction, as the field decays with distance from the interface. (Ambrose, 1956; Axelrod, 1981).

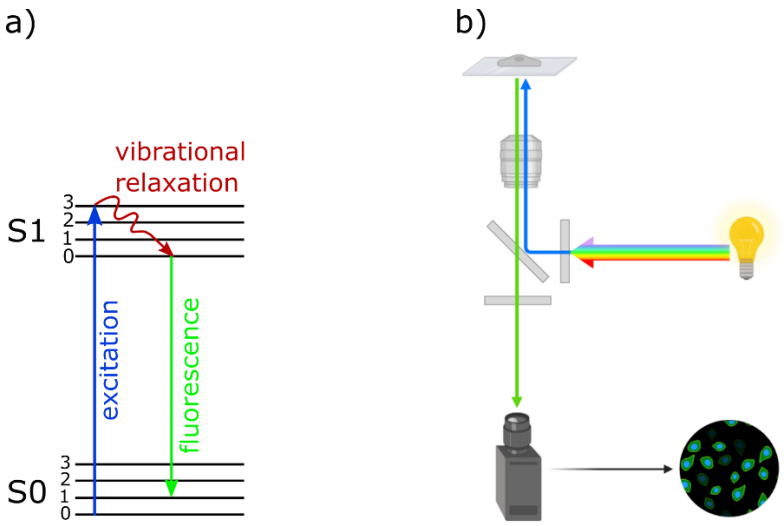

Figure 1: Basics of fluorescence microscopy.

a) Jablonski diagram (Jabłonski, 1933) showing the energy transitions leading to fluorescence. When a fluorophore absorbs light, its electrons get excited and reach a higher energy state (S1). Subsequently, they undergo vibrational relaxation and emit light from a lower vibrational state. The result of this process is an increase in the wavelength of the emitted light, the fluorescence. b) The basic principle of a fluorescence microscope. Light is emitted from a light source and passes through an emission filter that transmits only a specific wavelength required for excitation. The dichroic mirror is a wavelength-specific filter that reflects excitation light but transmits fluorescence light. The excitation light then passes through the objective and reaches the sample. The fluorophores are excited and the fluorescence is detected, resulting in an image.

However, although these techniques enhance the contrast, they are limited in resolution by the diffraction limit of light, which was defined by Ernst Abbe in the late 19th century. The resolution limit of a diffraction-limited microscope is thus determined by the Abbe equation (1.1),

$$d = \frac{\lambda}{2NA} \quad (1.1)$$

where *d* represents the distance that is still resolvable, λ is the wavelength and *NA* is the numerical aperture, which is the primary indicator of an objective's light-gathering ability. When light passes an object, this leads to bending of the light waves, i.e. diffraction. When light travels through the aperture of an objective lens, this causes diffraction and interference of the light waves, resulting in the point spread function (PSF). Shorter

wavelengths and higher *NA* values lead to less diffraction, smaller PSFs and improved resolution.

If two fluorophores are too close to each other, i.e. below the diffraction limit, it is no longer possible to resolve them as individual spots because their PSFs overlap (Figure 2).

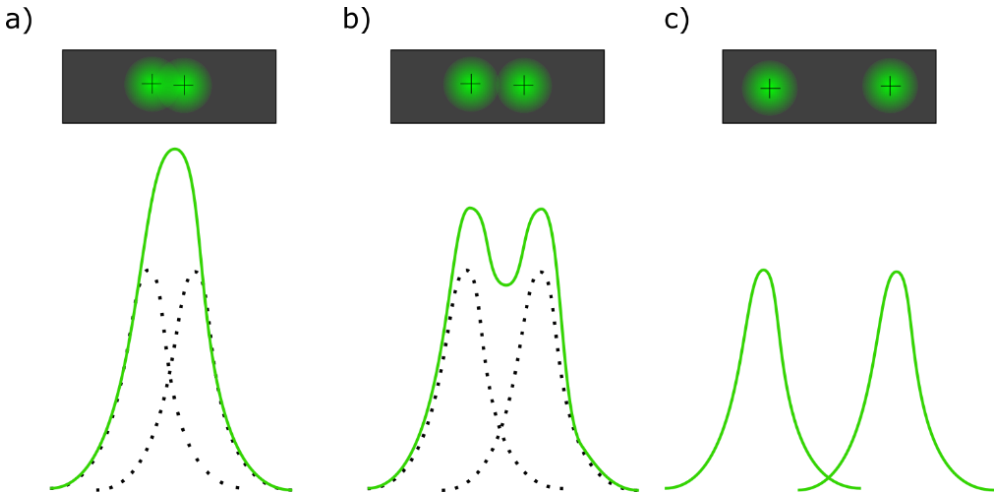

Figure 2: The diffraction limit of light.

a) If two fluorophores are too close to each other, i.e. below the diffraction limit of light, their PSFs overlap and they cannot be resolved individually from each other. b) If the distance between the fluorophores is close to the diffraction limit, their PSFs are just distinguishable, allowing them to still be differentiated from one another. c) When two fluorophores are sufficiently distanced that their PSFs are clearly separated from each other, they are detected as two distinct signals.

1.2 Super-resolution microscopy techniques

In order to overcome the diffraction limit, several techniques were developed, so called super-resolution microscopy techniques. Before their invention, biological structures below the diffraction limit, were accessible only by electron microscopy (EM) (Ruska, 1940). Basically, two different approaches can be distinguished here. Either the PSFs are separated from each other in time or in space. The first approach refers to single molecule localization microscopy (SMLM) (Figure 3a), such as photoactivated localization microscopy (PALM), (direct) stochastic optical reconstruction microscopy ((*d*)STORM) and DNA points accumulation for imaging in nanoscale topography (DNA-PAINT) (Betzig *et al.*, 2006; Rust,

Bates and Zhuang, 2006; Heilemann *et al.*, 2008; Jungmann *et al.*, 2010). The latter approach includes stimulated emission depletion (STED) microscopy (Figure 3b) and structured illumination microscopy (SIM) (Hell and Wichmann, 1994; Klar and Hell, 1999; Gustafsson, 2000).

1.2.1 Single molecule localization microscopy (SMLM)

As the name SMLM suggests, super-resolution is achieved by localizing individual molecules. Techniques in this family include PALM and (*d*)STORM. The difference between these techniques is that PALM uses photoactivatable (PA) proteins, such as PA-green fluorescent protein (PA-GFP) or Eos-fluorescent protein (Eos-FP), and *d*STORM uses photoswitching dyes, such as Cyanine 5 (Cy5) and Alexa Fluor 647 (AF647) (Patterson and Lippincott-Schwartz, 2002; Wiedenmann *et al.*, 2004; Heilemann *et al.*, 2008). An image, which is below the diffraction limit, can be reconstructed by compiling a series of images collected over time. The center of a PSF of a single molecule can be determined if neighboring molecules are temporally kept in the dark state ((*d*)STORM) or are photobleached (PALM), thereby avoiding light emission from all fluorophores simultaneously. In this way high spatial resolution of about 20-50 nm can be obtained. This temporal separation can be achieved by different means. In the original STORM variant an activator fluorophore was required to switch fluorophores ON and OFF (Rust, Bates and Zhuang, 2006), whereas in *d*STORM photoswitching between the bright and the dark state was achieved by exploiting the blinking behavior of certain dyes, like Cy5 and AF647, and the use of special buffer conditions (Heilemann *et al.*, 2008).

However, in PALM a loop of photoactivation, detection, and photobleaching is repeated until no unactivated, unbleached molecules remain (Betzig *et al.*, 2006).

DNA-PAINT is characterized by the binding and unbinding of fluorophore-conjugated single-stranded DNA oligomers to their targets. This ON and OFF binding therefore resembles the alternating ON/OFF switching of fluorescence. An advantage over the aforementioned methods is that no photobleaching occurs because the imager strands bind reversibly to their complementary structures and are refilled continuously (Jungmann *et al.*, 2010). However, a major disadvantage is the long acquisition times.

1.2.2 Stimulated emission depletion (STED) microscopy

In contrast to SMLM techniques, STED microscopy does not rely on computational reconstruction of an image but instead directly generates it. STED utilizes the principle of stimulated emission to suppress the spontaneous fluorescence of molecules located at the focal point's edge (Hell and Wichmann, 1994; Klar *et al.*, 2000). During spontaneous emission, the molecule is excited to a higher energy state and then returns to the ground state spontaneously by emitting a photon with a longer wavelength. However, when the excited molecule is stimulated again by a photon with a wavelength that matches part of its emission spectrum, it emits two identical photons and returns to the ground state. This is the process of stimulated emission (Einstein, 1916). To detect spontaneous emission in a small region, a depletion laser with a donut-shaped intensity profile is required. The center of the profile should have zero intensity, which is created by destructive interference patterns (Reuss *et al.*, 2010). The donut-shaped intensity profile of the depletion laser allows only the fluorophores in the central region to emit photons through spontaneous fluorescence emission. This reduces the PSF and results in higher resolution (Hell and Wichmann, 1994; Klar and Hell, 1999). It follows that an increase in laser intensity leads to a broadening of the diameter of the depletion beam and thus to a reduction of the area in which photons are emitted. Ultimately, this leads to improved resolution but also to increased bleaching and consequently lower signal intensity (Westphal and Hell, 2005). To solve this problem adaptive illumination STED nanoscopy, especially dynamic intensity minimum (DyMIN) scanning, was developed. Here, depletion laser intensities are dynamically modified during imaging according to the local structural features, resulting in reduced photobleaching and enhanced contrast and resolution (Göttfert *et al.*, 2017; Heine *et al.*, 2017). A big advantage of 2D STED compared to 2D SMLM techniques is the fast acquisition time due to the use of the laser scanning confocal mode for illumination of the sample. For 3D STED, a second axial STED laser is used in addition to the spatial donut laser (Wildanger *et al.*, 2009). However, STED microscopy is best suited for imaging near the coverslip surface (0-15 µm) due to its high optical requirements. The problematic aberrations, which occur when imaging deep inside specimens can be corrected by the use of adaptive optics, namely spatial light modulators, which are placed in the phase of the depletion beam (Gould *et al.*, 2012; Patton *et al.*, 2016; Zdankowski *et al.*, 2019).

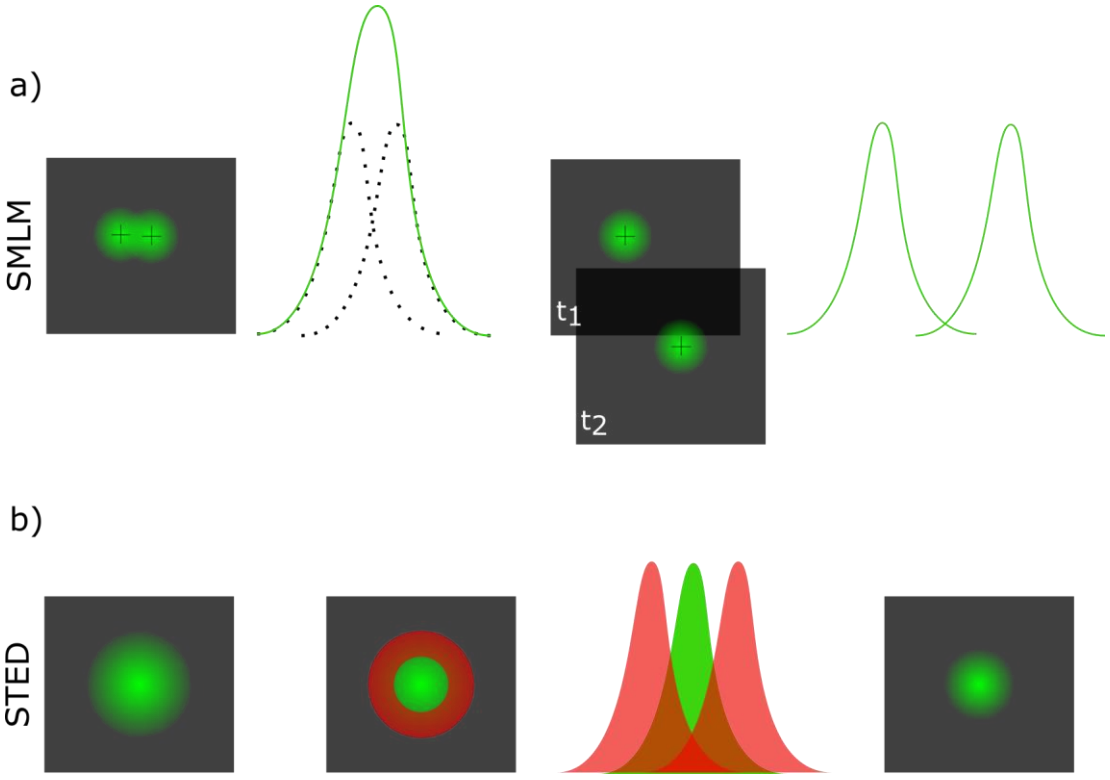

Figure 3: Basic principles of super-resolution microscopy techniques.

a) In SMLM two fluorophores, which are too close to each other to be resolved by diffraction-limited microscopy are separated in time and individually localized one after the other. Thereby, their PSFs can be recorded individually, resulting in a super-resolved image. b) STED microscopy utilizes a depletion laser (shown in red) to reduce the size of the PSF and increase the resolution.

1.3 Expansion microscopy

All the above mentioned super-resolution techniques have in common that they require expensive equipment and a high level of specialist knowledge about them, which makes them accessible to a limited number of people only. To counter this, expansion microscopy (ExM) was invented in 2015 by Edward Boyden´s group (Chen, Tillberg and Boyden, 2015). The main advantages of this method are that it does not require sophisticated technology and is relatively easy to implement. The field of ExM has developed rapidly in recent years, so that many protocols are available for different purposes and a wide range of applications. In its simplest form, ExM consists of a fluorescently labeled sample, which is embedded in a polyacrylamide gel formed by radical polymerization between acrylamide (AA), N,N'-methylene-bis-acrylamide (BIS) and sodium acrylate (SA) after an anchoring step (Chen, Tillberg and Boyden, 2015). An anchoring reagent, such as 6-

((acryloyl)amino)hexanoic acid succinimidyl ester (Acryloyl-X, AcX) equips labels and proteins with a polymerizable unit, so that they copolymerize into the formed hydrogel (Tillberg *et al.*, 2016). The sample is then digested by a protease, e.g. proteinase K, to ensure for a homogenous and isotropic expansion in water (Chen, Tillberg and Boyden, 2015). As long as salt is present in the buffer, the charges of the ionic groups are shielded. However, as soon as the gel is immersed in water, the salt is flushed out and the charge is repelled, resulting in expansion (Buchholz, 1994). By expanding the hydrogel, the structure is pulled apart increasing the physical distance between the labels (Figure 4a). Consequently, fluorophores, which had overlapping PSFs before expansion can now be distinguished (Figure 4b). As the biological structure itself is digested, the resulting image represents the larger facsimile of the original biological structure.

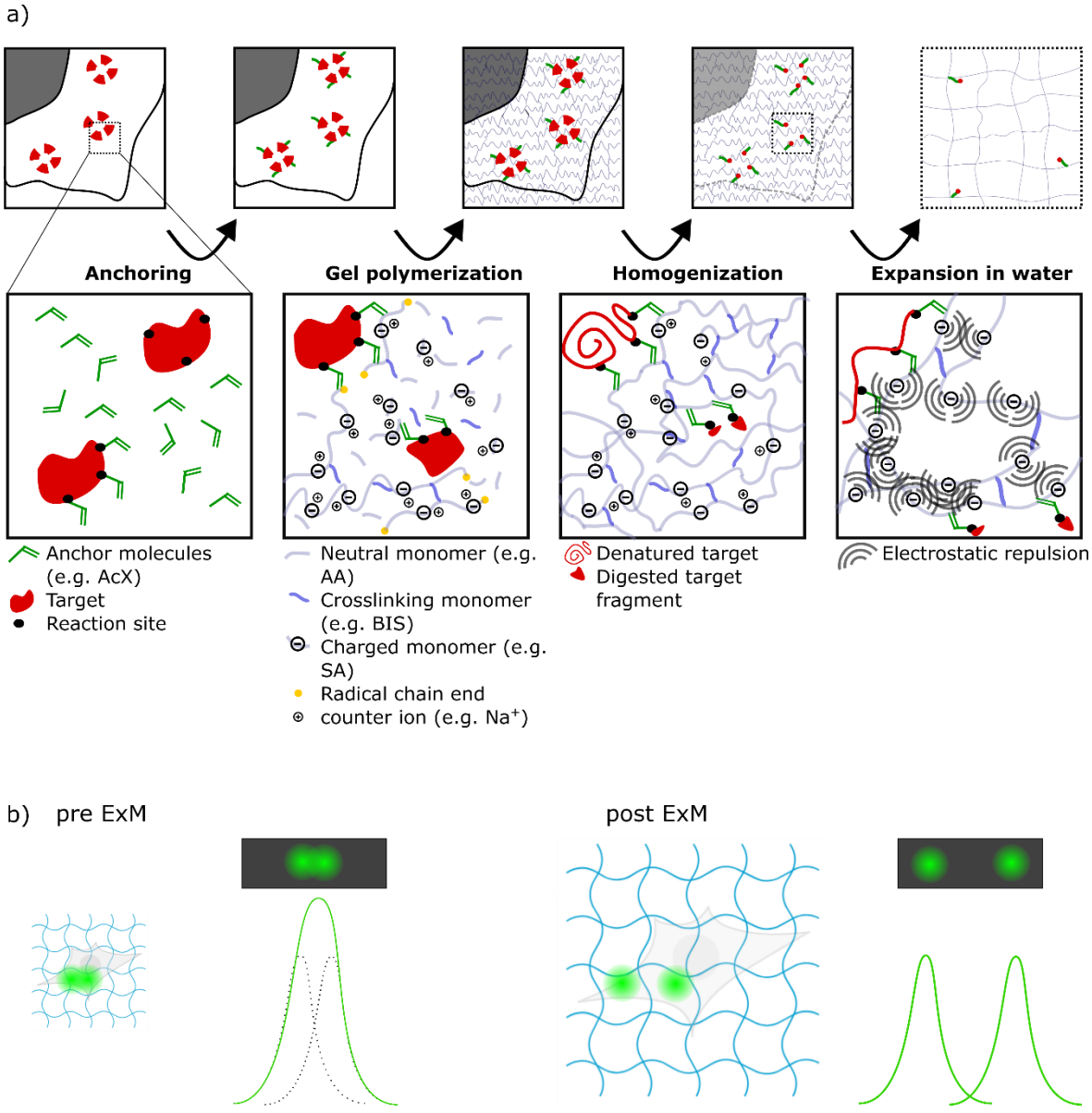

Figure 4: ExM principle.

a) Principle of the ExM technique. After anchoring the target, e.g. with AcX, the polyacrylamide gel is formed. Gelation occurs between neutral monomer groups, such as acrylamide, and crosslinking monomers, such as BIS. The charged monomer SA provides ionic groups to the gel. In most cases, polymerization occurs by radical-induced chain growth until the polymer network is formed and the anchored portions of the target structure are copolymerized into the gel. In the next step, the structure is digested or denatured and only the anchored fragments remain in the gel. Non-anchored fragments are washed away. In the final step, the polyacrylamide gel is immersed in water and expands due to charge repulsion as the salt-containing buffer is washed away and the charges are no longer shielded. Adapted with permission from N. Hümpfer, R. Thielhorn, H. Ewers, unpublished work, under review at Journal of Cell Science. b) Two objects that cannot be resolved by diffraction limited microscopy due to their overlapping PSFs can be resolved after expansion due to the increased physical distance between the objects.

1.3.1 ExM variants

In the original ExM protocol the protein of interest was anchored into the gel by a methacryloyl group, which was coupled to an oligo-bearing secondary antibody (Chen, Tillberg and Boyden, 2015). This anchoring strategy was simplified by using a global anchoring reagent such as AcX, methacrylic acid N-hydroxysuccinimide ester (MA-NHS) or glutaraldehyde (GA) (Chozinski *et al.*, 2016; Tillberg *et al.*, 2016). In the following years, several variants of ExM were developed, most of them with the aim of increasing the resolution. This development can generally be divided into two strategies. First, combining ExM with super-resolution techniques, such as SIM (Halpern *et al.*, 2017), STED (Unnersjö-Jess *et al.*, 2016a; Gao *et al.*, 2018), light sheet microscopy (LSM) (Bürgers *et al.*, 2019) , lattice light sheet microscopy (LLSM) (Gao *et al.*, 2019), and SMLM (Zwettler *et al.*, 2020). Second, varying the hydrogel composition to allow higher expansion factors, as in X10 (Truckenbrodt *et al.*, 2018) or ten-fold robust expansion microscopy (TREx) (Damstra *et al.*, 2022), which allow expansion factors of 10. In enhanced ExM (EExM) X10 microscopy was combined with Airyscan to further increase the resolution (Sheard *et al.*, 2019). In an approach called X10 heat-treated (X10ht), X10 microscopy has been combined with high-temperature homogenization. The signal intensity increased compared to proteinase K treated samples and enabled the analysis of 200 µm thick tissue samples (Saal *et al.*, 2023). Higher expansion factors were also achieved by performing two rounds of expansion, as shown in iterative ExM (iExM) (Chang *et al.*, 2017). This approach was later combined with ultrastructure ExM (U-ExM) (Gambarotto *et al.*, 2019) in an approach called iterative ultrastructure ExM (iU-ExM) (Louvel *et al.*, 2023). In addition to improving resolution, other approaches were aimed at improving the labeling or were optimized for specific target structures. For example, very shortly after the introduction of ExM, expansion fluorescent in situ hybridization (ExFISH) was already developed to visualize RNA with ExM (Chen *et al.*, 2016). Expansion pathology (ExPath) was developed to image clinical samples (Zhao *et al.*, 2017). The expansion of membranes appeared to be difficult because of the lipids lacking an amine-anchorable group. However, ExM variants addressing this issue were introduced with sphingolipid ExM and lipid ExM (LExM) (Götz, Kunz, *et al.*, 2020; White *et al.*, 2022). Labeling of various biomolecules such as lipids, glycans, RNA and proteins was enabled by Click-ExM (Sun *et al.*, 2021). In addition, a multifunctional anchor was developed in uniform

ExM (uniExM) that can anchor different types of biomolecules in a single experimental step (Cui *et al.*, 2022). In contrast, Magnify does not require an additional anchoring step and is suitable for nucleic acids, proteins and lipids (Klimas *et al.*, 2023). M'Saad and Bewersdorf developed a whole cell staining with N-hydroxysuccinimide (NHS) ester dyes that resembles EM-like images when combined with an iterative expansion, called pan-ExM (M'Saad and Bewersdorf, 2020). In addition to its low cost and simple feasibility, another benefit of ExM is its potential for decrowding. Expansion Revealing (ExR) has been shown to increase the accessibility of proteins to antibody staining by expanding the sample prior to labeling, especially in crowded environments such as the brain (Sarkar *et al.*, 2022). For an overview of the evolution of ExM variants over time, see Figure 5a.

At the beginning of ExM development, the resolution was about 70 nm with the 4x ExM protocols (Chen, Tillberg and Boyden, 2015; Chozinski *et al.*, 2016; Tillberg *et al.*, 2016) and it decreased to 20-25 nm with expansion factors of ~20 achieved by X10 and iExM. Only the combination with super-resolution techniques could further reduce the resolution to 10 nm (Unnersjö-Jess *et al.*, 2016b; Gao *et al.*, 2018; Zwettler *et al.*, 2020) until a resolution of about 1 nm was achieved by a very recent ExM variant called one-step nanoscale expansion (ONE) microscopy. Here, 10-fold expansion was combined with a fluorescence-fluctuation analysis, called super-resolution radial fluctuations (SRRF) method (Shaib *et al.*, 2022). An exemplary overview of how the improvement in resolution has developed with the introduction of further ExM variants can be found in Figure 5b. It should be noted that the resolution between organelles may be different because organelles do not expand to the same extent. This is due to the different biochemical properties that affect the swelling behavior between organelles (Zhao *et al.*, 2017; Pernal *et al.*, 2020; Büttner *et al.*, 2021). In differential ExM (DiExM) it was shown that tissues, organelles, and even domains within organelles expand differently (Pernal *et al.*, 2020).

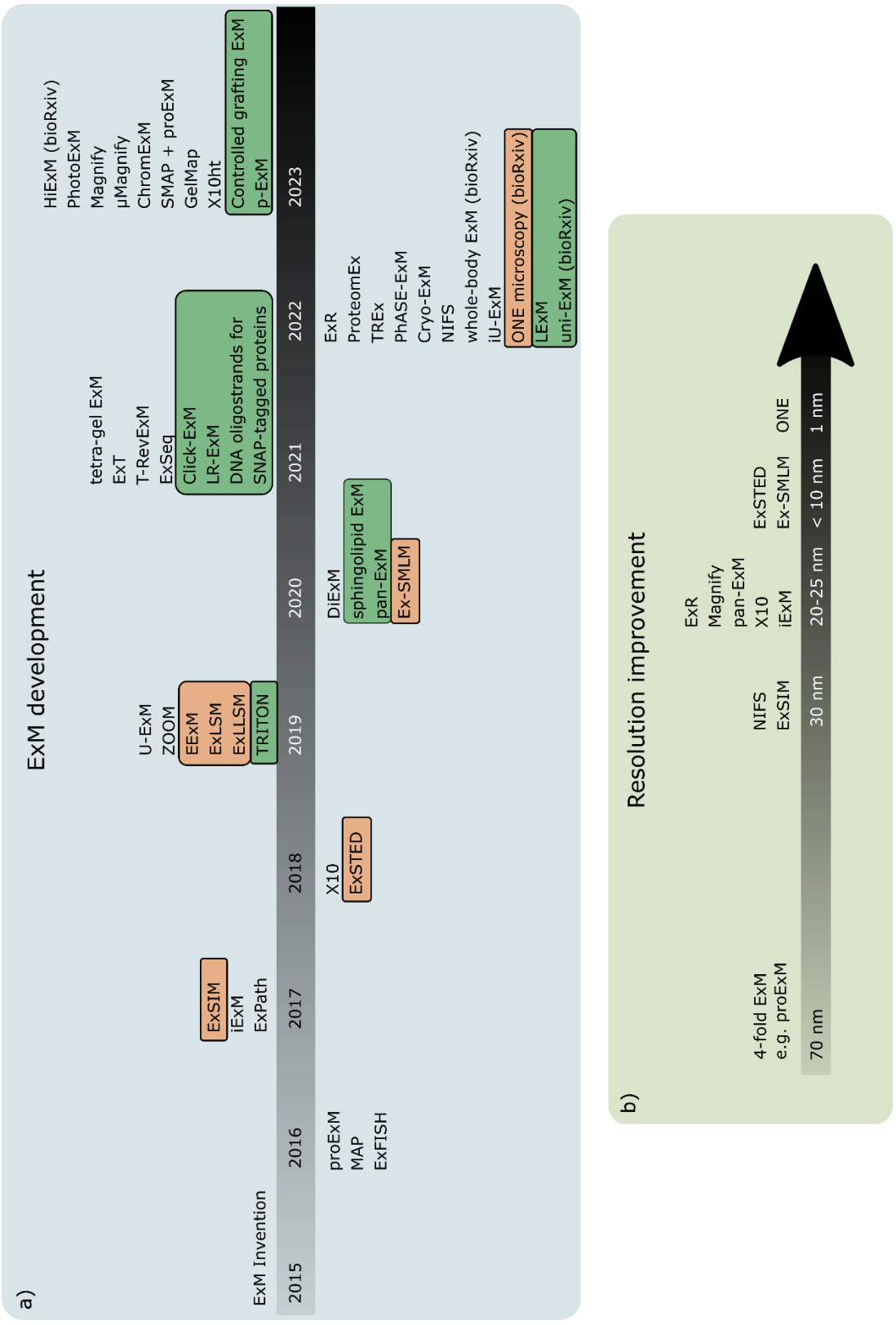

Figure 5: ExM development.

a) Timeline showing the ExM development from its invention in 2015 until 2023. ExM techniques combined with super-resolution techniques are shown in orange. ExM techniques, which are focused on the labeling of the target structures are highlighted in green. b) Schematic and exemplary representation of the resolution improvement with the invention of new ExM variants.

1.3.2 Challenges for ExM

Retention of the fluorescence signal is one of the major problems in ExM. On the one hand the local fluorophore density with a 4-fold expansion protocol is diluted by a factor of 64 because of the volumetric expansion in all three dimensions. This problem is intrinsically to the expansion process and cannot be circumvented. It plays an even greater role at higher expansion factors, leading to a ~1000-fold reduction for X10 microscopy. On the other hand proteases used for the digestion step are necessary to provide an isotropic expansion but at the same time also cut off labels, which will be washed away. All these factors contribute to a significant signal loss after expansion. How this challenge can be addressed and what labeling techniques exist to date is described in 1.3.3.

Additionally, some dyes, e.g. cyanine dyes or AF647, do not withstand the polymerization process. This issue can be addressed easily by the choice of dye. However, even dyes suitable for ExM can get partially damaged due to radical reactions, which further reduces brightness (Chen, Tillberg and Boyden, 2015; Tillberg *et al.*, 2016). A way to increase the photostability of fluorophores was recently demonstrated by Wen *et al*. They showed that conjugation of 4-nitrophenylalanine (NPA) in proximity to the dye protects it from radical induced degradation (Wen *et al.*, 2022).

The intact preservation of the structure can be hindered by non-optimal anchoring, gelling and homogenization conditions. If these steps are not optimized for the desired expansion factor and sample, cracking of the target sample can occur. An example is ensuring homogeneous gelation in thick samples, e.g. tissue, where 4-hydroxy-2,2,6,6-tetramethylpiperidin-1-oxyl (4-Hydroxy-TEMPO, 4-HT) can be added. It inhibits gel formation and allows the monomer solution to penetrate deep into the sample before polymerization begins. A similar effect is achieved by incubating the sample with the monomer solution prior to adding the polymerization initiator. In addition, even before the gel is formed, artifacts may occur due to fixation (Schnell *et al.*, 2012). In U-ExM a single fixation step was avoided and later cryofixation ExM (Cryo-ExM) was developed to preserve the native ultrastructure and remove artifacts caused by aldehyde fixation techniques or protein denaturation (Gambarotto *et al.*, 2019; Laporte *et al.*, 2022).

From the beginning of the ExM development the isotropic expansion of the specimen has been an often discussed aspect. Since only a replica of the original biological structure is imaged after expansion, it is essential to assess whether the length ratios between the expanded labeled structures still correspond to those of the original sample. It is known that polyacrylamide gels formed by radical-induced polymerization often exhibit network heterogeneities due to stochastically distributed crosslinking points and topological defects such as dangling ends and loops. Therefore, the mesh size is not uniform, but varies between 1-10 nm (Di Lorenzo and Seiffert, 2015). These differences in the polymer network result in differences in the swelling behavior of the gel. Areas containing a high number of crosslinking points swell less compared to areas with a low number of crosslinking points (Bastide and Leibler, 1988) (Figure 6). Consequently, it can be assumed that these heterogeneities and variations in swelling among different gel regions contribute to the distortion of the biological structure.

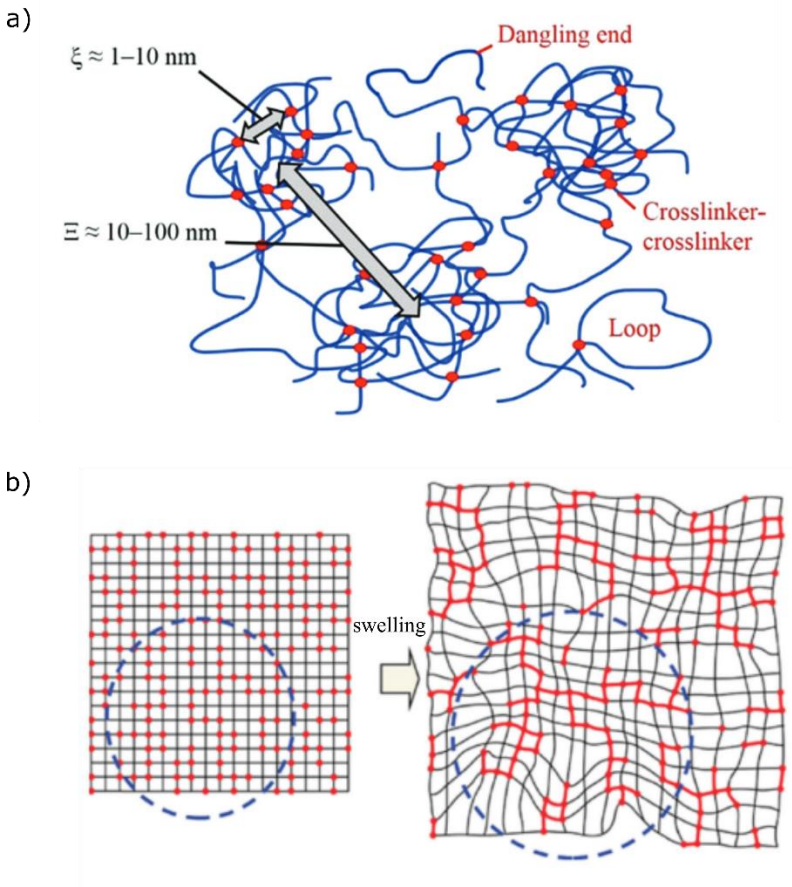

Figure 6: Network heterogeneity and swelling behavior of polyacrylamide gels.

a) Radical-induced polymer networks display heterogeneity due to randomly distributed crosslinking points, dangling ends, and loops. The small arrow marks a typical mesh size of 1-10 nm,

while the long arrow indicates the spatial distances between highly crosslinked regions. b) Polymer networks with randomly distributed crosslinking points experience different degrees of swelling. Regions with high crosslink density show less swelling than areas with sparse crosslinking. Reprinted with permission from (Di Lorenzo and Seiffert, 2015).

To address this issue several methods have been used additionally to comparing the exact same region of interest before and after expansion. For example, subcellular reference structures like nuclear pores can be used. One advantage of this method is that pre ExM imaging is not necessary. The expanded nuclear pore provides information about the expansion factor and the distortion due to the known original size and shape (Pesce *et al.*, 2019; Thevathasan *et al.*, 2019). Vanheusden *et al.* developed an intrinsic ruler by photobleaching an area of a well-defined shape before expansion and comparing it with the expanded size and shape of that very area (Vanheusden *et al.*, 2020). Recent approaches for analyzing the distortion and calculating the expansion factor focused on the application of DNA-origamis (Scheible and Tinnefeld, 2018; Lee *et al.*, 2021) and nanopillars (Nakamoto *et al.*, 2022) as rulers for ExM. Another approach focuses on simplifying specimen handling for correlative pre and post ExM imaging rather than developing a ruler by preserving the gel geometry in a newly developed microplate system (Seehra *et al.*, 2023). In chromatin ExM (ChromExM), the authors introduced a pattern of parallel stripes into the nucleus. They expected the stripes to remain parallel if the expansion was isotropic (Pownall *et al.*, 2023). In a very recent method, called GelMap, a fluorescent grid is introduced into the polyacrylamide gel before expansion. This grid expands to the same extent as the sample. Finally, the distortion can be easily detected from the expanded grid (Damstra *et al.*, 2023). Since local protein density has an effect on the expansion of the sample, and organelles have been shown to expand differently (Büttner *et al.*, 2021), GelMap presents a promising tool because it reports local deformations in the areas of interest. This must be considered when structures other than the structure of interest are used to measure the distortion or the expansion factor and especially when they originate from different cells, even within the same sample.

If only the calculation of the expansion factor is of interest, the simplest method is to measure the macroscopic size of the gel before and after expansion and then divide the resulting diameters. However, it has been shown that this calculation is inaccurate and only

gives an indication of the actual expansion achieved within the cell. Proteins in the cell actually seem to expand more than the total gel block (Martínez *et al.*, 2020). Therefore, one of the above methods should be considered for an accurate calculation.

1.3.3 Labeling techniques

Samples subjected to ExM can be labeled either before expanding, more specifically after fixing and before gelling, or after expanding. Advantages of pre ExM labeling are that the sample can be imaged before and after expansion and the same regions of interest can be compared. This gives detailed and precise information about the distortion in the region of interest and the resolution improvement. Disadvantages of this labeling concept are the introduced linkage error and the loss of labels during digestion. Immunolabeling introduces a labeling error of the size of the antibodies, which scales with the expansion. Post ExM labeling however, introduces antibodies at a later step, after the first expansion step, which is followed by the final expansion step after labeling (Gambarotto *et al.*, 2019). Therefore, one of the major disadvantages of pre ExM labeling, which is the fluorophore loss in the digestion step, is avoided in post ExM labeling. However, when using post ExM labeling, it has to be considered that not all epitopes survive denaturation. It can be problematic to label genetically encoded tags such as SNAP- or HALO-tag, since they are no longer accessible after denaturation (Razzaq *et al.*, 2021). Some probes do not bind after denaturation or proteolytic treatment due to structural changes of the target and are therefore not suited for post-expansion labeling, e.g. phalloidin (Park *et al.*, 2020).

Among the different classes of target structures, not only proteins but also RNA, lipids and carbohydrates can be labeled. Cells can be labeled metabolically to equip lipids or glycans with an alkyne group, which can subsequently be labeled via click chemistry (Sun *et al.*, 2021). Glycans in particular, can be labeled using the fluorescent labeling of abundant reactive entities (FLARE) method which involves oxidizing the diols of monosaccharides to aldehydes and then labeling them with hydrazide fluorophores (Lee *et al.*, 2022). One strategy for labeling RNA is to alkylate its bases with LabelX or to use an acrylate-modified probe that hybridizes to the poly(A) tail of mRNAs to anchor them to the polyacrylamide gel (Chen *et al.*, 2016; Wang, Moffitt and Zhuang, 2018).

In the following, I will focus on pre ExM labeling approaches for proteins as these are subject of this study. As explained above (see 1.3.2) one major issue in ExM is the fluorophore loss and the improvement of signal retention to obtain a good post ExM image quality. Therefore, several ideas have been put forward to address this issue.

In protein retention ExM (proExM), the target protein is stained by conventional immunostaining, and the signal is retained by using an anchoring reagent such as AcX (Tillberg *et al.*, 2016) (Figure 7a). Amines, regardless of whether they are part of the target protein or the antibody, are randomly crosslinked into the polyacrylamide network. It has to be noted that only (fluorescent) proteins, like the green fluorescent protein (GFP), are anchored but not dyes themselves. After proteolytic digestion various fragments remain. On the one hand, some fragments are anchored but not labeled and therefore invisible after expansion. On the other hand, there are fragments that are labeled but have no anchoring moiety and are therefore also invisible because they are washed away. Only those fragments that are labeled and crosslinked to the gel via AcX can be imaged. For this reason, many approaches to increase signal retention in ExM aim to link the polymerizable moiety and the fluorophore in one molecule so that they cannot be separated by proteolytic digestion. This led to the development of trifunctional linkers, which combine the anchoring, targeting and reporter moiety in one molecule. In 2020 Wen *et al.* published the first approach to enable direct grafting of the label, called TRITON, standing for TRIvalenT anchOriNg (Wen *et al.*, 2020). The multivalent linker consists of a fluorescent reporter, a reactive handle for conjugation, e.g. tetrafluorophenyl (TFP) ester for amine conjugation, and a monomer for grafting. Secondary antibodies can be attached to the TRITON linker via TFP ester chemistry (Figure 7b). Similar to TRITON, trifunctional anchors were developed, which bind to SNAP- or CLIP-tagged proteins and provide them with a polymerizable unit. However, the reporter molecule is not directly included in the trivalent linker. Instead, biotin (B) or digitonin (DIG) is used, which is recognized after digestion by fluorescently labeled streptavidin or fluorescently labeled anti-digitonin, respectively (Shi *et al.*, 2019) (Figure 7c). The combination of all three functions, target recognition, grafting and reporting has also been realized by the use of DNA oligo strands. Here, benzylguanine (BG) and acrydite are linked to one end of the oligo, whereas the fluorophore is located on the opposite end (Yao *et al.*, 2021) (Figure 7d). A disadvantage of this method is that the

DNA oligo strands are not cell permeable and therefore not suitable for live cell labeling. This means that the cells must either be fixed before staining or permeabilized alive with digitonin, as the authors suggest (Yao *et al.*, 2021).

Another approach, which requires a biotinylated target protein uses fluorescently labeled streptavidin that has been additionally labeled with AcX (Kim, Kim, Lee and S. Shim, 2019; M. Kang *et al.*, 2021) (Figure 7e). Due to the four biotin binding sites of the tetrameric streptavidin molecule, signal amplification is possible by adding more biotin and fluorescently labeled streptavidin. This has been shown to be beneficial in expansion STED (ExSTED) imaging (Kim, Kim, Lee and S. H. Shim, 2019).

The trifunctional dye, which is a main component of this doctoral thesis, combines target linkage via the BG-SNAP tag interaction, the fluorophore, here tetramethylrhodamine (TMR), and the monomer for gel anchoring in one molecule (Figure 7f-g) (Thielhorn *et al.*, 2023). It is a very small molecule, less than 1 kDa, that binds covalently to its protein of interest and is able to penetrate the cell membrane.

Further concepts for labeling involve using plasmonic fluors to enhance the fluorescence signal called plasmon-enhanced ExM (p-ExM) or aim at multi-color imaging (Min *et al.*, 2020; Rathi *et al.*, 2023).

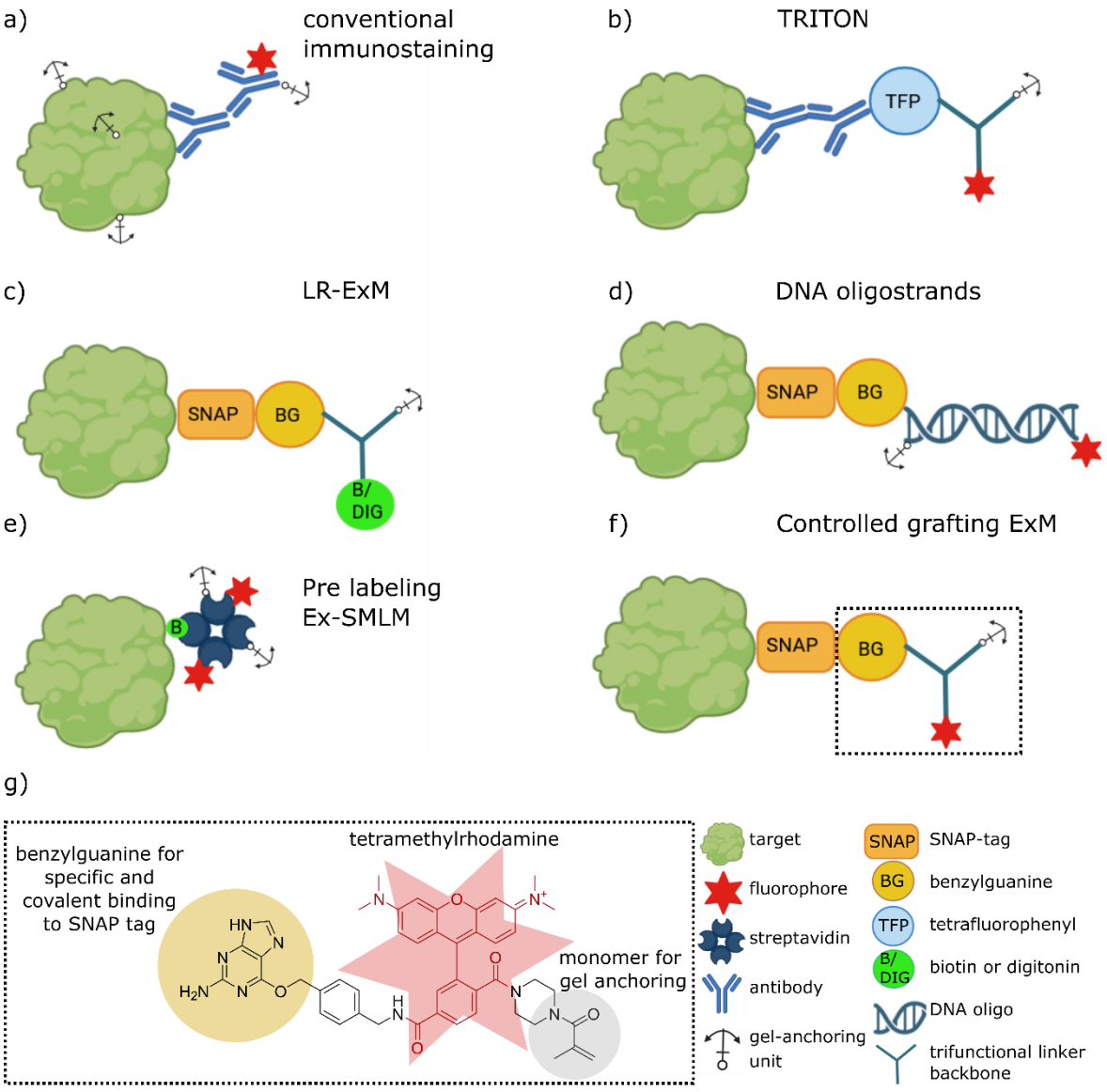

Figure 7: Concepts for pre ExM labeling.

a) Conventional immunostaining is used to stain the protein of interest in combination with an anchoring reagent like AcX, which crosslinks amines into the polyacrylamide network. AcX reacts randomly with free amines of the target and the antibodies. b) Direct grafting approach with trifunctional TRITON linker. c) Label-retention ExM (LR-ExM) uses trifunctional anchors for optimal signal retention. The fluorophore, coupled to streptavidin or anti-digitonin, is added after digestion (not shown). d) Labeling system based on a DNA oligostrand coupled to benzylguanine for SNAP-tag binding, acrydite and a fluorophore. e) Pre labeling Ex-SMLM uses streptavidin coupled to fluorophores and anchoring units to label a biotinylated target protein. f) Trifunctional rhodamine probe bound to SNAP-tagged protein, which is the subject of this thesis. g) Detailed chemical structure of trifunctional rhodamine probe (boxed region in (f)).

1.3.4 Polymer chemistry and grafting

The polyacrylamide gel composition in the classic 4-fold expansion protocol consists of AA, BIS and SA. Together, they make up the monomer solution (MS). AA provides the backbone, BIS is the crosslinker that connects the polyacrylamide chains to form a network (Figure 8a) and SA provides the gel with ionic groups. The latter ultimately contributes to the swelling of the gel (Buchholz, 1994). Removing salt through water immersion results in the negative charge repelling and causing expansion. This, in turn, leads to the formation of hydrogen bonds (Nasu, Ozaki and Sato, 2021) (Figure 8b). Consequently, more ionized groups in combination with lower concentration of crosslinker lead to higher expansion factors. Unfortunately, this is at the expense of gel stability, resulting in a trade-off between gel stability and expansion factor (Zohuriaan-Mehr and Kabiri, 2008). The chain polymerization reaction is initiated by ammoniumpersulfate (APS), a free-radical initiator, and catalyzed by tetramethylethylenediamine (TEMED). Polymerization performs rapidly and oxygen has an inhibitory effect on the polymerization because it reacts with free radicals (Bhanu and Kishore, 1991).

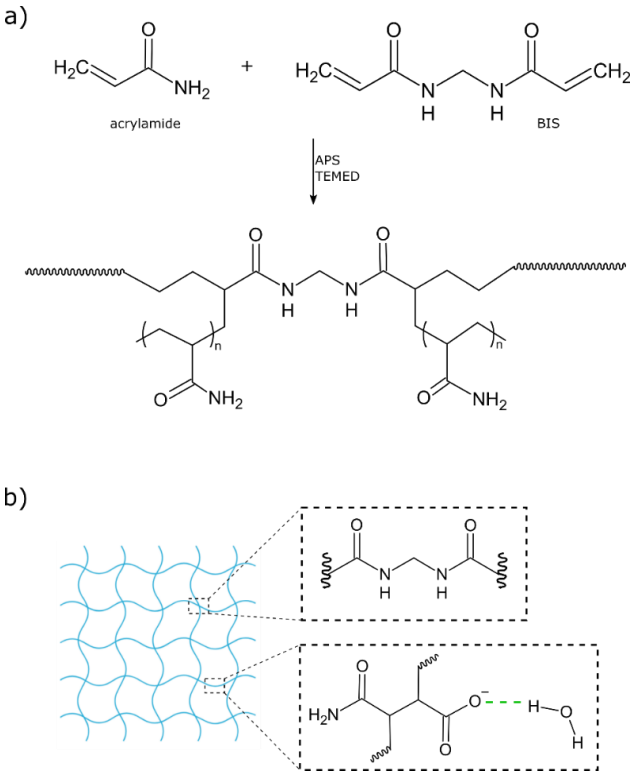

Figure 8: Polyacrylamide gels for ExM.

a) Polymerization reaction. BIS acts as crosslinker to connect the polyacrylamide chains. The polymerization reaction is initiated by APS and catalyzed by TEMED. Figure adapted with permission

from (Huang *et al.*, 2018) © The Optical Society. b) Schematic representation of an expanded polyacrylamide network. The upper box depicts polymerized BIS as part of the network, while the lower box shows sodium acrylate with a negatively-charged carboxylate ion (COO-). The repulsion of negative charges causes the hydrogel to swell, accompanied by the formation of hydrogen bonds (indicated in green). Figure adapted with permission from AAAS (Chen, Tillberg and Boyden, 2015).

As described in 1.3.2 polyacrylamide gels formed by radical-polymerization exhibit a network heterogeneity due to dangling ends, loops and crosslinker-crosslinker linkages (Di Lorenzo and Seiffert, 2015). The network heterogeneity can be influenced by the crosslinker and monomer concentration (Kizilay and Okay, 2003; Nie, Du and Oppermann, 2004) and the reactivity of the chosen crosslinking agent (Lindemann, Schröder and Oppermann, 1997). If the crosslinker concentration is increased, while the monomer concentration is kept constant, this results in higher network heterogeneity (Kizilay and Okay, 2003). The opposite effect can be observed with increasing the monomer concentration at a constant crosslinker concentration, leading to more homogenous network structures (Nie, Du and Oppermann, 2004).

Approaches to develop a more homogenous gel system for ExM focused on non-radical and step-growth polymerized hydrogels (Gao *et al.*, 2021; Günay *et al.*, 2023). Gao *et al.* showed that by using tetrahedral monomers and click-chemistry, a more homogenous ExM matrix was generated, which enabled expansion of virions with smaller spatial errors compared to polyacrylamide hydrogels (Gao *et al.*, 2021). However, the photoinitiated polymerization process of hydrogels (PhotoExM) implements a mixed-mode polymerization initiated by light that is insensitive to oxygen. It combines chainwise and stepwise polymerization and therefore homogenizes the spatial distribution of crosslinking points (Günay *et al.*, 2023). PhotoExM was then combined with hydrogels prepared using allyl-sulfide crosslinking groups in an approach known as phototransfer by allyl sulfide exchange-expansion microscopy (PhASE-ExM) (Blatchley *et al.*, 2022).

ExM variants use different gel compositions to meet their requirements. For example in magnified analysis of the proteome (MAP) and U-ExM high concentrations of AA were used to prevent intra- and interprotein crosslinking thereby enabling complete dissociation and denaturation of proteins (Ku *et al.*, 2016; Gambarotto *et al.*, 2019). In iExM and ExM variants, which made use of iterative gelation and expansion, like pan-ExM, the cleavable

crosslinker N,N´-(1,2-dihydroxyethylene)bisacrylamide (DHEBA) was added, to allow multiple rounds of expansion (Chang *et al.*, 2017; M'Saad and Bewersdorf, 2020). The monomer N,N-dimethylacrylamide (DMAA) was used in X10 microscopy to generate a hydrogel, which can expand 10-fold (Truckenbrodt *et al.*, 2018). The crosslinker N,N-ethylenebisacrylamide (EBIS) was used to create a ninefold swelling (NIFS) hydrogel (H. Li *et al.*, 2022). Furthermore, in expansion tomography (ExT) the monomer 2-acrylamido-2-methyl-1-propanesulfonic acid (AMPS) was added additionally to AA to produce a superabsorbent gel with high mechanical strength that allowed for alternating imaging and sectioning (Chen *et al.*, 2021). To adjust the expansion factor in a temperature-dependent manner hydrogels were prepared with poly(N-alkyl acrylamide) or poly(methacryloyl sulfobetaine) in an approach called thermoresponsive ExM (T-RevExM) (Kang *et al.*, 2021). Similarly, in Zoom by hydrOgel cOnversion Microscopy (ZOOM), the expansion factor was adjusted through alkaline hydrolysis with heat. The nonionic primary amide side chains of the AA hydrogel undergo alkaline hydrolysis, resulting in the formation of ionic carboxylate groups. An increase in the number of ionic groups finally leads to an expansion ratio increase (Park *et al.*, 2019).

For the target structure to be visualized after expansion, it is essential that it, or more precisely the fluorophore with which it was labeled, is incorporated into the polyacrylamide network. For this purpose, the label is provided with a polymerizable group, which can be achieved by various methods (see 1.3.3). The more label is incorporated into the polyacrylamide mesh, the higher the fluorescence intensity after expansion. Therefore, it is important to understand how this incorporation works and what factors are involved so that ultimately signal retention can be maximized. The term chemical grafting describes the chemical attachment of polymers to surfaces. It can be divided into three subgroups: "grafting to", "grafting from" and "grafting through". In "grafting to" preformed polymer chains are chemically anchored to the substrate (Figure 9a). In contrast, "grafting from" describes the growth of a polymer chain started from an initiator-functionalized surface (Figure 9b). However, in the "grafting through" approach copolymerization proceeds via incorporation of surface-bound monomers and free monomers (Figure 9c) (Henze *et al.*, 2014; Datta and Genzer, 2016).

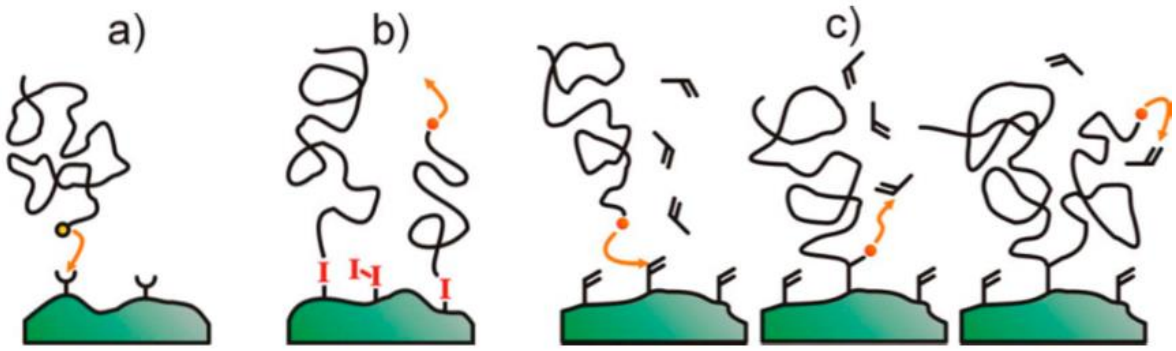

Figure 9: Overview of grafting techniques.

a) "grafting to", b) "grafting from", c) "grafting through" approach. Reprinted with permission from (Henze *et al.*, 2014). Copyright {2023} American Chemical Society.

1.3.5 Applications of ExM

The extremely rapid development of ExM has led to the creation of a huge number of ExM variants (see 1.3.1) and various applications in a very short time. As mentioned in 1.3.1 ExM was successfully combined with many super-resolution techniques and the gel recipe has undergone many changes, resulting in improvement in resolution. Apart from that, ExM has been utilized in a wide range of biological samples and species, such as yeast, fly, worm, mouse, algae, bacteria, fungi, plants, fish, birds, insects, parasites and viruses (Freifeld *et al.*, 2017; Mosca *et al.*, 2017; Halpern *et al.*, 2017; Jiang *et al.*, 2018; Düring *et al.*, 2019; Lim *et al.*, 2019; Gambarotto *et al.*, 2019; Kao and Nodine, 2019, 2021; Yu *et al.*, 2020; Götz, Panzer, *et al.*, 2020; L. Chen *et al.*, 2021; Gao *et al.*, 2021; Steib *et al.*, 2022; Kraft *et al.*, 2023). Furthermore, with whole-body ExM an entire mouse embryo could be imaged with detailed precision as well as a full zebra fish larvae (Sim *et al.*, 2022).

Clinical application was made possible through the use of ExPath, a variant of ExM that facilitates the imaging of clinical specimens, enabling the diagnosis of diseases previously only detectable by EM (Zhao *et al.*, 2017). This development was expanded through the invention of high-throughput ExM (HighExM), allowing for the combination of ExM and drug screening and thus enabling pharmaceutical applications (Day *et al.*, 2023). Another high-throughput drug screening method was developed by combining a superhydrophobic microwell array plate (SMAP) with proExM (Xie *et al.*, 2023).

The use of ExM to facilitate a different method is a further application of ExM, as it is used in expansion sequencing (ExSeq), which first expands the sample to make the RNAs more accessible for fluorescent in situ sequencing (Alon *et al.*, 2021). The same is true for expansion proteomics (ProteomEx), which uses ExM to enable spatially resolved proteomics (Li *et al.*, 2022).

1. 4 Aims of the study

In contrast to other super-resolution microscopy techniques, ExM is a relatively new method that brings together two disciplines: chemistry and molecular biology. As a result, the method still offers many opportunities for further development, and there is still a lack of in-depth understanding of the chemical and molecular biological aspects.

Due to the proteolytic digestion and the at least 64-fold dilution of the fluorophores, there is an enormous loss of labels after expansion of the sample. Another aspect is the distortion of the sample after expansion. Due to the digestion of the original biological structure and the subsequent expansion, it is necessary to ensure that the labels remain in a relative position true to the original structure. So far, ExM lacks easy to use tools to assess the distortion.

For this reason, this study has the following objectives:

First, the development of new tools for ExM. This includes the development of a trifunctional dye to improve signal preservation after expansion. Among the different functionalities of the dye is the moiety for gel anchoring for better incorporation of the label into the polyacrylamide network. Also, the development of an intrinsic ruler using tobacco mosaic virus (TMV) particles to determine the distortion and calculate the expansion factor (Figure 10).

Secondly, this study will help to better understand the mechanism of ExM, especially what contributes to efficient grafting and incorporation of labels, thus bridging the gap between the biological and chemical perspectives.

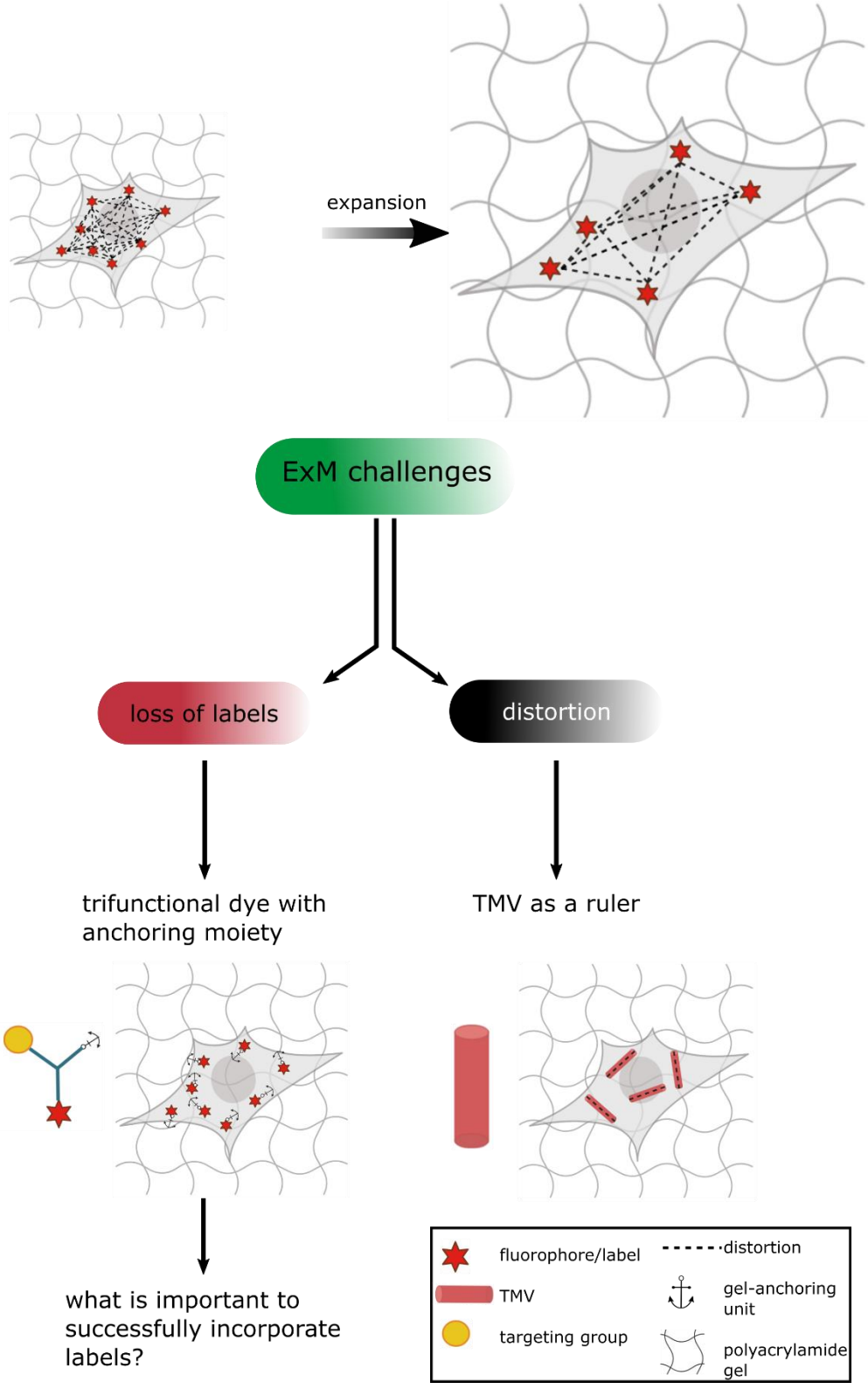

Figure 10: Aims of this study.

After expansion of a labeled structure of interest, labels (red stars) are lost due to proteolytic digestion and radical-induced polymerization. The relative position between labels (dashed lines) may be distorted after expansion. These two challenges are addressed in this study by developing a trifunctional dye with an anchoring moiety for direct incorporation into the gel and by developing a ruler to measure the distortion.

2. Results and Discussion

2.1 Development of the trifunctional rhodamine dye BG-TMR-MA for ExM

From the beginning of its development retaining the fluorescence signal has been a major problem in ExM. For a detailed description see section 1.3.2 'challenges for ExM'. For This reason many laboratories focused on enhancing the signal after expansion by different means. For instance, by extensively labeling the target structure before expansion with different antibodies directed against the same target, which has been proven advantageous for ExSTED (Gao *et al.*, 2018). Instead of extensively increasing the signal prior to expansion, an alternative strategy is to focus on effectively linking the target structure to the polyacrylamide matrix. It is crucial to anchor the label efficiently for signal retention. One potential solution is the use of trifunctional linkers that incorporate three essential functionalities: a dye moiety, target delivery, and gel anchoring.

The aim of my research project was to further improve this subject by developing a small (< 1 kDa) trifunctional probe, equipped with a polymerizable monomer, a bright and stable fluorescent rhodamine dye and a covalent targeting via SNAP-tag. The probe is composed of BG, which reacts with SNAP-tagged proteins, resulting in the covalent attachment of the label. The core of the probe is the fluorescent dye TMR and it additionally contains a methacrylate (MA) group that is incorporated into the growing polymer chain. Because of its components the trifunctional probe is from now on called BG-TMR-MA (benzylguanine-tetramethylrhodamine-methacrylamide) (Figure 11).

Chemical synthesis and purification of BG-TMR-MA was carried out by my collaborator Dr. Isabelle Heing-Becker under supervision of Prof. Dr. Kai Licha and Dr. Carlo Fasting in the group of Prof. Dr. Rainer Haag at the organic chemistry department of the Freie Universität Berlin. To attach our dye to the target protein, we selected the SNAP-tag due to its stable covalent thioether bond created between the protein and the label (Keppler *et al.*, 2004), the specificity of the labeling reaction and the reduced labeling error when compared to antibodies. The target protein is expressed as SNAP-tagged fusion protein

either via transient transfection or in a stable cell line. SNAP-tagged proteins act as self-labeling proteins and reaction with BG leads to attachment under release of guanine. Rhodamines have a high fluorescence quantum yield and photostability (Beija, Afonso and Martinho, 2009). Importantly, it has been shown that they survive the polymerization process very well (Chozinski *et al.*, 2016) and are therefore ideal candidates for the design of a novel ExM probe. Here, 6-carboxytetramethylrhodamine was chosen as the dye and starting point for the synthesis due to the presence of an additional carboxylic acid group in the carboxyphenyl ring, which can be activated and functionalized for the attachment of BG. As shown in Figure 11 the additional carboxyl group was activated with disuccinimidyl carbonate (DSC) for the attachment of BG. The second carboxyl group was masked with a mono-tert-butyloxycarbonyl (boc)-protected piperazine after it had been activated with hexafluorophosphate azabenzotriazole tetramethyl uronium (HATU) to convert it into an active ester. Masking was necessary to prevent intramolecular spirocyclization of the dye, which leads to the formation of a non-fluorescent spirolactone (Lavis, 2017). After removal of the Boc protecting group with trifluoroacetic acid (TFA), the MA group was attached to the piperazine at the remaining carbonyl group in the last step. The final product BG-TMR-MA absorbs at 565 nm and emits at 590 nm (Figure S 1).

The dye initially lacked a methyl group in its polymerizable group and consisted of an acrylate group instead of an MA group as it evolved. However, the early BG-TMR-acrylate variant exhibited lower stability towards pre-polymerization and a decrease in signal intensity after short-term storage (Figure S 2). Thus, the acrylate group was substituted with the MA group and para-methoxyphenol was added as an inhibitor to prevent the dye from self-polymerizing.

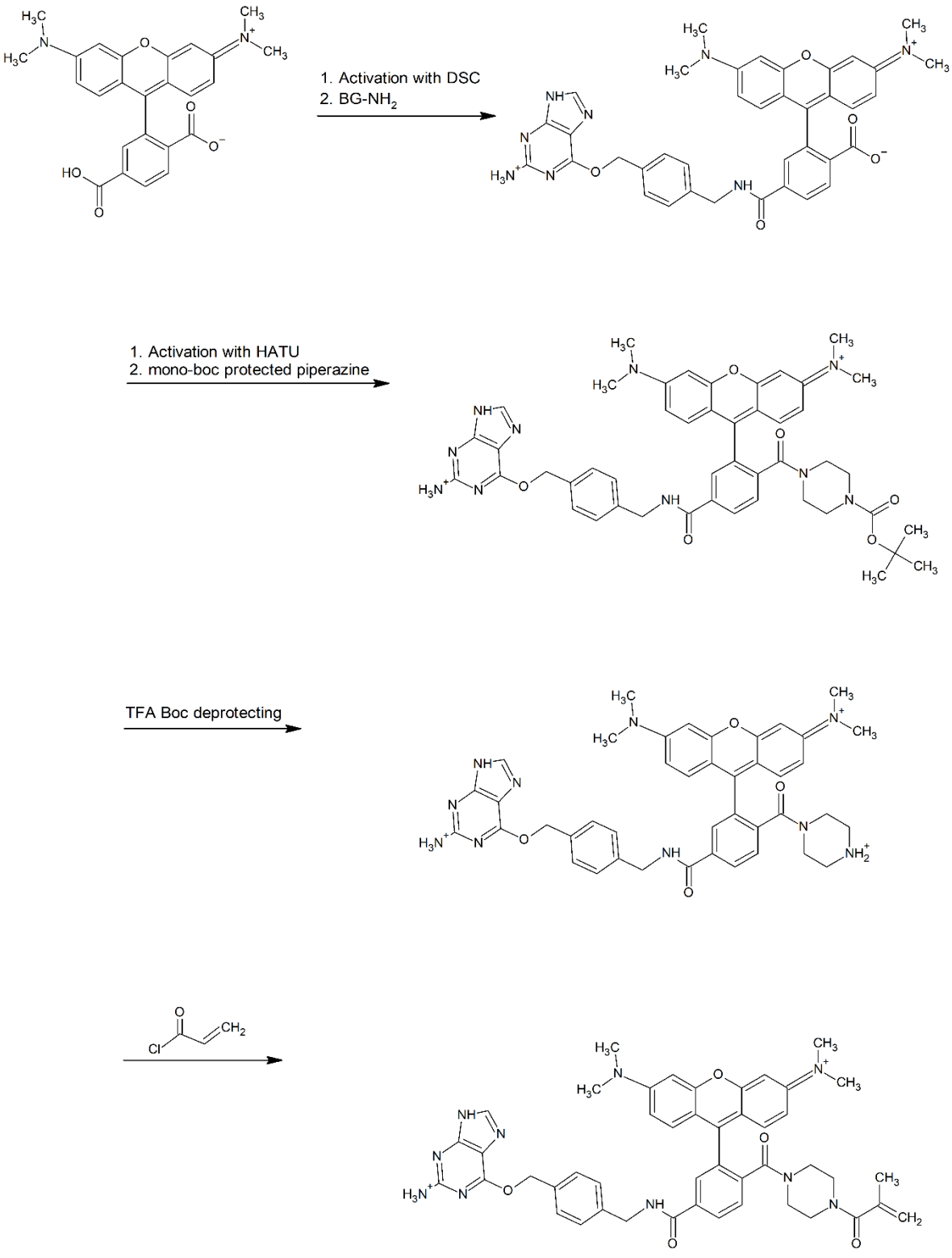

Figure 11: Synthesis of BG-TMR-MA.

Starting from 6-carboxytetramethylrhodamine, BG-TMR-MA was synthesized via the Boc-protected intermediate (BG-TMR-Boc). Synthesis was performed by Dr. Isabelle Heing-Becker.

2.1.1 Characterization of BG-TMR-MA

To characterize BG-TMR-MA before performing cellular experiments the absorption at 562 nm was measured with a plate reader after adding the polyacrylamide gel components to the dye in solution (Figure 12a). For comparison, the same experiment was performed using the commercially available dye SNAP-Cell TMR-Star, which has a very similar structure. SNAP-Cell TMR-Star consists of a TMR core but instead of BG it has an amino chloropyrimidine group (Figure S 4), which can also be recognized by SNAP-tagged proteins (Cole, 2013). An important difference is the absence of the MA group. However, measurement of absorption in aqueous solution after addition of the chemicals required for the ExM process, such as APS, TEMED and MS showed that both dyes displayed only a slight loss of absorption during the process. In addition, there was little absorption loss in the fully polymerized gel, which was of particular interest for its applicability to ExM and proved that both dyes could resist the polymerization process very well (Figure 12).

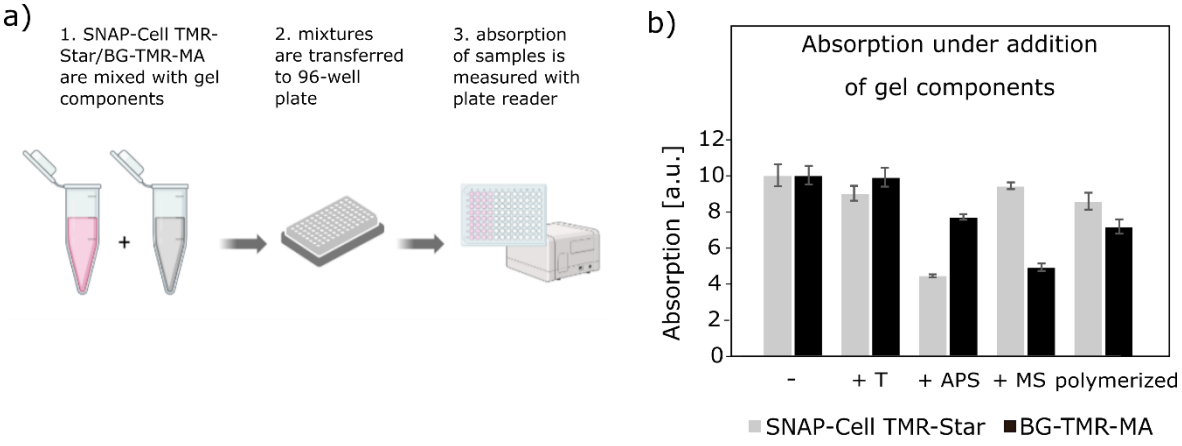

Figure 12: Absorption of SNAP-Cell TMR-Star versus BG-TMR-MA under addition of polyacrylamide gel components.

a) Workflow of absorption measurement. b) The absorption of SNAP-Cell TMR-Star versus BG-TMR-MA was measured (absorption of the dyes in SNAP-dye buffer, addition of TEMED, addition of APS, addition of monomer gelling solution (MS), polymerized gel, which includes MS, APS and TEMED). Error bars represent standard deviation (SD), *n*=3.

After testing the suitability of BG-TMR-MA for the ExM process, I tested its staining ability for different biological targets (Figure 13). For this purpose, SNAP-tagged target proteins were transiently expressed by transfection with SNAP fusion protein constructs, once as SNAP-clathrin-light-chain-yellow-fluorescent-protein (SNAP-CLC-YFP) (Figure 13a) and

furthermore as SNAP-tubulin (Figure 13b). Additionally, two cell lines stably expressing SNAP-tagged proteins were used: U2OS-Nucleoporin96-SNAP (U2OS-NUP96-SNAP) cells (Figure 13c) and NRK49F-Septin2-SNAP (NRK49F-S2-SNAP) cells (Figure 13d). No matter whether the target protein was transfected or stably expressed, and regardless of the target protein itself, BG-TMR-MA showed specific staining and a high fluorescence signal.

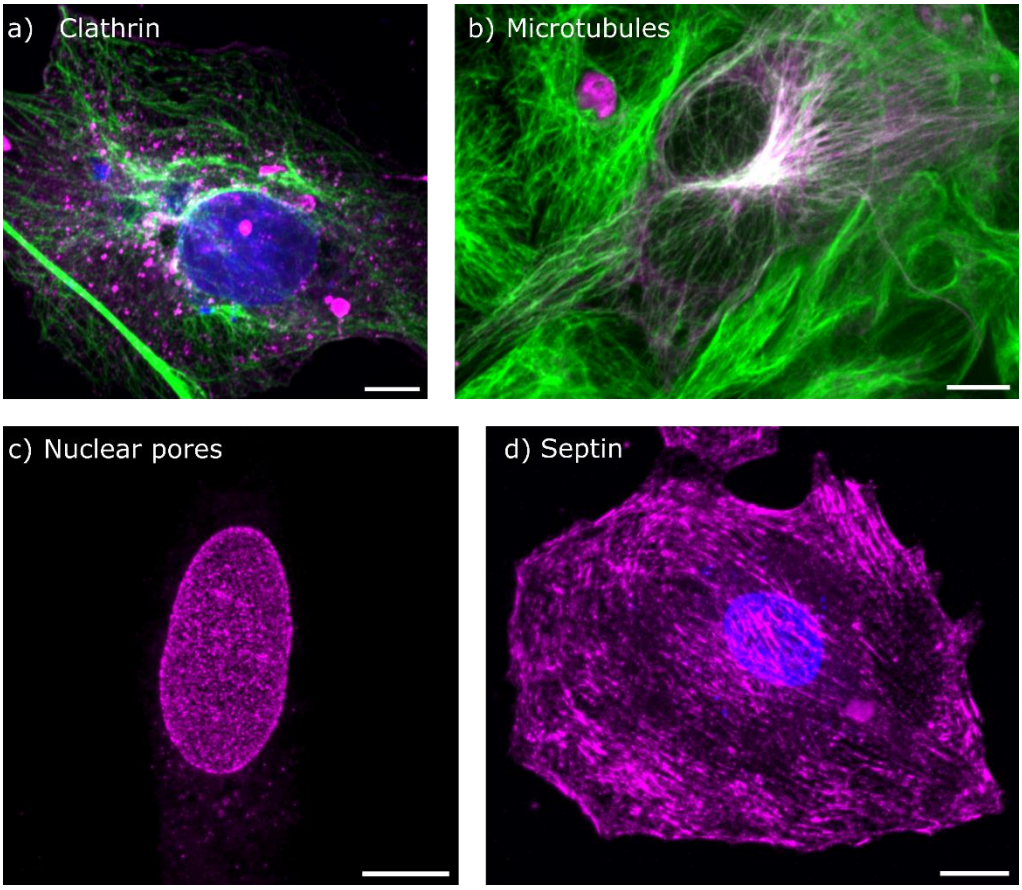

Figure 13: Labeling of different cellular targets with BG-TMR-MA.

a) Fluorescence micrograph of a SNAP-CLC-YFP expressing cell. Microtubules were stained with primary anti-alpha-tubulin, anti-beta-tubulin antibodies and secondary anti-mouse Abberior Star Red antibody (green). SNAP-tagged Clathrin was stained with BG-TMR-MA (magenta). Nuclear staining with DAPI. b) Fluorescence micrograph of microtubules stained with primary anti-alpha-tubulin, anti-beta-tubulin antibodies and detected via secondary anti-mouse Abberior Star Red antibody (green). Additionally, cells were transfected with SNAP-tubulin and stained with BG-TMR-MA (magenta). SNAP-tubulin expressing cell in the middle of the image is white due to overlaid BG-TMR-MA signal (magenta) and immunofluorescence signal (green). c) Fluorescence micrograph of nuclear pores stained with BG-TMR-MA. d) Fluorescence micrograph of a Septin2-SNAP expressing cell labelled with BG-TMR-MA. Nuclear staining with DAPI. Image (d) acquired by Maria-Anna Kirmpaki. Scale bars are 10 µm.

For the following experiments, the stable cell line U2OS-NUP96-SNAP was preferred and some experiments were performed using the SNAP-CLC-YFP construct. Nuclear pores were chosen because they are often used as a reference standard in super-resolution microscopy due to their stereotypical ring-like structure with a diameter of ~100 nm (Winey *et al.*, 1997). They consist of an inner nucleoplasmic ring and an outer cytoplasmic ring. Each nuclear pore complex (NPC) theoretically contains 32 SNAP-tags, as each of the 8 corners of the ring is composed of 2 nucleoporin (NUP) 96 proteins (Thevathasan *et al.*, 2019) (Figure 14a). BG-TMR-MA provides specific staining of nuclear pores throughout the entire nucleus as shown in Figure 14b-c. To characterize the staining properties of the trifunctional dye I compared it to several commercially available SNAP-dyes, but focused on SNAP-Cell TMR-Star due to its structural similarity (Figure S 4), as previously mentioned. Both dyes are cell-permeable because they are uncharged and can thus be used to label living cells. Therefore, the dyes were incubated in the culture medium for 5 min or 30 min at 37°C, followed by washing and fixation. Interestingly, 5 min versus 30 min of live cell labeling had no significant effect on the fluorescence intensity of BG-TMR-MA, whereas a longer incubation time of SNAP-Cell TMR-Star dramatically affected the labeling, increasing the intensity by an order of magnitude after 30 min (Figure 14d-e). Additionally, there were no significant differences between any of the dyes when labeling living cells for 30 min versus post-fixation labeling. Overall, BG-TMR-MA showed a significantly higher signal intensity compared to SNAP-Cell TMR-Star. When comparing BG-TMR-MA with other SNAP dyes, such as JF-SNAP-552, SNAP-Cell 647-SIR, and SNAP-Surface AF647, it is evident that BG-TMR-MA demonstrated remarkably high brightness (Figure 14f). Specifically, BG-TMR-MA showed the significantly highest fluorescence intensity among all SNAP dyes mentioned above (Figure 14g).

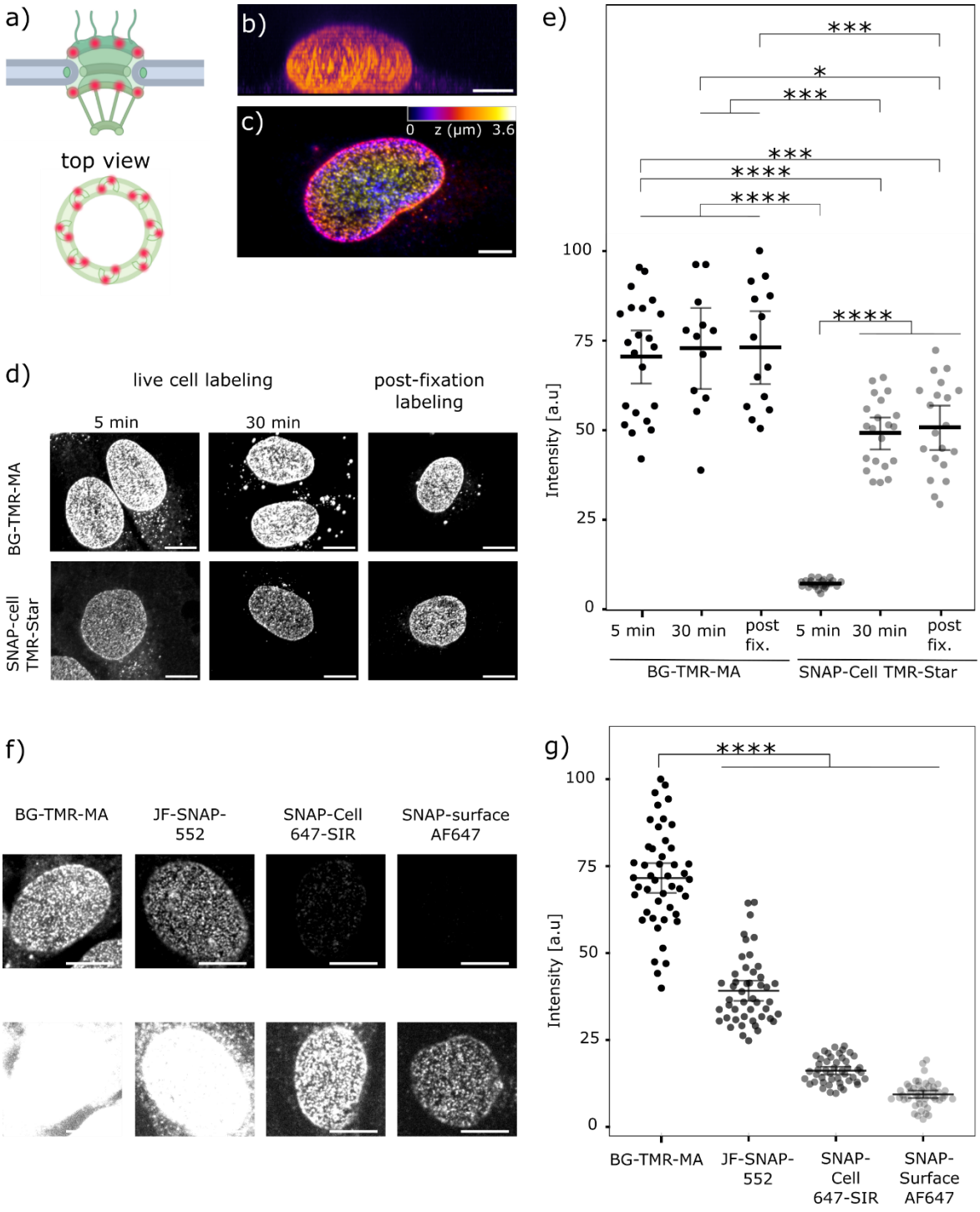

Figure 14: Characterization of the staining properties of BG-TMR-MA by using nuclear pores.

a) Schematic nuclear pore complex with cytoplasmic ring and nuclear ring, including nuclear basket, spanning the membrane. The U2OS-NUP96-SNAP cell line used here has 16 SNAP-tags per ring (see top view of ring). Red bullets represent SNAP-tagged NUP96 proteins. b) Side view of z-stacks taken from a NUP96-SNAP expressing cell labeled with BG-TMR-MA. c) Depth encoded z-stacks of the same cell as in b). The color represents the z-depth. d) Live cell labeling with 5min and 30 min incubation time vs. post fixation labeling of nuclear pores with SNAP-Cell TMR-Star and BG-TMR-MA. Same intensity scales for fluorescence micrographs are shown, except of SNAP-Cell TMR-Star-5 min, which is represented with a 5 times higher intensity. e) Quantification of fluorescence

intensity of NUP96-SNAP-expressing cells labeled live or after fixation with SNAP-Cell TMR-Star or BG-TMR-MA. Shown is the mean and error bars represent 95% confidence interval. Statistical analysis was done via T-Test. f) Fluorescence micrographs of NUP96-SNAP-expressing cells stained with different SNAP dyes: BG-TMR-MA, JF-SNAP-552, SNAP-Cell 647-SIR and SNAP-Surface AF647. Images are shown at two different intensity scales to emphasize the relative difference in intensity. g) Quantification of fluorescence intensity of NUP96-SNAP-expressing cells labeled with BG-TMR-MA, JF-SNAP-552, SNAP-Cell 647-SIR and SNAP-Surface AF647. Shown is the mean and error bars represent 95% confidence interval, *n*=47. Statistical analyses were conducted using unpaired T-Tests under the assumption of unequal variances. Scale bars are 5 µm (b, c) and 10 µm (d, f).

Rhodamines and their derivatives are frequently utilized in STED microscopy, including the commercially available far-red dye Abberior Star Red. Although the focus of this study was not to develop a specific STED dye, I discovered that BG-TMR-MA has the potential to be used for STED imaging (Figure S 5). Therefore, it could be considered for future use in ExSTED imaging. Either way, I investigated the staining quality and super-resolution imaging capabilities of BG-TMR-MA and therefore compared its performance in ExM of nuclear pores with STED microscopy of unexpanded NUPs stained with commercially available STED dyes. For STED imaging, either NUP96-GFP cells were stained via primary antibodies against GFP and secondary antibodies coupled to Abberior Star Red (Figure 15a) or NUP96-SNAP cells were stained with SNAP-Cell 647-SIR (Figure 15b). For confocal spinning disc imaging, I stained NUP96-SNAP cells with BG-TMR-MA and performed ExM after anchoring with 1 mg/mL AcX. After expanding the samples, they were imaged using a spinning disc confocal microscope. The fixed pixel size of approximately 100 nm/pixel, which equates to around 33 nm/pixel after expansion with a factor of 3, resulted in pixelated images. In contrast, STED microscopy images, where the pixel size could be selected and set to 10 nm, were much clearer. However, a clear drop in fluorescence in the middle of a ring-shaped structure for individual nuclear pores could be observed with ExM confocal imaging, which points out the super-resolution imaging capabilities of BG-TMR-MA (Figure 15c). In all cases a similar dip in fluorescence was observed. It can be concluded that BG-TMR-MA in combination with AcX provides high resolution and brightness in ExM experiments.

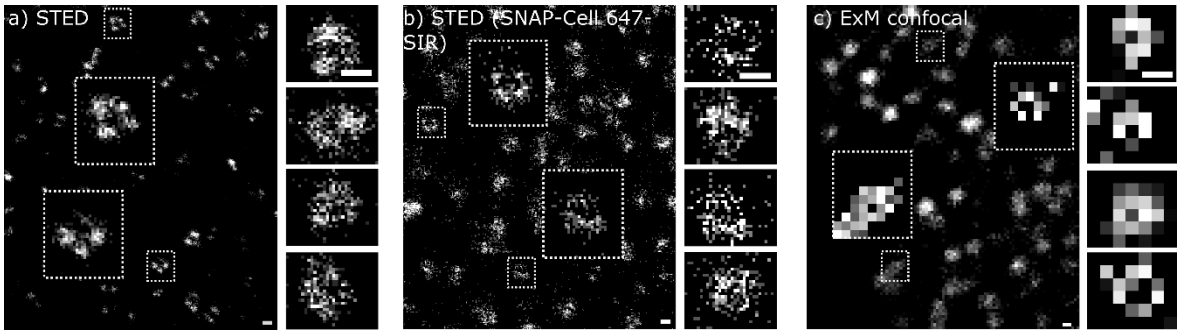

Figure 15: Comparison of ExM confocal imaging of BG-TMR-MA stained nuclear pores with STED imaging of nuclear pores stained with commercially available dyes.

a) STED of NUP96-GFP labeled with an anti-GFP primary antibody and detected with an Abberior Star Red conjugated secondary antibody. b) STED of NUP96-SNAP labeled with SNAP-Cell 647-SIR. Zoom-in of boxed nuclear pores. c) Fluorescence micrograph of NUP96-SNAP stained with BG-TMR-MA after expansion under presence of 1 mg/mL AcX and imaged in spinning disc confocal microscopy. Insets on the right were taken from different cells. Scale bars are 100 nm.

2.1.2 ExM with BG-TMR-MA without the use of additional anchoring reagent

We assumed that the MA group of the trifunctional dye will be incorporated into the hydrogel and that it should be sufficient to successfully anchor the dye in the gel and increase the signal intensity because of the increased probability of labeled and copolymerized fragments. During an ExM experiment with BG-TMR-MA without additional anchoring reagents, I observed only a slight improvement in signal intensity (Figure 16a) compared to the undetectable signal of SNAP-Cell TMR-Star (Figure 16b). This was unexpected given the dye's linkage to the hydrogel matrix via its acrylate group, which should have led to enhanced signal retention.

Figure 16: ExM without using additional crosslinker.

a) Fluorescence micrograph of a SNAP-CLC-YFP expressing cell stained with BG-TMR-MA after ExM without crosslinker. b) Fluorescence micrograph of a SNAP-CLC-YFP expressing cell stained with SNAP-Cell TMR-Star after ExM without crosslinker. Inset shows DAPI staining of the same cell. Scale bars are 10 µm.

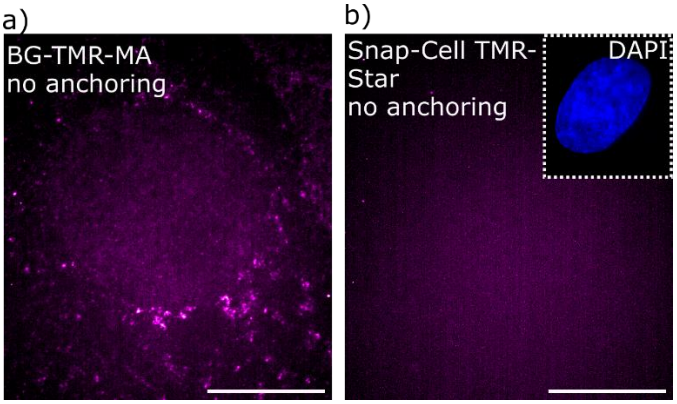

To determine the cause of the signal loss, I first optimized the staining process and tested various dye concentrations ranging from 5 nM to 5 µM. It was observed that dye concentrations exceeding 1 µM led to excessive background signal, while those in the nanomolar range produced more specific yet less intense signals. To reduce background signal, successive stainings were performed by one round of nanomolar dye concentration and washing followed by a second round of staining and washing (Figure S 3). Although the signal intensity increased after the second round of staining, it was still ineffective in retaining the signal after expansion. This means that even an intense pre ExM staining resulted in high signal loss after expansion. It is commonly suggested in literature to utilize low micromolar concentrations of 0.3-0.5 µM for SNAP-dyes, except for the fluorogenic SNAP dye SNAP-Cell 647-SIR, which can be used in concentrations up to 5 µM (Lukinavičius, Reymond and Johnsson, 2015). Nonetheless, for BG-TMR-MA, the ideal concentration for obtaining both specific and high intensity staining was found to be 1 µM. However, despite optimizing the staining protocol with the trifunctional dye, the signal remained unsatisfactory after expansion. The only plausible explanation for this result is insufficient anchoring.

2.1.3 Comparison of BG-TMR-MA with SNAP-Cell TMR-STAR and BG-TMR-Boc under addition of AcX

To investigate the cause of the weak signal after expansion, I tested the hypothesis that insufficient anchoring may be the reason. This was done by adding the crosslinker AcX. AcX crosslinks proteins throughout the cell in a random manner into the gel by equipping them with a polymerizable monomer via an N-hydroxysuccinimide (NHS)-ester reaction between amine residues of the proteins and AcX. For this purpose, I performed ExM experiments while gradually increasing AcX concentration from 0.01 mg/mL to 1 mg/mL. The samples were imaged using a spinning disc confocal microscope at various stages of the ExM process. BG-TMR-MA was compared not only with SNAP-Cell TMR-Star but also with BG-TMR-Boc. BG-TMR-Boc is an intermediate from the dye synthesis (Figure 11) that lacks the MA-group and instead contains a Boc protecting group. The latter cannot be polymerized into the gel, but it is similar to the MA group in terms of size and polarity. The initial imaging

was performed after staining the NUP96-SNAP cells with BG-TMR-MA, SNAP-Cell TMR-Star or BG-TMR-Boc. The second imaging was carried out after the polyacrylamide gel was polymerized, the third imaging after the hydrogel was digested and the final imaging was performed as usual after the gel was expanded in water (Figure 17a). After staining and gelation, fluorescence intensity was comparable and not dependent on the AcX concentration among all tested dyes. In general, higher AcX concentrations resulted in greater signal retention for all three dyes after digestion and expansion (Figure 17b, c, e, f). As expected, the trifunctional dye BG-TMR-MA exhibited an increased signal retention, which was roughly ten times higher than SNAP-Cell TMR-Star (Figure 17d) and significantly higher compared to BG-TMR-Boc in the presence of 1 mg/mL AcX (Figure 17g).

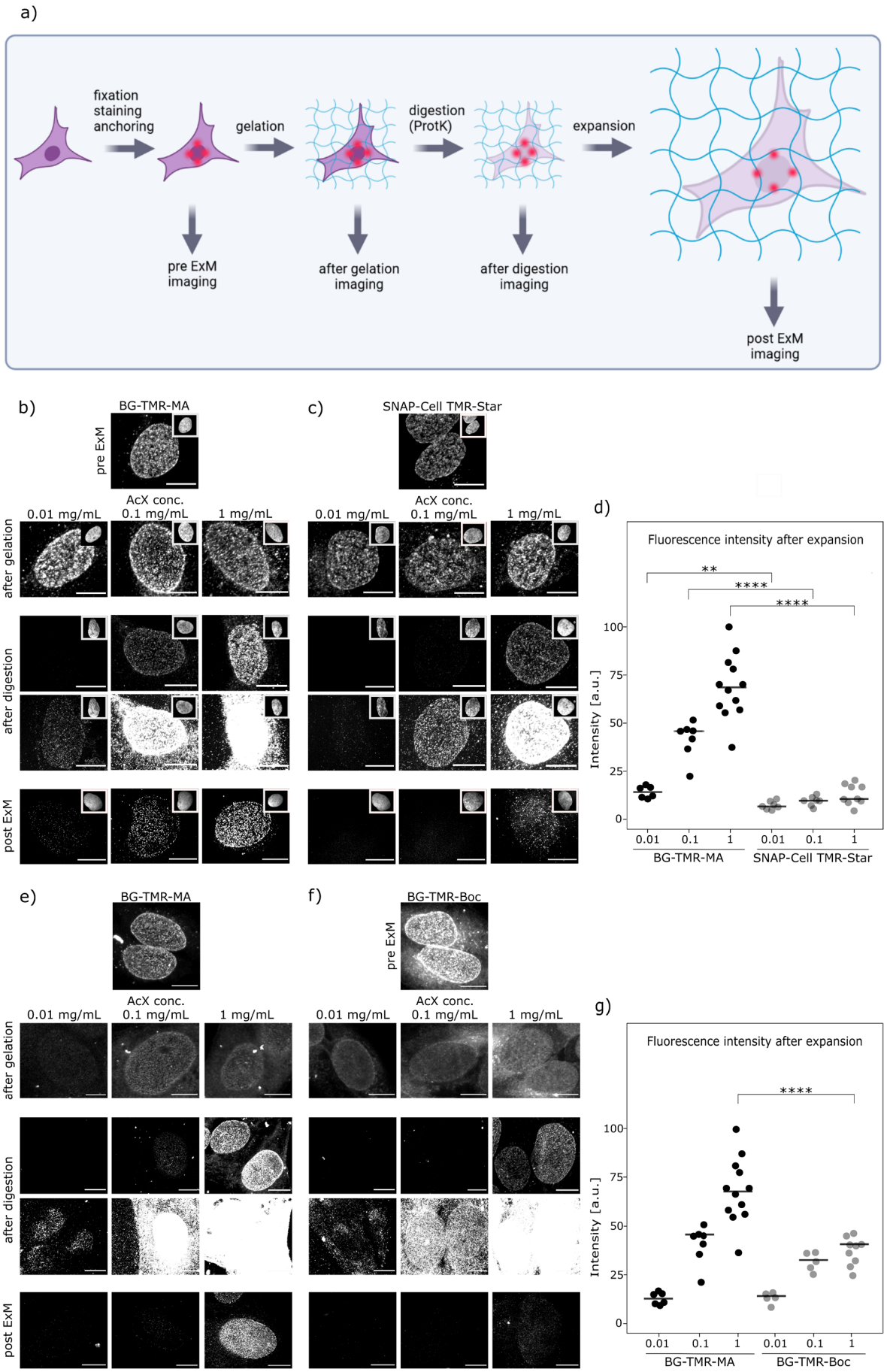
a)
fixation
staining
anchoring
gelation
digestion
(ProtK)
expansion
pre ExM
imaging
after gelation
imaging
after digestion
imaging
post ExM
imaging
b)
BG-TMR-MA
pre ExM
AcX conc.
0.01 mg/mL
0.1 mg/mL
1 mg/mL
after gelation
after digestion
post ExM
c)
SNAP-Cell TMR-Star
d)
Fluorescence intensity after expansion
**
****
****
Intensity [a.u.]
100
75
50
25
0
0.01
0.1
1
BG-TMR-MA
SNAP-Cell TMR-Star
e)
BG-TMR-MA
f)
BG-TMR-Boc
g)
Fluorescence intensity after expansion
****
BG-TMR-MA
BG-TMR-Boc

Figure 17: Comparison between BG-TMR-MA and SNAP-Cell TMR-Star or BG-TMR-Boc in the presence of different AcX concentrations.

a) Schematic representation of ExM process and imaging steps. Red bullets represent stained nuclear pores. Confocal spinning disc imaging was performed after staining, after gelation, after digestion and after expansion. b), e) Representative confocal fluorescence micrographs of NUP96-SNAP expressing cells stained using BG-TMR-MA after staining (pre ExM), gelation, digestion and expansion (post ExM) in the presence of different AcX concentrations. c) Representative confocal fluorescence micrographs of NUP96-SNAP expressing cells stained using SNAP-Cell TMR-Star after staining (pre ExM), gelation, digestion and expansion (post ExM) in the presence of different AcX concentrations. The fluorescence micrographs imaged after digestion are shown at two different intensity scales to emphasize the relative difference in intensity. Scaling is identical for BG-TMR-MA and SNAP-Cell TMR-Star, respectively for the top and bottom row to emphasize the relative intensity. Boxes show DAPI staining of the same cell. d) Quantification of fluorescence intensity of stained cells after expansion between BG-TMR-MA and SNAP-Cell TMR-Star in dependence of the AcX concentration. f) Representative confocal fluorescence micrographs of NUP96-SNAP expressing cells stained using BG-TMR-Boc after staining (pre ExM), gelation, digestion and expansion (post ExM) in the presence of different AcX concentrations. The fluorescence micrographs imaged after digestion are shown at two different intensity scales to emphasize the relative difference in intensity. Scaling is identical for BG-TMR-MA and BG-TMR-Boc, respectively for the top and bottom row to emphasize the relative intensity. g) Quantification of fluorescence intensity of stained cells after expansion between BG-TMR-MA and BG-TMR-Boc in dependence of the AcX concentration. Statistical analysis was done via an unpaired T-Test under the assumption of unequal variance. Scale bars are 10 µm.

This observation can be attributed to the MA group causing more labeled fragments to be incorporated into the gel. Even when proteinase K cuts between anchoring sites, fragments containing a trifunctional dye are always anchored via the MA group, thus avoiding the risk of being washed out (Figure 18a). This is in contrast to fragments that are labeled with SNAP-Cell TMR-Star or BG-TMR-Boc, but are accidentally not anchored via AcX (Figure 18b).

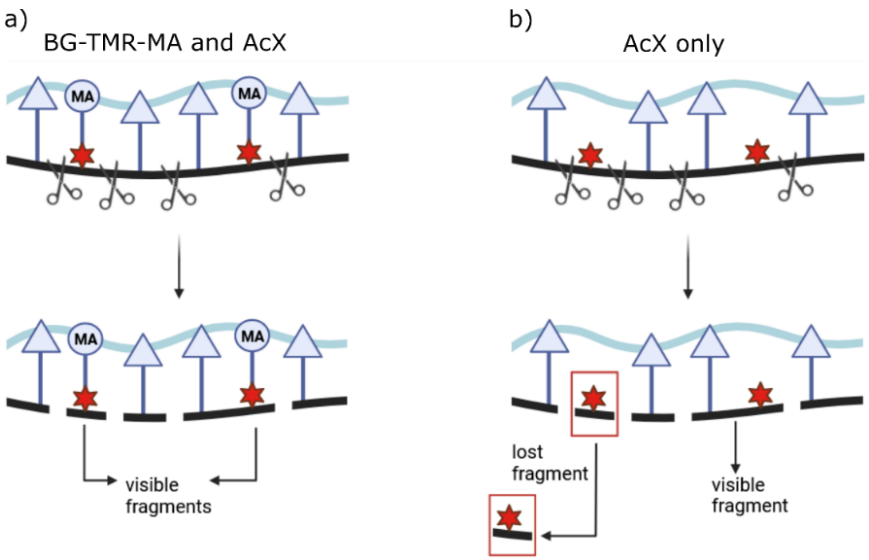

Figure 18: Combined crosslinking of BG-TMR-MA and AcX results in more visible fragments after ExM compared to using AcX alone.

a) Fragments labeled with BG-TMR-MA (asterisk with bullet) give a fluorescence signal after expansion even if proteinase K cuts between AcX anchor points (triangle). b) Fragments labeled with SNAP-Cell TMR-Star or BG-TMR-Boc (asterisk) are visible after ExM only when proteinase K cuts out fragments that contain both an AcX anchor point (triangle) and the label. The black line represents the surface of the target protein, while the blue line represents the polymer chain.

The conclusion that the MA-group is responsible for increased dye retention, was further strengthened by the finding that BG-TMR-MA staining of septins in a Septin2-SNAP stable cell line also showed higher fluorescence intensity after expansion compared to BG-TMR-Boc under presence of 1 mg/mL AcX (Figure 19). The results are therefore transferable to other biological structures, indicating that the increased signal intensity is due to the use of an MA-anchored dye and is independent of the target structure.

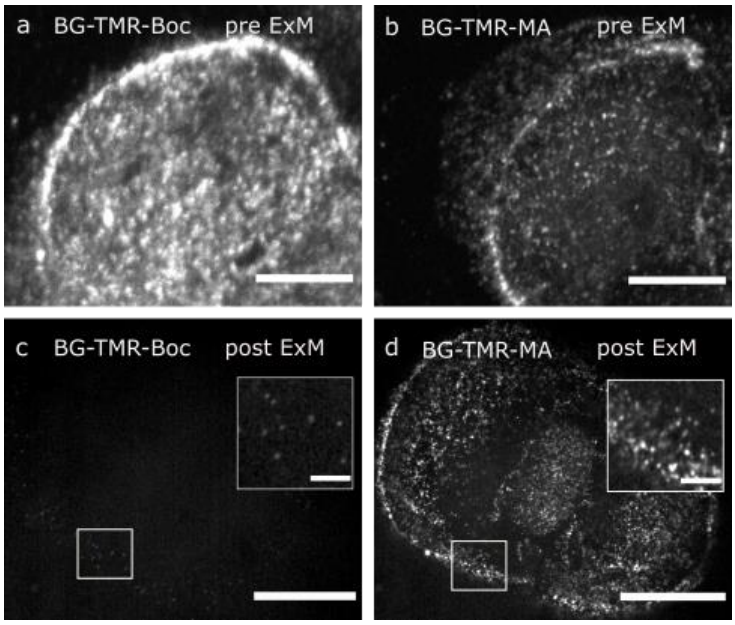

Figure 19: Comparison of pre and post ExM spinning disc confocal imaging between BG-TMR-Boc and BG-TMR-MA stained septins.

a)-b) Pre ExM comparison of fluorescence micrographs of NRK52E cells, stably expressing Septin2-SNAP and stained with BG-TMR-Boc and BG-TMR-MA. c)-d) Post ExM comparison of fluorescence micrographs of NRK52E cells, stably expressing Septin2-SNAP and stained with BG-TMR-Boc and BG-TMR-MA. Anchoring was performed with 1 mg/mL AcX. Zoom-in of boxed regions demonstrate higher fluorescence intensity and more cellular details in BG-TMR-MA labeled cell. Same intensity scalings for the respective images pre and post ExM. Scale bars are 10 µm and 150 nm in the insets.

2.1.4 Local delivery of AcX

Thus, a high monomer density at the target structure and at the label seemed to be crucial for signal preservation, so that as many anchored labeled fragments as possible remain after digestion. To further investigate this observation, I increased the monomer density at the target surface by directly delivering AcX in the close vicinity of BG-TMR-MA. In order to do this, I labeled SNAP- and GFP-directed nanobodies with AcX (anti-SNAP-nb-AcX, anti-GFP-nb-AcX) and expressed a SNAP- and YFP-tagged clathrin-light chain construct (SNAP-CLC-YFP (Figure S 6) (Jones *et al.*, 2011)) in cells. YFP can be recognized by GFP-nanobodies. In this manner, AcX should be directed to the protein of interest, in this case clathrin, via the labeled nanobodies. Successful overexpression of SNAP-CLC-YFP and specific clathrin staining using BG-TMR-MA was demonstrated by co-staining clathrin with an anti-clathrin heavy chain (CHC) antibody conjugated to AF647 (Figure 20).

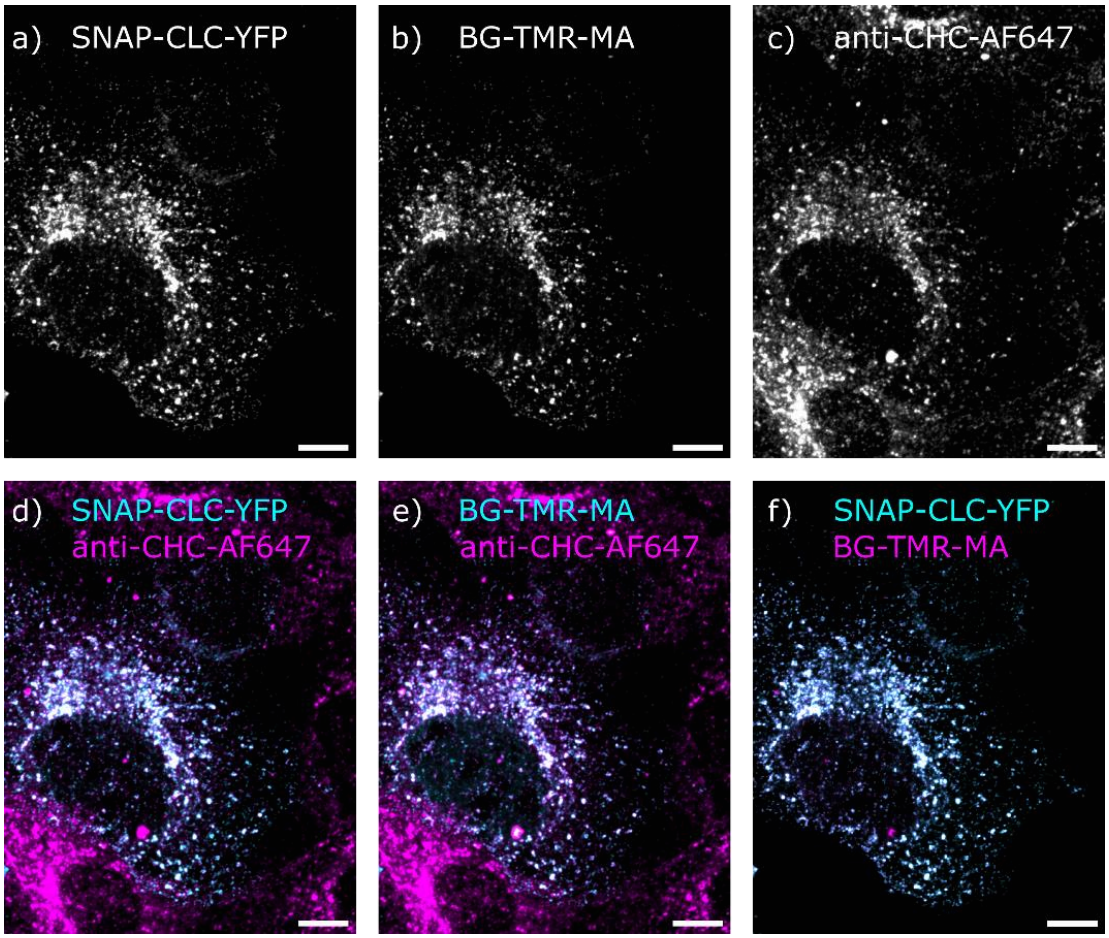

Figure 20: Expression of SNAP-CLC-YFP in CV1 cells.

a) Fluorescence micrograph of a SNAP-CLC-YFP expressing cell. b) Fluorescence micrograph of a SNAP-CLC-YFP expressing cell stained with BG-TMR-MA. c) Same region of interest as in a) and b) stained via immunofluorescence against clathrin using an anti-CHC-AF647 antibody. d) Overlay of a) and c) with SNAP-CLC-YFP expression shown in cyan and anti-CHC-AF647 staining shown in magenta. e) Overlay of b) and c) with BG-TMR-MA staining shown in cyan and anti-CHC-AF647 staining shown in magenta. f) Overlay of a) and b) with SNAP-CLC-YFP expression shown in cyan and BG-TMR-MA staining shown in magenta. Scale bars are 10 µm.

Since AcX does not fluoresce, specificity of nanobody binding to their targets had to be verified. Therefore, the specific binding of anti-GFP and anti-SNAP nanobodies was evaluated by labeling the respective nanobodies with Abberior Star Red and staining Septin2 in a stable Septin2-GFP (NRK49F-S2-GFP) and a stable Septin2-SNAP (NRK49F-S2-SNAP) cell line (Figure 21). Although Abberior Star Red coupled anti-GFP-nanobodies showed some nuclear background, both nanobodies proved to bind specifically to their targets and were therefore considered suitable for further experiments.

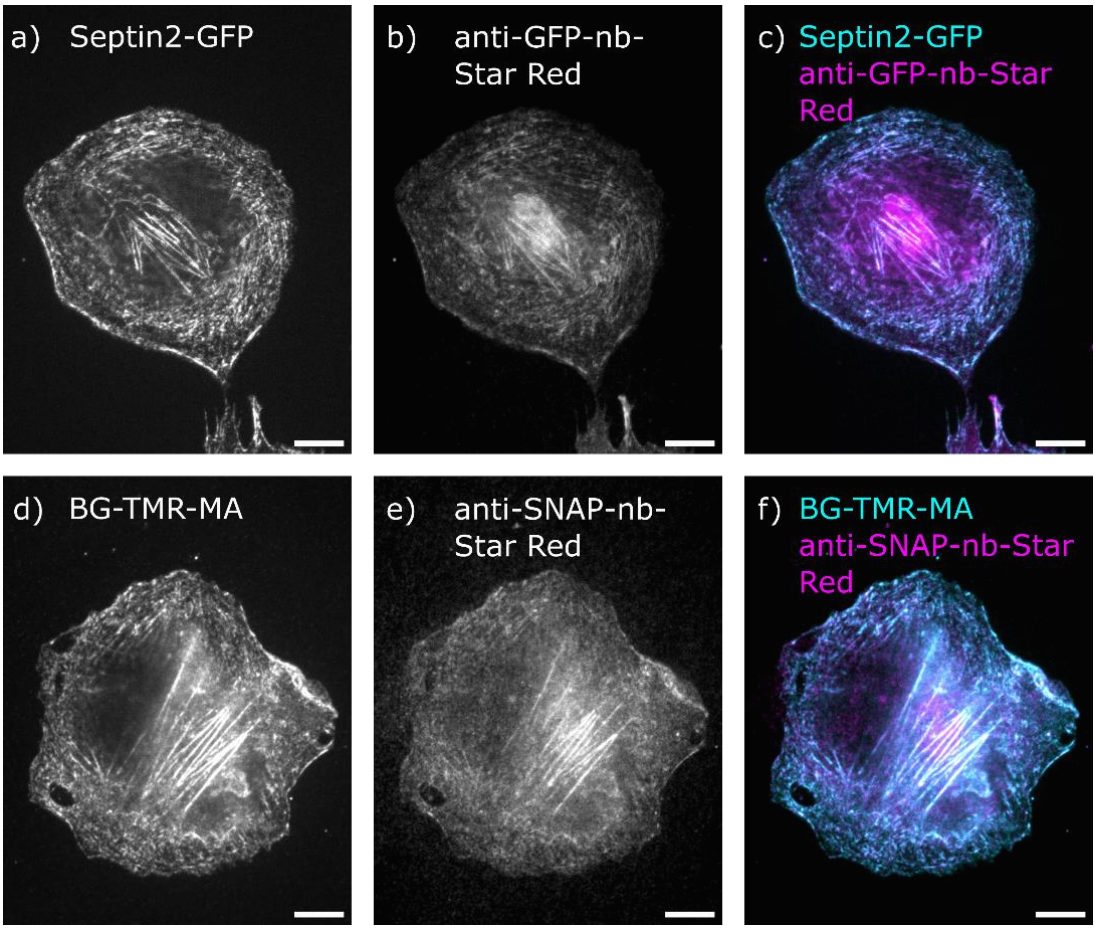

Figure 21: Anti-GFP and anti-SNAP nanobody binding controls.

a) Fluorescence micrograph of a NRK49F cell stably expressing Septin2-GFP. b) Fluorescence micrograph of the same Septin2-GFP expressing cell stained with an anti-GFP nanobody coupled to Abberior Star Red. c) Overlay image of a) and b) with Septin2-GFP signal in cyan and the anti-GFP-nb-Star Red signal in magenta. d) Fluorescence micrograph of a NRK49F cell stably expressing Septin2-SNAP stained with BG-TMR-MA. e) Fluorescence micrograph of the same Septin2-SNAP expressing cell as in d) stained with an anti-SNAP nanobody coupled to Abberior Star Red. f) Overlay image of d) and e) with BG-TMR-MA signal in cyan and the anti-SNAP-nb-Star Red signal in magenta.

In addition to the monomer introduced by BG-TMR-MA, the AcX-labeled anti-SNAP and anti-GFP nanobodies should provide the target (here clathrin) with more polymerizable monomers directly at the target site and in close proximity to the label. It is important to note that no global AcX was added, which means that only the target structure, but no other cellular structure, was anchored in the hydrogel (Figure 22a). Indeed, I found that delivering AcX directly to the target and close to BG-TMR-MA was sufficient to ensure a high signal retention and significantly increase signal intensity compared to using BG-TMR-MA alone as anchoring moiety (Figure 22b-c). When I compared the signal retention to

SNAP-Cell TMR-Star, I found that using AcX-coupled nanobodies also increased the signal intensity for SNAP-Cell TMR-Star stained clathrin in contrast to using SNAP-Cell TMR-Star without the use of any additional anchoring reagent (Figure 22d-e). However, the signal intensity was significantly lower compared to BG-TMR-MA (Figure 22f). Once again, this can be attributed to the absence of the MA group in SNAP-Cell TMR-Star.

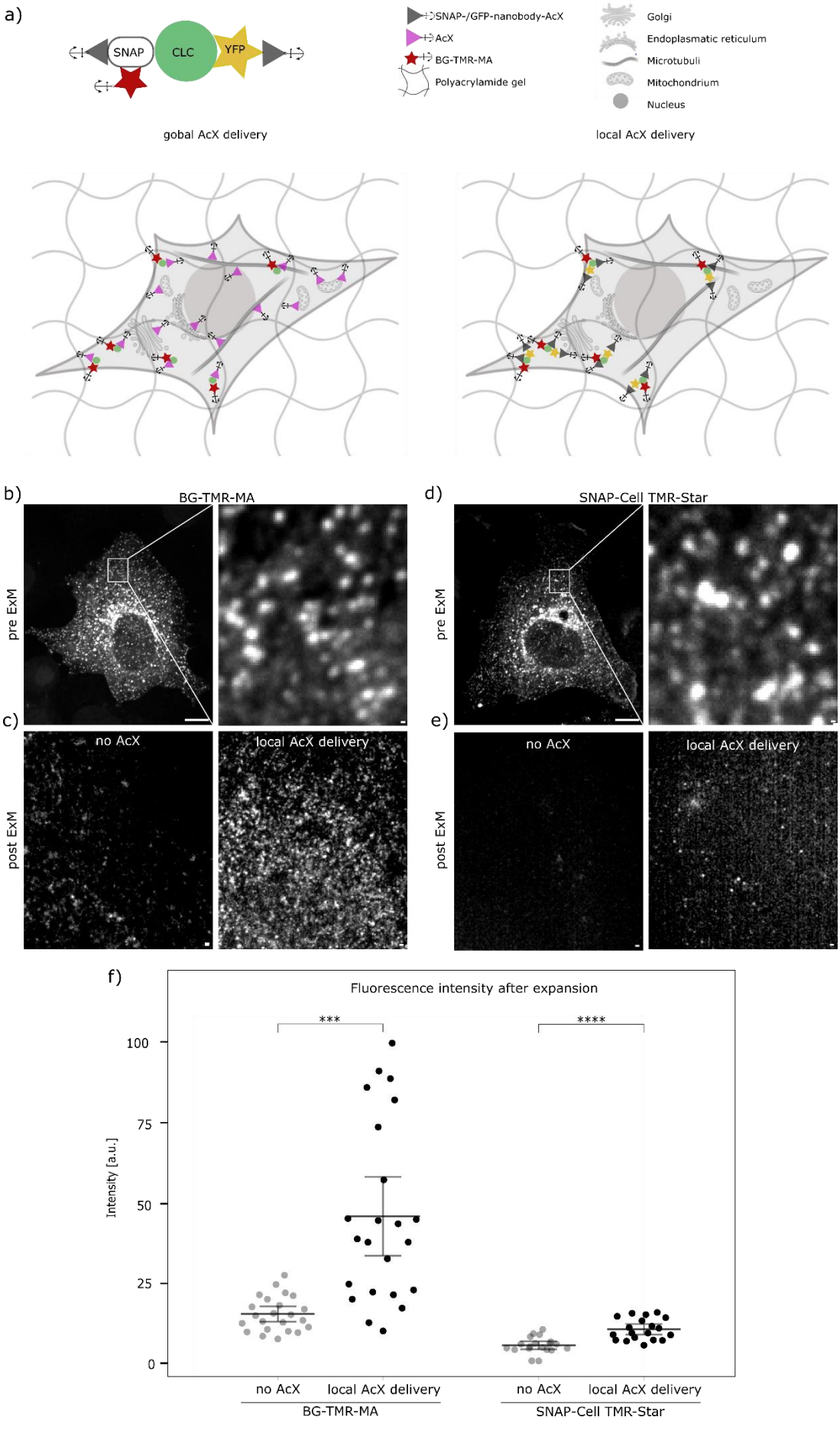
a)
SNAP
CLC
YFP
SNAP-/GFP-nanobody-AcX
AcX
BG-TMR-MA
Polyacrylamide gel
Golgi
Endoplasmatic reticulum
Microtubuli
Mitochondrium
Nucleus
gobal AcX delivery
local AcX delivery
b)
BG-TMR-MA
pre ExM
c)
no AcX
local AcX delivery
post ExM
d)
SNAP-Cell TMR-Star
pre ExM
e)
no AcX
local AcX delivery
post ExM
f)
Fluorescence intensity after expansion
***
****
Intensity [a.u.]
100
75
50
25
0
no AcX
local AcX delivery
BG-TMR-MA
no AcX
local AcX delivery
SNAP-Cell TMR-Star

Figure 22: Local delivery of AcX via AcX-coupled nanobodies rescues BG-TMR-MA signal.

a) Schematic representation of SNAP-CLC-YFP construct with BG-TMR-MA and AcX-coupled SNAP- and GFP-nanobodies binding to the SNAP- and YFP-tagged target protein, respectively. Comparison of monomer availability in the case of global AcX delivery versus local AcX delivery. In the first case AcX provides cellular structures randomly with polymerizable units, whereas in the latter polymerizable acrylate moieties are only delivered to the target protein, here clathrin. b) Fluorescence micrograph of a SNAP-CLC-YFP expressing cell stained with BG-TMR-MA before expansion. On the right zoom-in of boxed region. c) Post-ExM zoom-in images of SNAP-CLC-YFP expressing cells stained with BG-TMR-MA. ExM was performed without AcX or with local AcX delivery via AcX-coupled nanobodies. (left) BG-TMR-MA staining of SNAP-CLC-YFP without any AcX. (right) BG-TMR-MA staining of SNAP-CLC-YFP in presence of AcX-coupled anti-SNAP nanobodies and AcX-coupled anti-GFP nanobodies (anti-GFP nanobody binds to YFP). d) Fluorescence micrograph of a SNAP-CLC-YFP expressing cell stained with SNAP-Cell TMR-Star before expansion. On the right zoom-in of boxed region. e) Post-ExM zoom-in images of SNAP-CLC-YFP expressing cells stained with SNAP-Cell TMR-Star. ExM was performed without AcX or with local AcX delivery via AcX-coupled nanobodies. (left) SNAP-Cell TMR-Star staining of SNAP-CLC-YFP without any AcX. (right) SNAP-Cell TMR-Star staining of SNAP-CLC-YFP in presence of AcX-coupled anti-SNAP nanobodies and AcX-coupled anti-GFP nanobodies. Scale bars are 10 µm (b, d), 200 nm (zoom-in b, zoom-in d) and 200 nm (c, e). d) Quantification of fluorescence intensity of cells stained with BG-TMR-MA and SNAP-Cell TMR-Star after expansion. Cells (*n*=23 for BG-TMR-MA stained cells and *n*=19 for SNAP-Cell TMR-Star stained cells) with local delivery of AcX via AcX-coupled nanobodies and without any AcX are compared. Error bars represent standard error of the mean (SEM). Tested for significance using Mann-Whitney test and unpaired T-Test under the assumption of unequal variances.

On the contrary, directed delivery of AcX to another cellular target, for example microtubules, resulted in missing signal of BG-TMR-MA stained nuclear pores (Figure 23a). For this negative control, the stable NUP96-SNAP cell line was used to ensure that a negative signal resulted from a lack of anchorage because the AcX-labeled nanobodies were too far away from the label, rather than from a cell that was simply not transfected. Therefore, anti-tubulin antibodies were coupled to AcX and used to crosslink microtubules into the gel. Secondary anti-mouse Abberior Star Red antibodies were used for visualization. In this way, only microtubules were anchored, but not nuclear pores. As expected, the signal for the nuclear pores was lost after expansion but not for the locally anchored microtubules (Figure 23a). For comparability, NUP96-SNAP cells were stained using the same staining and fixation protocol as in previous nuclear pore experiments. However, it is worth noting that the protocol includes two permeabilization steps that are not optimal for microtubule preservation, resulting in a discontinuous signal.

Otherwise, if AcX-coupled SNAP-nanobodies were directed against nuclear pores, a signal for BG-TMR-MA stained nuclear pores was detected (Figure 23b). It follows that the

delivery of AcX via nanobodies is specifically directed towards the target protein, resulting in signal enhancement for that particular structure.

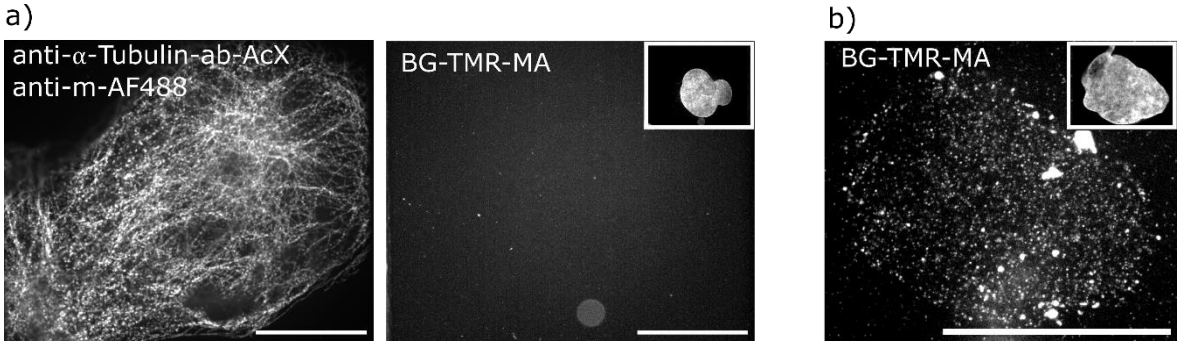

Figure 23: Directed delivery of AcX is specific for the target protein and results in a signal enhancement for this very structure.

a) Directed AcX delivery to microtubules via AcX-coupled anti-alpha-tubulin antibodies resulted in missing signal for BG-TMR-MA stained NUP96-SNAP cell but retained signal for microtubules after expansion. (left) Microtubules were anchored and stained simultaneously via AcX-coupled primary anti-alpha-tubulin antibodies and detected via secondary anti-mouse-AF488 antibodies. (right) Post ExM image of BG-TMR-MA stained nuclear pores of the same cell. b) BG-TMR-MA stained nuclear pores after expansion under presence of AcX-coupled anti-SNAP-nanobodies. Image (b) acquired by Maria-Anna Kirmpaki. Insets show DAPI staining. Scale bars are 10 µm.

2.1.5 AcX concentration has an effect on expansion factor

As explained in 1.3.4 the polyacrylamide gel is made of different components and the monomer-equipped labels copolymerize into the hydrogel for efficient signal retention. The rate of expansion of the gel is dependent on various factors, including the degree of crosslinking of certain regions in the gel. I found that the use of high AcX concentrations unfortunately affected the expansion factor. The higher the AcX concentration, the lower the expansion factor was. This is most likely due to a greatly increased number of AcX-monomers in the cell, which are crosslinked into the polyacrylamide gel throughout the cell, increasing the crosslinking density and the strength of the swollen gel and thus making it less extensible (Zohuriaan-Mehr and Kabiri, 2008). Two approaches were used to calculate the expansion factor: Firstly, the diameter of the NPC was measured after expansion and divided by the literature value for the diameter of nuclear pores, which is 107 nm (Winey *et al.*, 1997). Secondly, the area of the nucleus was measured and divided by the mean nuclear area before expansion. Both methods yielded comparable results for the expansion factor in the presence of 0.1 mg/mL and 1 mg/mL AcX, with expansion

factors of 3 and 3.6 for 0.1 mg/mL, and expansion factors of 2.5 and 2.3 for 1 mg/mL AcX (Figure 24). At a low AcX concentration of 0.01 mg/mL, measurement of the NPC diameter was more difficult because of the weak signal. Therefore, determining the nuclear area to calculate the expansion factor is more reliable here and revealed an expansion factor of 4.3 for 0.01 mg/mL AcX (Figure 24c-d). However, when AcX-coupled nanobodies were used, an average expansion factor of 4.16 ± 0.12 was calculated by using computational distortion analysis (see 2.1.6). It follows that by using AcX-coupled nanobodies, the expansion factor could be rescued. Compared to the global use of high concentrations of AcX, the coupling of AcX with nanobodies resulted in a localized increase in monomer density. This increase did not hinder the overall swelling abilities of the gel but did enhance the copolymerization of labeled fragments at the target site.

a)

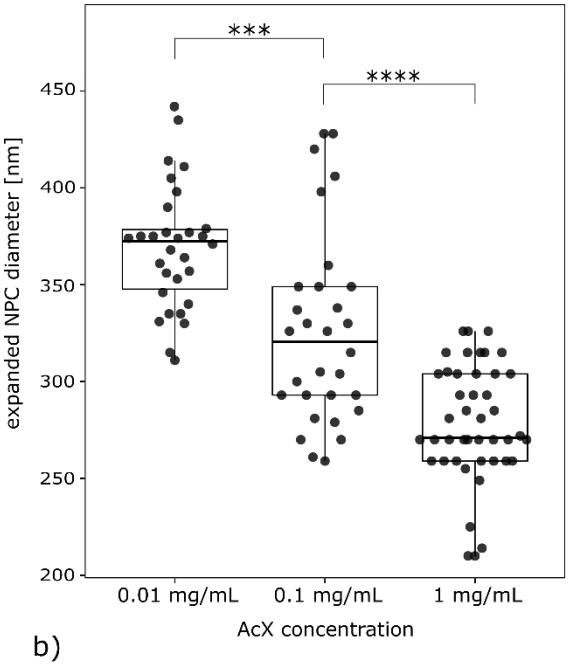

b)

AcX conc.	0.01 mg/mL	0.1 mg/mL	1 mg/mL
EF	3.5	3.0	2.5

c)

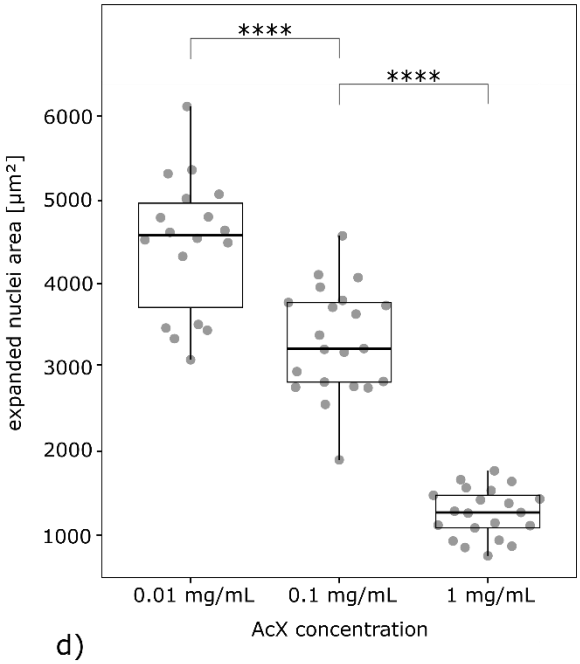

d)

AcX conc.	0.01 mg/mL	0.1 mg/mL	1 mg/mL
EF	4.3	3.6	2.3

Figure 24: Expanded diameter of nuclear pores and expanded nuclei area in dependence of AcX concentration.

a) The expanded nuclear pore diameter was measured for 0.01 mg/mL, 0.1 mg/mL or 1 mg/mL AcX. b) Calculation of expansion factors (EFs) based on NPC diameter for 0.01 mg/mL, 0.1 mg/mL or 1 mg/mL AcX. The median NPC diameter was divided by 107 nm (Winey *et al.*, 1997) to calculate the expansion factor. c) The expanded nuclei area was measured for 0.01 mg/mL, 0.1 mg/mL or 1 mg/mL AcX. d) Calculation of EFs based on nuclei area. The nuclei area for each condition was divided by the mean nuclear area before expansion, which was found to be 252.6 µm^2. Tested for

significance using an unpaired T-Test under the assumption of unequal variances. Shown is the median and the boxes represent the upper and lower quartile.

2.1.6 Distortion analysis to evaluate isotropy of local AcX delivery

Nevertheless, increased monomer density at certain parts in the cell could potentially lead to a denser polymer network at these locations leading to an inhomogeneous structure, which could affect the isotropy of the expansion. In order to test this, I performed a distortion analysis using the python script provided in Truckenbrodt *et al.*, 2019. To do so, I expressed the SNAP-CLC-YFP fusion protein in cells and stained via BG-TMR-MA in presence of AcX-coupled anti-SNAP and anti-GFP nanobodies. Additionally, microtubules were stained via primary anti-alpha and anti-beta-tubulin antibodies and detected with secondary anti-mouse Abberior Star Red antibodies. Although the microtubules were not directly anchored, they still emitted a fluorescent signal after expansion. This is most likely due to their high abundance within the cell in terms of protein levels. Furthermore, microtubules serve as tracks for the transportation of clathrin-coated pits (CCPs) and interact with each other, as shown by the control of microtubule acetylation by CCPs (Montagnac *et al.*, 2013). Therefore, it is possible that microtubules were indirectly anchored by their proximity to AcX-anchored CCPs. Additionally, the sample was extensively labeled with two primary antibodies targeting alpha- and beta-tubulin, and the signal was amplified using a fluorescently labeled secondary antibody that binds to multiple primary antibodies. Because the microtubule signal was crucial for the distortion analysis, the fixation method was adjusted to optimize it. As such, methanol denaturation was used instead of paraformaldehyde (PFA) fixation. However, as expected, the signal intensity was lower and more discontinuous than in expanded microtubules imaged after anchoring with AcX-coupled anti-tubulin antibodies or AcX alone.

The same cells were imaged before and after expansion (Figure 25a-c) and analyzed using the python script (Truckenbrodt *et al.*, 2019) mentioned above, which rotates and scales the pre and post ExM images in order to overlay them as best as possible. Through sequential pre- and post-ExM imaging of the same regions, I was able to demonstrate the resolution improvement achieved with the local AcX delivery approach. CCPs, which are approximately 100 nm in size (Heuser and Evans, 1980), appeared as indistinct spots before

expansion (Figure 25d). However, they clearly benefited from the improved resolution after expansion with AcX-coupled nanobodies (Figure 25e). The root mean square (RMS) error was calculated by subtracting the deformation vectors before and after ExM from each other. Because of their well-defined structure, microtubules and not clathrin were used here to calculate the deformation vectors and analyze the degree of distortion (Figure 25f). The deformation vector map derived from the python script gave additional hints for regions most prone to anisotropic expansion (Figure S 7). Overall distribution of distortion vectors was visualized via a polar plot (Figure 25h). When comparing the angular distribution of vectors to the region of interest, it became clear that the amount of distortion did not correlate with regions predominantly anchored with AcX-coupled nanobodies. If AcX-coupled nanobodies were to cause additional distortion, it would likely be more prevalent in the regions where they bind to their target. In this case, those regions are where clathrin is detected (Figure 25g). Consequently, more distortion between 90° and 135° would be expected in this example (Figure 25g), but this is not the case, as shown in Figure 25h.

Overall, the findings indicate that delivering AcX locally through AcX-coupled nanobodies does not cause any additional distortion during the expansion process, particularly in areas where the local monomer density is higher. While the signal retention is locally improved, it seems to have a minimal effect on local hydrogel matrix changes.

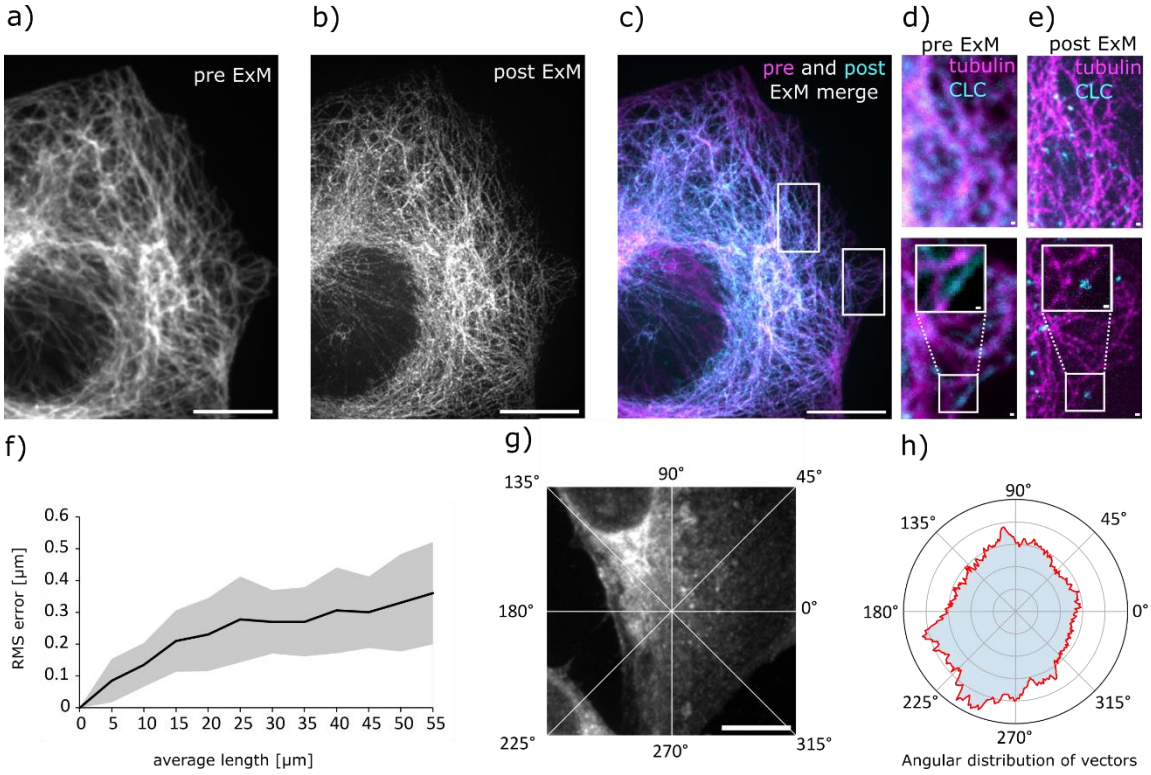

Figure 25: Local delivery of AcX does not cause additional distortion during the expansion process.

a) Fluorescence micrograph showing microtubule staining before expansion. Immunostaining against microtubules with primary anti-alpha- and anti-beta-tubulin antibodies, which were detected with a secondary anti-mouse Abberior Star Red antibody. b) Fluorescence micrograph showing the same cell as in a) after expansion. c) Overlay of pre ExM image a) in magenta and post ExM image b) in cyan. d) Insets showing pre ExM images of boxed regions in c) stained for microtubules via primary anti-alpha- and anti-beta-tubulin antibodies and detected with secondary anti-mouse Abberior Star Red antibody (magenta). SNAP-CLC-YFP was stained with BG-TMR-MA (cyan). e) Same regions of interest as in d) but after expansion in presence of AcX-coupled anti-SNAP and AcX-coupled anti-GFP nanobodies. Boxed regions in d) and e) show zoom-in images to emphasize resolution improvement after expansion. f) RMS error as a function of the average measurement length to determine the degree of distortion for local AcX delivery experiments. (black line = mean, standard deviation = grey shaded area, *n*=3, 111 measurements. g) Fluorescence micrograph of BG-TMR-MA stained clathrin before expansion with overlaid angular distribution. Highest fluorescence intensity between 90°-135° reflects the region where most AcX-coupled nanobodies are expected to bind. h) Polar plot showing the distribution of deformation vectors corresponding to the post ExM image of g). Deformation vectors are randomly distributed and do not accumulate between 90°-135°. Scale bars are 10 µm for a)-c), g) and 200 nm for d)-e).

2.1.7 Controlled grafting model

The results indicate that monomers directly located at the target are crucial for efficient incorporation of labels into the hydrogel. However, it is not enough to use the trifunctional label alone to deliver individual monomers to the target as shown in Figure 16a (no AcX used). The explanation for this is to be found in polymer chemistry. The process called grafting describes the recruitment of growing polymer chains to a surface. Especially, the bonding of the polymer chain to the surface by the incorporation of surface-bound monomers, called "grafting through" (Figure 9c), explains the chemistry behind our findings. In the "grafting through" approach, copolymerization occurs through the incorporation of surface-bound and free monomers. Here, the density of surface-bound monomers plays an important role in the formation of surface-attached polymers (Datta and Genzer, 2016).

Therefore, the dim signal after using BG-TMR-MA alone without any AcX is due to the unlikelihood that a growing polymer chain, after the reaction has started in solution, encounters a sparsely dispersed MA monomer on the target surface, which presents the only available polymerizable unit (Figure 26a). However, increasing the monomer density on the target surface increases the probability of a contact with the polymer chain and therefore of incorporation into the polyacrylamide meshwork. The densification can now be achieved in different ways: on the one hand by using AcX additionally and, on the other hand, by increasing the local AcX concentration using AcX-coupled nanobodies. In principle, both approaches result in the same outcome: the increased embedding of the labels in the hydrogel and thus greater signal retention (Figure 26b). Another aspect is the proximity of surface-bound polymerizable units, which is decisive for the incorporation of preferably bound or free monomers into the polymer chain (Datta and Genzer, 2016). If they are very close to each other incorporation of surface-bound monomers is favored, whereas more free monomers are incorporated if the spatial distance between surface-bound monomers is greater (Figure 26c). This is also reflected in my experiments: when high AcX concentrations are used, the monomer density is higher than at low concentrations. As a result, at high AcX concentrations, more surface-bound monomers, including BG-TMR-MA, are copolymerized, resulting in higher signal intensity. Ultimately, this can lead to a state of almost complete polymerization at the surface, known as in-plane polymerization (Datta

and Genzer, 2016). In contrast, the use of low AcX concentrations leads to a less dense distribution of surface-bound monomers and thus to the formation of loops with alternating incorporation of dissolved and surface-bound monomers (Figure 26c).

The hypothesis on the importance of surface grafting for signal maintenance in ExM was confirmed by delivering AcX only in close proximity to BG-TMR-MA stained clathrin via AcX-coupled nanobodies. This approach ensured that only surface-bound monomers were enriched, thus proving that the latter are the major player in ExM signal retention.

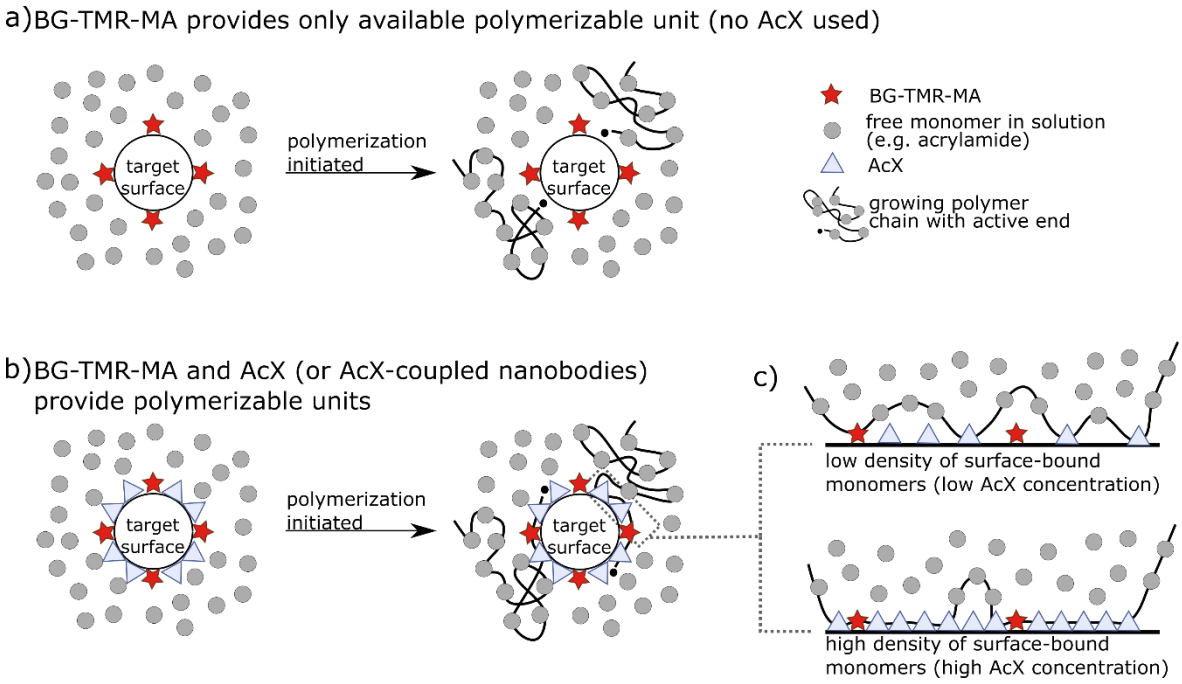

Figure 26: Model explaining the importance of surface grafting for signal retention in ExM.

a) If BG-TMR-MA is used as only anchoring moiety without any AcX, it provides the only available polymerizable unit. Therefore, the density of surface-bound monomers is very low and so are the chances that an active polymer chain will encounter a BG-TMR-MA monomer on the target surface and incorporate it into the growing chain. b) If BG-TMR-MA and AcX (or AcX-coupled nanobodies) are used together, they provide a higher density of surface-bound monomers compared to a). Thus, it is more likely that an active polymer chain will incorporate a surface-bound monomer, including BG-TMR-MA, and incorporate it into the growing chain. c) Based on b) two scenarios are possible: If the density of surface-bound monomers is low, the formation of loops is favored and alternating surface-bound and solute monomers will be incorporated into the polymer chain. If the density of surface-bound monomers is high, the incorporation of surface-bound monomers is favored over the incorporation of free monomers, leading to an almost in-plane polymerization.

2.1.8 Discussion

Since the development of ExM the retention of the fluorescence signal after the biological sample has been incorporated into a polyacrylamide gel, digested and expanded has been an essential issue of investigation. Due to the treatment needed for successful expansion of the specimen to occur, the signal afterwards is greatly reduced. To obtain a signal following the expansion procedure, the label or labeled structure of interest must be equipped with a polymerizable group that is incorporated into the polymer network ensuring signal preservation. Therefore, several strategies have been developed to address this issue. One is to directly equip the label with the polymerizable group. Here, this work has made significant advances. The project was originally focused solely on developing a novel trifunctional dye for ExM. This dye was thought to be beneficial because of its trifunctional nature, combining three important features in one small molecule: labeling, target delivery via covalent binding and anchoring. Thus, the idea was that a monomer moiety as part of the dye would be enough for sufficient anchorage. Indeed, it turned out that it was not. This eventually took the project in a different direction, allowing a closer look at the mechanism of signal retention in ExM.

BG-TMR-MA was synthesized by our collaborators in the organic chemistry department. I characterized its properties in terms of staining cellular targets and its robustness to the chemicals applied during the expansion procedure. I found that BG-TMR-MA exhibited great staining capabilities in our preferred cell line that stably expressed SNAP-tagged nuclear pores. The fluorescence intensity was higher compared to four different SNAP dyes tested, and the staining was highly specific among different biological target structures. Additionally, BG-TMR-MA is a cell-permeable dye and could also be used to label living cells. Furthermore, BG-TMR-MA demonstrated robustness against the chemicals used for the hydrogel formation. In conclusion, the trifunctional dye was the perfect candidate for ExM and for the future development of this project. However, the trifunctional dye's MA group, initially considered a substitute for the anchoring reagent, turned out to be insufficient to meet the requirement for a very bright fluorescent signal after expansion. To further investigate this observation, the anchoring reagent AcX was added globally to the sample at three different concentrations after staining with BG-TMR-MA, BG-TMR-Boc and SNAP-Cell TMR-Star. In order to gain a more detailed insight into the mechanism during the

individual steps of the expansion process, the samples were imaged after the respective steps, namely staining, gelation, digestion and expansion. This revealed that up to gelation the signal remained the same in all samples with different AcX concentrations. Notably, significant differences between the tested dyes and between the different AcX concentrations were observed after digestion and continued after expansion. This confirms that from the time of digestion, the anchoring plays a crucial role for the further signal intensity.

By adding AcX to the expansion procedure, I found that signal retention is increased with increasing concentrations of AcX. This can be explained by the fact that an increased amount of anchoring reagent results in more labeled proteins possessing a polymerizable group. This in turn means that more label is incorporated into the gel and therefore more signal is retained after expansion. Furthermore, as the concentration of AcX increased, BG-TMR-MA stained cells demonstrated higher signal retention compared to cells stained with the commercially available SNAP-Cell TMR-Star dye. The synthesis intermediate BG-TMR-Boc, as well as Snap-Cell TMR-Star, lack the MA group. As a consequence, the signal intensity of BG-TMR-Boc and SNAP-Cell TMR-Star is considerably lower after expansion than that of BG-TMR-MA. This observation was made using AcX concentrations that were gradually increased and without the use of any additional anchoring reagent. Consequently, it can be concluded that the MA group of BG-TMR-MA is functional and significantly contributes to the incorporation of more labels into the gel. However, using solely BG-TMR-MA without any additional polymerizable groups is not sufficient to achieve a satisfactory signal intensity.

This led to the hypothesis that monomer density at the target structure plays an important role in signal maintenance. This was demonstrated by delivering AcX via AcX-coupled nanobodies in close proximity to the target. To maximize the amount of monomers delivered to the target, a double-tagged target, SNAP-CLC-YFP, was chosen and expressed in cells. In this manner, AcX could be coupled to both anti-SNAP and anti-GFP nanobodies. Furthermore, nanobodies were preferred over antibodies due to their smaller size, allowing for more precise delivery of polymerizable groups to the target protein. Together with BG-TMR-MA this approach rescued the fluorescence signal and proved the model about the importance of surface grafting in ExM. An increased amount of polymerizable

groups on the target surface and next to the label increases the probability of the label being incorporated in the growing polymer chain and thus being retained.

When using high concentrations of AcX at 1 mg/mL applied globally to the sample, which is an order of magnitude higher than what is typically used in proExM (Tillberg *et al.*, 2016), a reduced expansion factor was observed. This is most likely due to increased crosslinking and resulting gel stiffness, which counteracts the expansion (Zohuriaan-Mehr and Kabiri, 2008). Although the local delivery of AcX rescued the expansion factor, minor disadvantages are that using AcX-coupled nanobodies is much more time consuming than using high AcX concentrations. First, a SNAP-labeled substrate must be expressed with an additional label, such as GFP, to increase the number of binding sites and the binding probability of AcX-coupled nanobodies. Even if the double-tagged construct is designed, the target protein may not be abundant enough, so anchoring via AcX-coupled nanobodies may not be sufficient for a good signal retention. In this case, higher AcX concentrations must ultimately be used. Possibly, a combination of a medium concentration of global AcX and a directed local AcX delivery would also be possible to avoid reduction of the expansion factor.

Nevertheless, it should be noted that local AcX delivery via AcX-coupled nanobodies does not cause any additional distortion of the expansion process, compared to conventional ExM. It was particularly interesting to investigate whether there is increased distortion in areas where nanobodies coupled with AcX specifically bind, namely in the region of interest (ROI). However, a distortion analysis revealed that this is not the case. These findings imply that the overall polyacrylamide gel structure remains unaffected by the presence of discrete AcX-coupled nanobodies, which may have led to partial stiffening of the gel and increased distortion. Due to the feasibility of length measurement for distortion analysis, nanoscale distortions were not considered and analysis was conducted in the micromolar range. The problem is that confocal pre ExM images are diffraction limited, whereas post ExM images are not. As a result, nanoscale distortions cannot be identified. This could be improved by comparing the super-resolution post ExM image with a super-resolution pre ExM image previously acquired using a different super-resolution imaging technique.

However, the experiments highlight the importance of surface grafting for dye retention in ExM. This mechanism is only one part of the whole expansion process, but it has not been

studied in detail yet. Therefore, understanding this mechanism may help in future troubleshooting, especially if there is a severe loss of signal after expansion. The amount of surface-bound monomers on the target surface and the proximity of these monomers to the label are critical for successful grafting and incorporation of the dye into the polymer network.

Outlook

For future improvement of the dye its integration into the polyacrylamide network is of special interest and could be improved further. One way to increase the likelihood that the polymerizable group of BG-TMR-MA will encounter a growing polymer chain in solution would be to increase the length of the linker between the dye and the MA group. To the best of my knowledge there is no information about best spatial distances between labels and monomers for optimal integration into the polymer network. It could be that increasing the linker length between the TMR core and the MA group, e.g. by Polyethylene glycol (PEG), would be beneficial for incorporation of the dye. One reason for this is steric hindrance. A longer linker would increase the molecule's flexibility, resulting in less steric hindrance. Other methods of creating trifunctional dyes already use longer linkers, such as the TRITON technique, which uses PEG as a linker (Wen *et al.*, 2020). The optimized TRITON linker for actin imaging features a combination of PEG and triazine as a scaffold (Wen *et al.*, 2023).

To enhance the grafting process, increasing the global concentration of AcX even further could be a potential option. Nevertheless, this approach does not appear to be very promising due to the possible further reduction of the expansion factor and steric limitations. Wen *et al*. have reported that there is no further improvement in signal intensity beyond a concentration of 0.5 mg/mL AcX. (Wen *et al.*, 2023). Therefore, it is likely that a reasonable maximum concentration of 1 mg/mL was already used in this study.

A more promising approach may be to incorporate additional acryloyl units into BG-TMR-MA. Recently, Wen *et al.* showed that increasing the number of acryloyl units in a trivalent linker increases signal retention. Interestingly, the number of anchors appears to be limited, as the authors observed increased signal retention up to three polymerizable

monomers, but signal retention decreased at four units (Wen *et al.*, 2023). Again, a reason for this might be that steric hindrance close to the target surface occurs upon adding too many AcX molecules. This is in line with the finding from Henze *et al.* They show that increasing the amount of surface-bound monomers is likely to be self-limiting in terms of new polymer chain attachment to the surface. The authors immobilized methacrylate moieties on silica gel surfaces and observed that attachment of new chains is hindered when a thick polymer layer is already formed on the surface (Henze *et al.*, 2014).

Apart from optimizing the label, other factors can also be considered to enhance signal preservation, e.g. different polymerization reactions or gel systems can also play a role. By using tetra gels it has been shown that non-radical polymerization is beneficial for preserving the signal, in terms of less dye destruction (Gao *et al.*, 2021). Another approach focuses on protecting the dye from free radical-induced degradation by including a fourth group to the trifunctional dye, which absorbs the attack of the radical resulting in intramolecular stabilization (Wen *et al.*, 2022).

Furthermore, the trifunctional dye could be optimized by exchanging or adding single atoms in the atomic ring structure or varying the alkyl groups on the nitrogen. For example, fluorination of the bottom aryl ring of the rhodamine scaffold or exchanging the bridgehead atom may lead to the development of new, optimized ExM dyes. These considerations are part of the current collaboration with Prof. Dr. Rainer Haag's group and will be investigated in future studies.

All these developments could be of interest for further improvement of BG-TMR-MA in order to make it even brighter and especially more robust against the harsh polymerization and digestion step.

2.2 Development of tobacco mosaic virus as a ruler for ExM

Since the early days of ExM invention, a much-discussed topic has been the isotropy of the expansion process. Isotropic expansion is of utmost importance, because only a reproduction of the biological structure is visible after expansion. Therefore, it must be ensured that the size ratios of the larger facsimile correspond to those of the original structure. The gold standard for reliably assessing isotropy and calculating the expansion factor has been to compare images of the same region before and after ExM. However, this approach is extremely time consuming, it is low throughput and requires advanced sample handling skills. Additionally, this approach is only possible in the case of pre ExM labeling but not in post ExM labeling. As described in 1.3.2 there have been several approaches to determine the expansion factor and the distortion in different ways.

After all, there is still no simple tool to determine the distortion and the expansion factor quickly and easily at a certain position of interest and in 3D. This project aimed at developing of such a tool by using tobacco mosaic virus (TMV). TMV is a positive-sense-single-stranded RNA virus that infects tobacco plants and causes a mosaic-like pattern on infected leaves from which it got its name. Due to its rigid rod shape and its certain length of 300 nm (Hall Vol and Cecil Hall, 1958; Zaitlin and Palukaitis, 2000), it was considered an ideal candidate for the development of a new ruler for ExM. The idea was to simply add labeled TMV particles to the sample of interest, expand them, and image the expanded particles along with the sample (Figure 17a). An automated pipeline would have been used to calculate the post ExM TMV length distribution and from that the expansion factor and possible distortions for individual regions in the whole sample. However, TEM analysis showed that TMV particles do not have a completely uniform length, but rather are distributed between 50 and 1280 nm, with most of them being 300 nm (Figure 27b-d). They appear to form aggregates as there is an increased population of 600 nm and 900 nm long particles, likely consisting of two and three 300 nm particles stuck together.

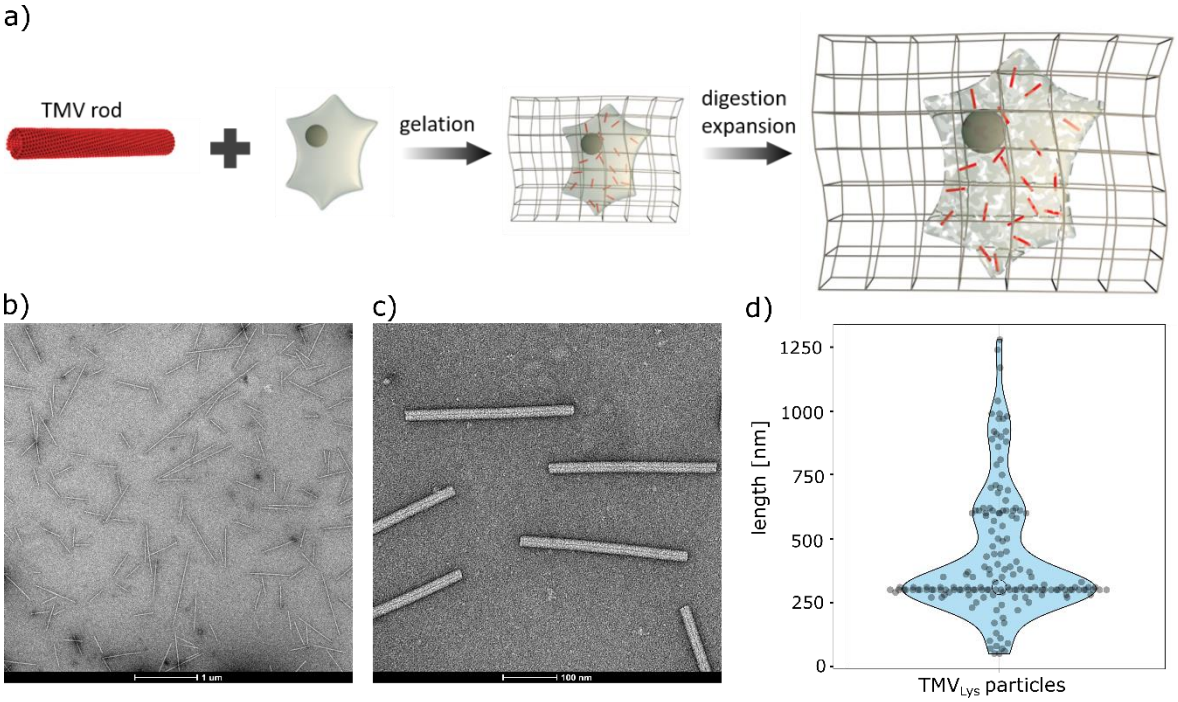

Figure 27: TMV rods as rulers for ExM.

a) Schematic showing the use of TMV rods as rulers for ExM. Labeled TMV rods are added to a sample of interest, e.g. a cell. The common ExM procedure is performed, including gelation, digestion and expansion. Afterwards, the expanded length of TMV particles is used to calculate the expansion factor and the distortion. b) TEM micrographs of TMV_{Lys} particles show a high distribution of particle lengths. c) TEM micrograph of TMV_{Lys} particles imaged at higher magnification. d) TMV_{Lys} nanorod length distribution. One quarter of all measured particles are 300 nm long (*n*=164). Scale bars are 1 µm (b) and 100 nm (c).

2.2.1 TMV labeling

To use TMV in fluorescence microscopy, it had to be labeled with a fluorophore. One TMV particle consists of 2130 coat proteins (CPs) arranged in a helical manner, which can be labeled theoretically. Geiger *et. al.* found that the fluorescent labeling of TMV_{wt} particles with Atto488-NHS ester did not succeed. After labeling, the authors performed SDS-PAGE and monitored fluorescence with a dark reader transilluminator. The respective CPs did not show a band for Atto488, indicating the importance of using engineered TMV particles for labeling (Geiger *et al.*, 2013). Therefore, an engineered version of TMV was used from Prof. Dr. Christina Wege´s laboratory in Stuttgart. They engineered TMV CPs to expose a higher number of lysine and/or thiol residues, making them more accessible for labeling. They gifted us the engineered variant TMV_{Lys}, which is equipped with an additional amino function on each CP subunit. To make the particles fluorescently visible before expansion,

they were labeled with varying amounts of the STED dye Abberior Star Red NHS and imaged on poly-L-lysine coated coverslips using a STED microscope (Figure 28). Regarding the labeling ratio, it was found that the best signal was obtained at a molar excess of about 4000 (Figure 28a). Lower amounts of dye resulted in weaker signals (Figure 28b-c) and at the same time higher amounts did not give a brighter signal. Also, when higher amounts were used, a solubility problem occurred and the dye precipitated.

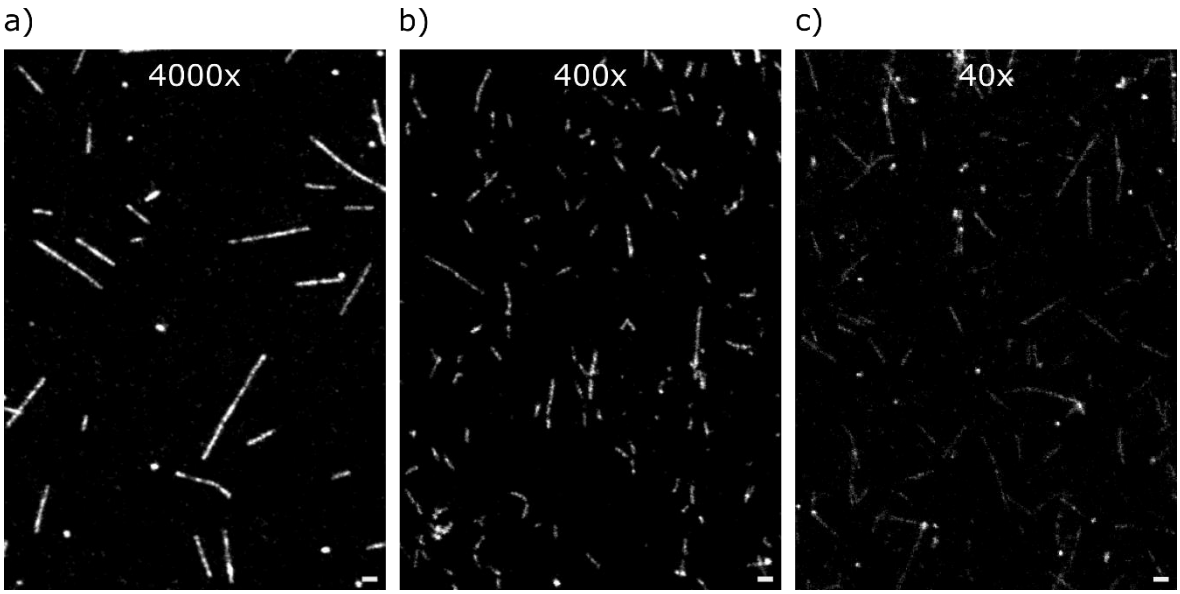

Figure 28: STED imaging of TMV_{Lys} particles labeled with Abberior Star Red.

a) TMV_{Lys} particles labeled with 4000x molar excess of Abberior Star Red NHS. b) TMV_{Lys} particles labeled with 400x molar excess of Abberior Star Red NHS. c) TMV_{Lys} particles labeled with 40x molar excess of Abberior Star Red NHS. Scale bars are 300 nm.

2.2.2 TMV cell entry

After successfully labeling TMV_{Lys} particles with Abberior Star Red NHS, hereafter referred to as $TMV_{StarRed}$, I added them to HeLa cells after fixation. Surprisingly, they did not enter the cells nor adhere to the cell membrane (Figure 29a-c). Even a harsh permeabilization step with 0.4% Triton-X-100 after methanol or 4% paraformaldehyde (PFA) fixation could not solve the problem. After observing that the issue was more evident with $TMV_{StarRed}$, especially after permeabilization in contrast to $TMV_{Atto488}$ (provided by Prof. Dr. Christina Wege), it seems that the dye itself plays a critical role. However, since Abberior Star Red is a remarkable STED dye, I did not modify the dye in this case. Instead, I aimed to deliver $TMV_{StarRed}$ directly and effectively into the cell by targeting tubulin via the interaction

between streptavidin and biotin. Therefore, $TMV_{StarRed}$ and primary anti-beta-tubulin antibodies were coupled to biotin, which subsequently bound to each other through streptavidin (Figure 29d-e). In this way, streptavidin acts as a linker platform connecting microtubules and TMV particles. The biotinylation of $TMV_{StarRed}$ and anti-beta-tubulin antibodies was confirmed by streptavidin-atto565 staining, respectively (Figure S 8). Moreover, 3D STED imaging demonstrated the deep penetration of $TMV_{StarRed-Biotin}$ into the cell (Figure 29f) and it further revealed the arrangement of $TMV_{StarRed-Biotin}$ particles along microtubules (Figure 29g). In order to efficiently target TMV to microtubules, while obtaining the maximum possible signal, the labeling had to be optimized because biotin-NHS and Abberior Star Red NHS both compete for the same binding sites. Molar excesses in the range of 400-4000x for Abberior Star Red NHS and 40-400x for biotin-NHS were tested and a molar excess of 2000x for Abberior Star Red NHS together with a molar excess of 40x for biotin-NHS was determined to be the best combination to simultaneously obtain efficient incorporation of TMV and a bright fluorescent signal. Additionally, also anti-alpha-tubulin antibodies were labeled with biotin and used simultaneously together with biotinylated anti-beta-tubulin antibodies to enhance the binding of $TMV_{StarRed-Biotin}$ to microtubules.

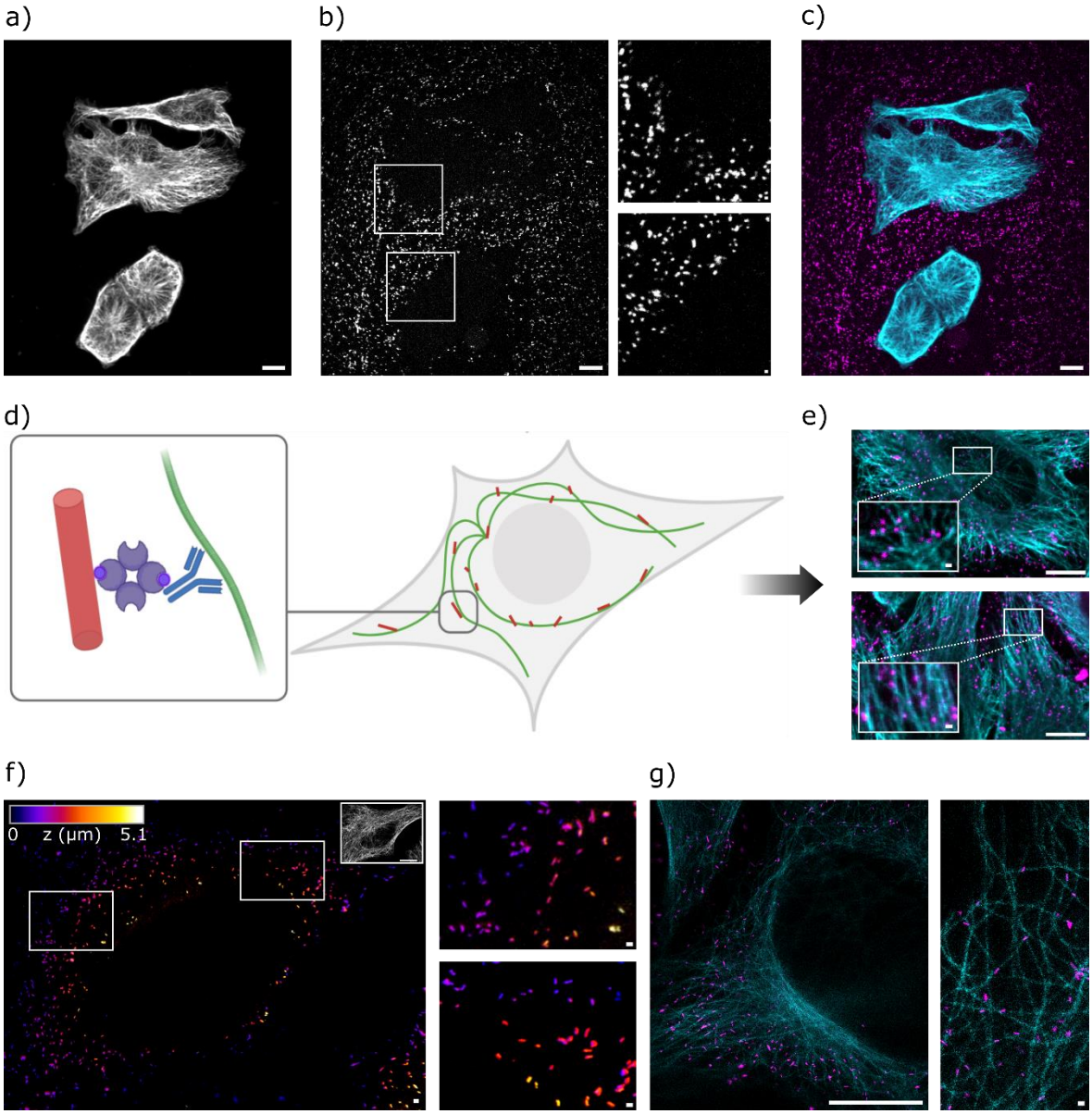

Figure 29: Facilitated TMV cell entry by tubulin targeting via streptavidin-biotin interaction.

a) Fluorescence micrograph of microtubules stained via primary anti-alpha-tubulin and anti-beta-tubulin antibodies, detected with a secondary anti-mouse Alexa Fluor488 antibody. b) $TMV_{StarRed}$ particles binding to cover glass but not to cells. Same region of interest as in a). Zoom-ins of boxed regions (b) demonstrate that TMV particles do not enter cells. Clear separation between $TMV_{StarRed}$ particles and the regions where cells are located. c) merge image of a) and b) showing no overlap of $TMV_{StarRed}$ particles and cells. d) Schematic representation of facilitated TMV cell entry. $TMV_{StarRed}$ particles and anti-tubulin antibodies are coupled to biotin (blue bullets). After microtubules are recognized by biotinylated anti-tubulin antibodies, streptavidin (dark blue homotetramer) acts as a linker and connects biotinylated tubulin antibodies and biotinylated $TMV_{StarRed}$ particles, thereby pulling TMV particles into the cell. e) Fluorescence micrographs demonstrating TMV cell entry using biotin-streptavidin-biotin as a linker platform. Microtubules were stained via biotinylated anti-beta-tubulin primary antibodies and detected with a secondary anti-mouse AF488 antibody (cyan). $TMV_{StarRed\text{-}Biotin}$ (magenta) binding to biotinylated tubulin antibodies via streptavidin. f) 3D STED imaging of $TMV_{StarRed\text{-}Biotin}$ with depth encoded z-stacks. The color represents the z-depth. For a better orientation, 3D STED imaging of microtubules of the same cell is shown in the zoomed-in

inserts. Microtubules were stained with biotinylated primary anti-alpha-tubulin and anti-beta-tubulin antibodies and detected with secondary anti-mouse Abberior Star580 antibodies. Zoom-ins of boxed regions highlight deep penetration of $TMV_{StarRed-Biotin}$ into the cell. g) 2D dual color STED imaging of microtubules and $TMV_{StarRed-Biotin}$. Microtubules were stained with biotinylated primary anti-alpha-tubulin and anti-beta-tubulin antibodies and detected with secondary anti-mouse Abberior Star580 antibodies. On the right zoom-in image of a different cell emphasizing the orientation of $TMV_{StarRed-Biotin}$ particles along the microtubules. Scale bars are 10 µm in main images (a, b, c, e, g), 600 nm in zoom-ins (b, e), 600 nm in f) and 300 nm in zoom-ins (f, g).

2.2.3 ExM of TMV

After successfully establishing the first two steps of developing TMV as a ruler for ExM, namely labeling TMV particles and introducing them into cells, the next goal was to perform ExM with TMV particles. Therefore, ExM was performed with $TMV_{StarRed}$ particles alone on poly-L-lysine coated coverslips and with $TMV_{StarRed-Biotin}$ particles in HeLa cells in combination with biotinylated anti-alpha- and anti-beta-tubulin antibodies. Unfortunately, the TMV rods could not be visualized as continuous tubular structures anymore after expansion (Figure 30).

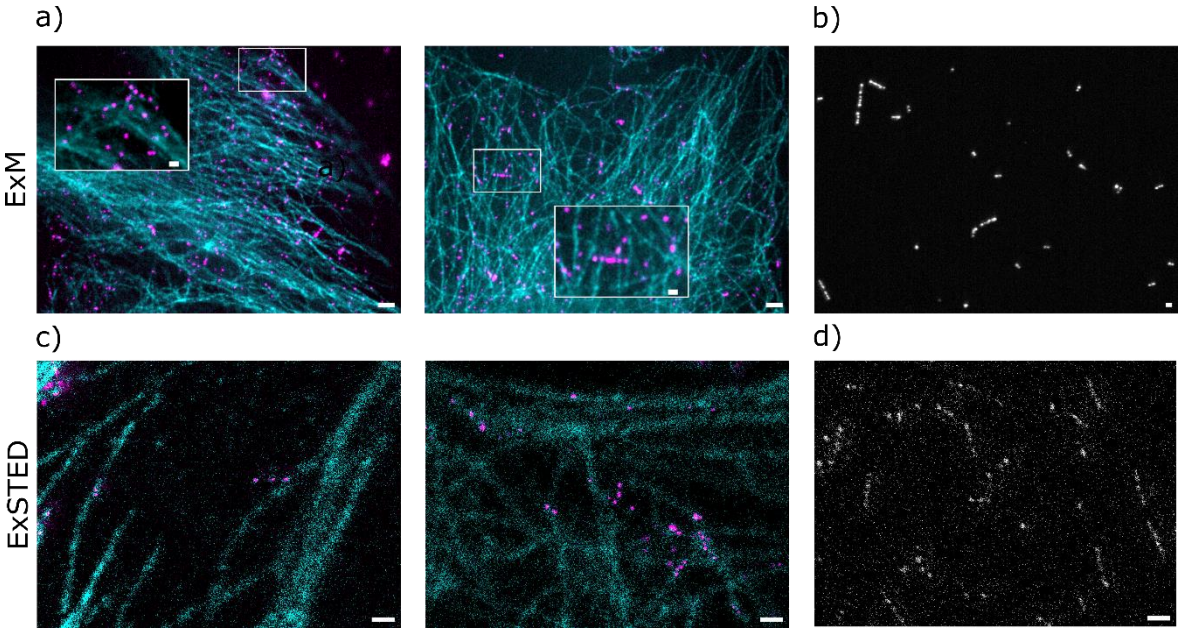

Figure 30: ExM of labeled TMV nanorods.

a) ExM of $TMV_{StarRed-Biotin}$ in HeLa cells. Microtubules were stained with biotinylated primary anti-alpha- and anti-beta-tubulin antibodies and detected with a secondary anti-mouse Abberior Star580 antibody. Zoom-in images of boxed regions. b) Fluorescence micrograph of expanded $TMV_{Atto488}$ particles on cover glass. c) STED imaging of expanded $TMV_{StarRed-Biotin}$ in HeLa cells. Laser scanning confocal imaging of expanded microtubules, stained with biotinylated primary anti-alpha- and anti-beta-tubulin antibodies and detected with a secondary anti-mouse Abberior Star 580

antibody. d) STED imaging of expanded $TMV_{StarRed\text{-}Biotin}$ particles on cover glass. Scale bars are 1 µm (a) and 300 nm (zoom-ins (a), b-d).

However, it is crucial that TMV rods are continuously labeled to ensure correct length measurement of the particles after expansion. Possible reasons for the discontinuous and weak signal could be that proteinase K cut off too many labels during the digestion process or that the TMV particles were not sufficiently anchored. Therefore, several approaches were developed to analyze the problem and to optimize the signal. These were based on the following points: labeling, anchoring, gel composition and digestion and are summarized in Table 1.

It was hypothesized that decreasing the density of fluorophores on the particles could enhance the anchoring efficiency by freeing up more lysine residues for AcX to react with, resulting in improved anchoring. Although this slightly improved the signal continuity after expansion, it decreased the signal intensity. The experiment was reversed by extensively increasing the amount of dye to a molar excess of 10,000 to 20,000. The aim was to achieve the highest possible labeling density in order to ensure that sufficient dye remained after digestion. Unfortunately, this resulted in dye precipitation. To improve the dye solubility, various dyes were tested in addition to Abberior Star Red, which enabled higher labeling ratios. These included Abberior Star 580, Atto488 and especially Abberior Star 635P, which is known to have a higher water solubility due to its phosphorylation. Indeed, labeling with Abberior Star 635P showed less precipitation, so that higher labeling ratios were possible. Unfortunately, $TMV_{Star635P}$ particles were not brighter in pre ExM imaging compared to Abberior Star Red labeled particles. Since replacing the dye did not provide benefits, I aimed to enhance the labeling by methods other than NHS-ester labeling. Initially, I used primary anti-TMV antibodies together with secondary anti-mouse Abberior Star Red antibodies. Unfortunately, the TMV immunolabeling was too unspecific and showed a strong background signal, so it was not pursued further. Secondly, I labeled streptavidin with Abberior Star Red to deliver more dyes to $TMV_{StarRed\text{-}Biotin}$ particles. However, signal intensity and continuity were comparable to particles labeled only with Abberior Star Red or Atto488 (Figure S 9). Another aspect was the optimization of the labeling process itself. Of the two labeling buffers tested, the following labeling buffer proved to be the best: 30 mM Hepes, 300 mM NaCl, and 10% glycerol. Furthermore, two different versions of

TMV_{Lys} were tested for labeling. Additionally to the previously used version TMV_{Lys20}, TMV_{Lys19} (also a gift from Prof. Christina Wege) was tested. The difference between both variants is a nucleotide substitution at a different position in the CP open reading frame of a plasmid containing the TMV_{WT} cDNA (Geiger *et al.*, 2013). This eventually leads to the additional introduced lysine residue being exposed at a different site of the CP. However, none of the attempts to improve the labeling did significantly improve the fluorescence signal after expansion. Therefore, in the next step the anchoring was optimized and different anchoring reagents, including AcX, MA-NHS and GA were tested. On the one hand, both AcX and MA-NHS rely on NHS-ester chemistry, so MA-NHS did not improve the incorporation of TMV particles into the hydrogel. On the other hand, GA anchoring (Chozinski *et al.*, 2016) is based on a different mechanism, namely crosslinking and proved to be more suitable for anchoring TMV rods in ExM. After anchoring, the next step to investigate was gelation. The U-ExM gel recipe (Gambarotto *et al.*, 2019) which contains twice as much SA and four times as much AA was tested alongside the conventional monomer solution used in proExM (Tillberg *et al.*, 2016). However, this did not have any impact on preserving TMV particles in the polyacrylamide gel. Finally, I investigated the digestion process and attempted denaturation with SDS rather than gel digestion, as described in the U-ExM protocol (Gambarotto *et al.*, 2019). However, no improvement in signal continuity was observed here either. A slight improvement in the retention of the signal was obtained when higher dilutions of proteinase K were used (10-fold higher than usual, 0.8 U/mL) (Figure S 10). However, this is not suited as general procedure because it most likely leads to inhomogeneous expansion of the sample and more distortion.

Table 1: Summary of TMV constructs and approaches to optimize ExM of TMV particles.

Results of the approaches are divided into "improvement in signal intensity" and "improvement in signal continuity". Red crosses indicate no improvement and green ticks indicate (partial) improvements. Subscript numbers represent molar labeling ratios.

TMV-construct/approach	Aim of approach	Improvement in signal intensity	Improvement in signal continuity	Comments
$TMV_{StarRed1000x\text{-}Biotin4x}$	Reduce fluorophore density to improve anchoring	✗	(✓)	Not enough biotin, TMV did not enter cells anymore
$TMV_{StarRed10,000x\text{-}Biotin40x}$ $TMV_{StarRed20,000x\text{-}Biotin40x}$	Increase fluorophore density to get maximal brightness	✗	✗	Precipitation of dye
$TMV_{Star580\text{-}5000x\text{-}Biotin40x}$ $TMV_{Star580\text{-}10,000x\text{-}Biotin40x}$ $TMV_{Atto488\text{-}10,000x\text{-}Biotin40x}$	Test different dyes for labeling	✗	✗	
$TMV_{Star635P\text{-}5000x\text{-}Biotin40x}$ $TMV_{Star635P\text{-}10,000x\text{-}Biotin40x}$	Increase solubility and thus enable higher labeling ratios	✗	✗	
Anti-TMV primary antibodies and anti-mouse Abberior Star Red secondary antibodies	Indirect labeling	✗	✗	(Figure S 9)
Labeling of $TMV_{StarRed\text{-}Biotin}$ with $streptavidin_{StarRed}$	Indirect labeling	✗	✗	(Figure S 9)
30 mM Hepes, 300 mM NaCl, and 10% glycerol instead of $NaHCO_3$	Optimization of labeling buffers	✓	✗	

TMV_{Lys19} instead of TMV_{Lys20}	Find best suited TMV variant for labeling	x	x	
MA-NHS anchoring	Optimization of anchoring reagent	x	x	
GA anchoring	Optimization of anchoring reagent	x	✓	
U-ExM MS for gelation instead of proExM MS	Optimization of gel formulation	x	x	
SDS denaturation instead of proteinase K digestion	Digestion vs. denaturation	x	x	
10 times less proteinase K (1:1000 dilution, 0.8 U/mL)	Optimization of digestion	✓	✓	Less expansion because of higher diluted proteinase K (Figure S 10)

2.2.4 Discussion

Due to the artificial nature of the ExM process, which is based on the combination of a biological sample with a chemical polyacrylamide gel and the expansion of the latter, the isotropy of the expansion process has been a hotly debated issue since the beginning of its development. After digestion or denaturation of the original biological sample, only a facsimile remains and all subsequent conclusions are based upon it. Ensuring that expansion was isotropic is therefore extremely important for reliability of results. Recently, several approaches have been proposed to develop a tool for determining distortion, including the use of DNA-origamis, nanopillars, and the addition of a fluorescent grid (Scheible and Tinnefeld, 2018; Lee *et al.*, 2021; Nakamoto *et al.*, 2022; Damstra *et al.*, 2023). However, when this project started there was no easy to use tool to determine the distortion in the sample after performing ExM. In addition, the tools developed to date have limitations in the following areas: Nanopillars do not serve as a standard integrated into the cell since the surface topography is only imprinted on the hydrogel surface (Nakamoto *et al.*, 2022). Although GelMap applies intrinsic calibration and permits the correction of anisotropies introduced during ExM, it only reports deformations in the micromolar range and does not penetrate deep into the sample (Damstra *et al.*, 2023). Finally, DNA origamis have so far only been used in vitro as a calibration tool (Scheible and Tinnefeld, 2018; Lee *et al.*, 2021).

This results in the requirement for this tool to be an internal standard that permeates the sample. Distortion is usually evaluated only in the x-y plane, but it can also occur in the z-plane. Therefore, the ideal tool would be able to detect distortions occurring in the z-plane and allow for analysis of overall distortion in 3D. Additionally, it should have a specific length to facilitate calculation of differences between expanded regions. Moreover, the tool must be rigid due to the challenges associated with measuring the length of curved structures. Moreover, the application of the tool should be straightforward and easy to use.

TMV particles were considered to be the ideal candidate for this application owing to their rigid structure and well-defined length. As reported in the literature, TMV particles should have a length of 300 nm (Hall Vol and Cecil Hall, 1958). However, further research and my own analyses have shown that the particles are more likely to have a length distribution,

with the majority of them being around 300 nm. While they are generally 300 nm in length, there are also shorter fragmented rods or rods that attach to each other and then appear as a single long rod. One possible explanation for the presence of fragmented rods could be the impurity of the sample, transport, and long storage times. In addition, temperature and buffer composition, especially the amount of calcium and magnesium ions, during the purification of TMV particles have an effect on fragmented and aggregated rods (Hulett and Loring, 1965). With regard to long TMV aggregates, either end-to-end aggregated TMV particles/fragments (Lauffer, 1938, 1944) or the mutation of Lysine residues might play a role. For instance, it has been demonstrated for a TMV_{T42W} mutant that it has a tendency to form very long particles (Asurmendi *et al.*, 2007).

Although TEM experiments showed that the TMV length was not as uniform as expected, the TMV particles were still considered a useful ruler for ExM. This is because nanoscale distortions in specific regions of the sample could be determined by comparing STED imaging of TMV particles before ExM with confocal or STED imaging of the same particles after ExM. The expansion factor of a cell can be determined even if pre ExM imaging of the same cell is not available, due to the known length distribution of TMV particles. Nevertheless, this finding was a limitation to the applicability of TMV particles. Comparing the same cell before and after expansion and performing pre ExM STED imaging would significantly increase the effort. In contrast to the length, the diameter of the viruses remains constant at 18 nm, which is approximately 72 nm after expansion. However, to achieve the necessary resolution, ExSTED would be required instead of confocal ExM. Nevertheless, very precise measurements would be necessary.

TMV_{Lys} particles, which have a higher number of exposed lysine residues and are therefore optimized for labeling were used to label them with Abberior Star Red NHS. The far red dye is an excellent STED dye and STED imaging of $TMV_{StarRed}$ particles resulted in bright and super-resolved images of the TMV rod-like structure.

However, after successfully labeling the particles for STED imaging, they could not be delivered into cells and did not even adhere to the cell membrane. This problem was solved by targeting biotinylated TMV particles to biotinylated antibodies that bind to microtubules by linking them via streptavidin. 3D STED imaging showed that the labeled TMV particles penetrated deep into the cell.

Unfortunately, in the next step, TMV particles could not be subjected to ExM with satisfactory results. Neither on coverslips nor in cells could they be detected as a bright and continuous rod-like structure after expansion. Various attempts aiming at different parts of the experimental procedure, did not result in a sufficient improvement of the signal. Since many fluorophores are removed in the digestion process and the fluorophore density is diluted by the volumetric expansion automatically, a high labeling density is crucial for good signal retention after expansion. Therefore, initial attempts aimed at increasing the labeling density by increasing the molar excess of the dye during labeling and by testing different fluorescent dyes. Since TMV particles consist of more than 2000 CPs, labeled rods were expected to be very bright if all CPs were labeled. One explanation for the limited labeling density after expansion could be that not all CPs were accessible for labeling due to their dense packing and possible steric hindrance. However, dyes are very small, so another factor probably plays a role. Hydrophobic effects could also have an influence due to the extremely high local dye density on the TMV particles. Furthermore, it is possible that there are insufficient free lysine residues available for attachment to AcX. To address this issue, I decreased the labeling density to ensure an adequate number of free lysines, which can then be modified with a polymerizable group. However, this trade-off between labeling density and anchoring has not resulted in improved signal intensity and continuity. Because GA acts as a crosslinker and is not based on NHS ester reaction with free amines, GA anchoring gave slightly better results compared to AcX anchoring. Different monomer solutions and digestion procedures did not yield further improvements, except for reducing the amount of proteinase K. However, this reduction decreased the expansion factor and most likely affected the isotropy of the expansion process. Consequently, this approach was not pursued any further. Nevertheless, that was an indication that incomplete anchoring of the particles occurred.

Outlook

For the future development of TMV as a ruler for ExM there are two important points, which need to be addressed. First, in order to meet the requirement for a tool that is easy to use with minimum effort, the length of the TMV particles should be uniform. Therefore, size exclusion chromatography can be used to obtain a fraction containing particles 300 nm

in length. To gain a clearer understanding of when the signal is lost during the ExM process, it may be beneficial to perform imaging after the different stages of the ExM process. Secondly, further improvement of labeling and anchoring is needed to enhance signal retention after ExM.

To improve the labeling of TMV particles, one possibility is to employ multi-epitope labeling, as done by Bruckman and Steinmetz (Bruckman and Steinmetz, 2014). By labeling diverse sites on the surface of TMV, a higher dye density can be achieved. For instance, exterior tyrosine residue 139 could be labeled by functionalization with a terminal alkyne residue, which can be labeled by click chemistry with an azide-conjugated fluorescent dye (Bruckman and Steinmetz, 2014). Lysine and tyrosine residues can then be labeled simultaneously using Abberior Star Red NHS and Abberior Star Red azide, respectively. In addition to the labeling procedure, future studies can explore enhancing the embedding of viral particles in the hydrogel. Our previous findings have demonstrated that the local monomer density plays a critical role in successful grafting (Thielhorn *et al.*, 2023). Consequently, introducing an acrylate anchor to the TMV particles could potentially improve signal retention. A trifunctional dye with both an anchoring and a targeting moiety, specifically an NHS-group, could be utilized for this objective. Furthermore, Michalska *et al.*, 2023 demonstrated recently that modified streptavidin-acrylamide could anchor biotinylated WGA into gel matrices (Michalska *et al.*, 2023). This approach may also lead to improved crosslinking of biotinylated TMV particles.

3. Conclusion

The aim of this doctoral study was to create novel ExM tools, such as a trifunctional dye and an internal ruler, that would improve the application of the technique and provide mechanistic insight into the underlying chemical reactions that lead to successful dye retention.

In this study, I developed a novel trifunctional dye for ExM that combines three essential functionalities in one small molecule: targeting, gel anchoring, and labeling. I identified the key mechanism for efficient signal retention in ExM, which lies in the provision of a sufficient amount of surface-bound monomers at the target structure. Delivering monomers in close proximity to the target demonstrated the significance of the amount of surface-bound monomers and their proximity to the labeled target for their incorporation into the growing polymer network during polymerization of the hydrogel, and ultimately for successful signal retention after expansion. This analysis of the chemical mechanisms involved in the ExM process is of particular interest for the further development and improvement of this technique. In addition, understanding the mechanistic basis of signal retention for ExM highlights the importance of considering how the labeled dye is incorporated into the gel when using different gel compositions or polymerization reactions. Moreover, the covalent attachment and hydrogel incorporation of the < 1 kDa probe minimized the linkage error. Additionally, sub-diffraction imaging of nuclear pores was made possible with this small dye in a stoichiometric manner. Therefore, this study marks a significant step forward in quantitative single molecule microscopy alongside ExM, achieved by using stoichiometric labeling of SNAP-tagged proteins with single dyes and a method for their gel retention.

Furthermore, this study aimed at developing an internal ruler for ExM, facilitating the quantification of distortion introduced during the expansion process and the calculation of the expansion factor. For this purpose, TMV particles were chosen due to their rigid and rod-like structure. They were labeled successfully, delivered into cells, and imaged using STED microscopy. However, post ExM imaging produced unsatisfactory results. In addition, the particles displayed a distribution of lengths rather than a defined size. If these two issues can be resolved in the future, TMV remains a viable tool for ExM. A major advantage

of using TMV particles as rulers is the ability to measure isotropic expansion in three dimensions, which is a challenge that has not yet been solved with any of the tools developed to date. Even if only the first concern is addressed, labeled TMV particles could function as a ruler to detect anisotropies in specific regions of interest at the nanoscale. However, this would require a reference image prior to ExM. Nevertheless, these studies contribute to the development of a reliable calibration for ExM, enabling the long-term trust of results obtained from high-resolution post ExM images.

4 Materials and Methods

4.1 Materials

Table 2: Reagents used in this study.

REAGENTS	SOURCE
2% LMP Agarose	Promega, V3841
Abberior Star 580	Abberior, ST580-0002-1MG
Abberior Star 635P NHS	Abberior, ST635P-0002-1MG
Abberior Star Red NHS	Abberior, STRED-0002-1MG
acrylamide	Sigma Aldrich, A4058-100ML
AcX	Thermo Fisher, A20770
Anti-alpha-tubulin antibody	Sigma Aldrich, T5168
Anti-beta-tubulin antibody	Sigma Aldrich, T5293
Anti-CHC-AF647	Invitrogen, MA1-065-A647
Anti-GFP antibody	Thermo Fisher, A-11120
Anti-GFP nanobody	Chromotek, 2631361
Anti-mouse Abberior Star Red antibody	Abberior, STRED-1001-500UG
Anti-mouse IgG	Jackson Immune Research, 715-005-151
Anti-rabbit IgG	Jackson Immuno Research, 111-005-003
Anti-rabbit-AF594	Invitrogen, A11072
Anti-SNAP nanobody	Chromotek, 2827564
Anti-TMV-antibody	Creative Diagnostics, CABT-B1023P
APS	Carl Roth, 9592.2
Atto488 NHS	Atto-tec, AD488-31
Biotin NHS	Thermo Fisher
BIS	Sigma Aldrich, M1533-25ML
BSA	Carl Roth, 8076.4
DMEM	Life technologies
EDTA	Carl Roth, 8040.3
FCS	Life technologies
Glutamax	Life technologies
Glutaraldehyde	Electron Microscopy Sciences, 16316-10
Goat serum	Gibco
Hellmanex	Hellma Analytics, 9-307-011-4-507
Image IT FX	Thermo fisher, 136933
JF-SNAP-552	Luke Lavis Lab (Grimm *et al.*, 2020)
Lipofectamine	Thermo fisher, L3000-015
Methanol	Chem Solute, 1428.2500

NaCl	**Acros organics, 747-14-5**
$NaHCO_3$	Carl Roth, 144-55-8
NH_4Cl	Merck, 12125-02-9
PFA	Thermo fisher, 28908
Poly-L-lysine	Sigma Aldrich, P8920
Proteinase K	New England Biolabs (NEB), , P8107S
SNAP-Cell 647-SIR	NEB, S9102S
SNAP-Cell TMR-Star	NEB, S9105S
SNAP-Surface AF647	NEB, S9136S
Sodium acrylate	Sigma Aldrich, 408220-100G
Streptavidin	Sigma Aldrich, 85878-1MG
Streptavidin atto565	Atto-tec, AD565-61
TEMED	Carl Roth, 2367.3
TMV_{Lys}	Prof. Dr. Christina Wege
Tris-HCl	Carl Roth, 4855
Trition X-100	Sigma Aldrich, T-9284

Table 3: Further materials and equipment used for this work.

MATERIAL/DEVICE	SPECIFICATION	SOURCE
Glass bottom imaging dishes	170 µm cover glass bottom, #1.5 coverslips	Zell-Kontakt, 6160-168
Glass coverslips	Round 18 mm #1.5 coverslips	VWR, 631-0153
Microplate reader	EZ read 2000 microplate reader, Galapagos software	Biochrom
Nanodrop	Nanodrop 1000 spectrophotometer, serial no.: F237	Thermo Scientific
Spinning disc confocal microscope	inverted Olympus IX71 microscope equipped with a Yokogawa CSU-X1 spinning disk, 60×/1.42 NA oil Olympus objective, 10x/0.30 NA air Olympus objective, sCMOS camera (Hamamatsu)	Olympus
STED microscope	Abberior STED system with an 100×/1.4 NA oil uPlanSApo Olympus objective	Abberior
TEM	SU8030	Hitachi
Zebra spin desalting columns	7 kDa molecular weight cut off	Thermo fisher, 89882

Table 4: Buffers used for this study.

BUFFERS	COMPOSITION
Blocking buffer 1	3% BSA, 4% goat serum, 0.1% Triton X-100 in PBS
Blocking buffer 2	10% goat serum, 0.3% Triton X-100 in PBS
Cell culture medium	10% FBS and 1% glutamax in DMEM
Digestion buffer	50 mM Tris-HCl, 1 mM EDTA, 0.5% Triton X-100, 1 M NaCl, pH 8.0
Labeling buffer 1	30 mM HEPES, 350 mM NaCl, pH 7.5
Labeling buffer 2	0.2 M $NaHCO_3$
Monomer solution	2.5% AA, 0.15% BIS, 2 M NaCl, 8.625% SA in PBS
PBS	137 mM NaCl, 2.7 mM KCl, 10 mM Na_2HPO_4, 1.8 mM KH_2PO_4, pH 7.4
PHEM buffer	60 mM PIPES, 25 mM HEPES, 10 mM EGTA, 2 mM $MgCl_2$, pH 6.9
SNAP-dye buffer	1 mM DTT, 1% BSA in PBS
Sodium-potassium-phosphate-buffer	100 mM KH_2PO_4, NaCl, pH 7.2

Table 5: Plasmid constructs used for transfection.

PLASMID CONSTRUCT	SOURCE
SNAP-CLC-YFP	Addgene, 38011 (Jones *et al.*, 2011)
SNAP-tubulin	Addgene, 136791

Table 6: Cell lines used for this study.

CELL LINE	SOURCE
U2OS-NUP96-SNAP	Prof. Dr. Jonas Ries
U2OS-NUP96-GFP	Prof. Dr. Jonas Ries
NRK52E-S2-SNAP	(Banko *et al.*, 2019), further genomically edited by Claire Schlack-Leigers to introduce SNAP tag
NRK49F-S2-SNAP	(Banko *et al.*, 2019) further genomically edited by Claire Schlack-Leigers to introduce SNAP tag
NRK49F-S2-GFP	(Banko *et al.*, 2019)
CV1	ATCC
HeLa	ATCC

4.2 Methods

4.2.1 Cell culture, fixation, staining

Staining of nuclear pores.

U2OS-NUP96-SNAP cells and U2OS-NUP96-GFP cells were cultured in DMEM medium containing 10% FCS and 1% glutamax. The cells were then fixed and stained following the protocol of Thevathasan *et al.*, 2019 consisting of fixation with 2.4% PFA in PBS for 20 sec, permeabilization with 0.4% Triton X-100 for 3 min, and a final fixation with 2.4% PFA for 20 min. Quenching was performed by treating the cells with 100 mM NH_4Cl for 5 min and then washing them with PBS two times for 5 min each. U2OS-NUP96-SNAP cells were blocked with Image IT FX for 1 h, while U2OS-NUP96-GFP cells were treated with blocking buffer 1 for the same time period. After blocking, U2OS-NUP96-SNAP cells were incubated with 1 µM of either BG-TMR-MA, SNAP-Cell TMR-Star, BG-TMR-Boc, SNAP-Cell 647-SIR, SNAP-Surface AF647 or JF-SNAP-552 in SNAP-dye buffer for 1 h at room temperature (RT). Meanwhile, U2OS-NUP96-GFP cells were stained with an anti-GFP antibody and detected using an anti-mouse Abberior Star Red secondary antibody.

SNAP-CLC-YFP and SNAP-tubulin transfection and staining.

CV1 cells were cultured in medium containing 10% FBS and 1% glutamax in DMEM. Cells were seeded onto 18 mm coverslips and transfected the following day with either 1 µg SNAP-CLC-YFP (Jones *et al.*, 2011) or 0.4 µg SNAP-tubulin, using lipofectamine. For SNAP-CLC-YFP, fixation was performed 24 h after transfection with 4% PFA in PBS for 13 min. Quenching was performed with 50 mM NH_4Cl for 10 min, followed by two PBS washes of 5 min each. For SNAP-tubulin, fixation was performed 48 h after transfection with -20°C methanol for 7 min at -20°C, followed by four PBS washes. Cells were blocked for 1 h using Image IT FX and either blocking buffer 2 for SNAP-CLC-YFP expressing cells or blocking buffer 1 for SNAP-tubulin expressing cells. Staining was performed with 1 µM BG-TMR-MA or 1 µM SNAP-Cell TMR-Star in SNAP-dye buffer for 1 h at RT. For tubulin co-staining, cells were additionally incubated with anti-alpha- and anti-beta-tubulin antibodies for 1 h,

washed three times with PBS, and incubated with secondary anti-mouse Abberior Star Red antibody for 45 min, followed by three washes with PBS.

Live cell staining.

To perform nuclear pore staining in live cells, SNAP-Cell TMR-Star and BG-TMR-MA were diluted to a final concentration of 1 µM in complete medium at 37°C. The culture medium was replaced with this medium and the cells were labeled at 37°C for 5 and 30 min, respectively, followed by three washes with medium. Cells were incubated in fresh medium for 30 min. The medium was changed again and 1 h later the cells were fixed in 2.4% PFA for 30 min, followed by quenching with 100 mM NH_4Cl for 10 min. Fixed cells were washed twice with PBS and imaged.

Staining of septin 2.

NRK52E-S2-SNAP and NRK49F-S2-SNAP cells were cultured in medium with 10% FBS and 1% glutamax in DMEM. The cells were seeded onto 18 mm coverslips and fixed the following day with 37°C warm 4% PFA in PHEM buffer for 15 min at RT. Prior to fixation, the cells were washed quickly with pre-warmed PHEM buffer. Quenching was performed by treating the cells with 50 mM NH_4Cl for 20 min and then washing them with PBS two times for 5 min each. Cells were blocked with blocking buffer 1 for 30 min and Image IT FX for 1 h. After blocking, cells were incubated with either 500 nM BG-TMR-MA or 500 nM BG-TMR-Boc in Snap-dye buffer for 1 h, followed by three PBS washes.

4',6-diamidino-2-phenylindole (DAPI) staining.

For DAPI staining, cells were incubated with 0.025 mg/mL DAPI for 10 min after complete staining. The cells were then washed twice with PBS.

4.2.2 Nanobody and antibody labeling

Anti-SNAP-nanobody, anti-GFP-nanobody, anti-alpha- and anti-beta-tubulin antibodies were labeled with a 10-fold molar excess of AcX in labeling buffer (30 mM HEPES, 350 mM NaCl, pH 7.5) for 1h at RT. Two rounds of purification were carried out using 7K-Zebra spin desalting columns following the manufacturer's protocol. For the AcX local delivery experiments, nanobodies labeled with AcX were diluted 1:100 in PBS and anchoring was performed overnight at 4°C.

4.2.3 TMV labeling

TMV_{Lys} particles (a gift from Prof. Dr. Christina Wege) were labeled with different molar excesses (Table 1) of the following dyes: Abberior Star Red NHS, Abberior Star 580 NHS, Abberior Star 635P NHS and Atto488 NHS in labeling buffer (0.2 M $NaHCO_3$ or 30 mM HEPES, 350 mM NaCl, pH 7.5) for 1 h at RT. For biotinylation, TMV particles were additionally labeled with a 4- or 40-fold molar excess of biotin. Dye labeling and biotinylation were performed simultaneously. For two-color STED imaging anti-mouse IgG antibodies were labeled with a 10-fold molar excess of Abberior Star 580 NHS in 0.2 M $NaHCO_3$ for 1 h at RT. Two rounds of purification were performed using 7K-Zebra Spin desalting columns according to the manufacturer's protocol.

4.2.4 TMV on poly-L-lysine coated coverslips

18 mm round coverslips were cleaned with ethanol and dried. Alternatively, coverslips were cleaned in 2% Hellamanex in an ultrasonic bath for 10-20 min, washed 4x with Milli-Q water, washed with 99.6% ethanol in an ultrasonic bath for 5 min, dried, and placed in a plasma cleaner for 10 min. Coverslips were then incubated with 0.1 g/L poly-L-Lysine for 40 min and washed with Milli-Q-water. Afterwards TMV particles were incubated for 1 h at RT and washed two times with PBS. Samples were post-fixed with 100% methanol for 7 min at -20°C, followed by three washes with PBS. For ExM, TMV particles were anchored by incubating them with 0.25% GA for 10 min, then washing them twice with PBS.

4.2.5 TMV delivery into cells

HeLa cells were cultured in medium with 10% FCS and 1% glutamax in DMEM and seeded on 18 mm round coverslips. Fixation was done with -20°C methanol for 7 min at -20°C, followed by four PBS washing steps. The protein concentration of the labeled probes ($TMV_{StarRed-Biotin}$, biotinylated primary anti-alpha-tubulin and anti-beta-tubulin antibodies) was measured using a nanodrop. This was done to ensure consistent incubation ratios of the probes. Cells were incubated with 0.08 mg/mL of biotinylated primary antibodies against alpha-tubulin and beta-tubulin for 1 h at RT. This was followed by washing with PBS three times. Coverslips were then placed face down on parafilm containing 50 µl drops of streptavidin at a concentration of 1 mg/mL, and subsequently washed with PBS three times. Afterwards, the cells were stained with secondary anti-mouse Abberior Star 580 antibody and $TMV_{StarRed-Biotin}$ for 30 min at RT and washed with PBS three times. Samples were post-fixed with 100% methanol for 7 min at -20°C and rinsed three times with PBS. For ExM, samples were anchored with 0.1 mg/mL AcX at 4°C overnight.

4.2.6 Gelation, digestion, expansion

Gelation, digestion, and expansion were performed according to Tillberg *et al.*, 2016 with minor modifications. Briefly, stained specimens were incubated overnight at 4°C in 1 mg/mL, 0.1 mg/mL, or 0.01 mg/mL AcX, washed with PBS thrice, and subsequently moved to a monomer solution for a 10-min incubation. Hydrogel formation was achieved by adding APS and TEMED to reach a final concentration of 0.2% each. The polymerization reaction occurred in a humidity chamber at 37°C for 1 h. For the digestion procedure, proteinase K was diluted to a concentration of 8 U/mL in the digestion buffer. The gels were then incubated in the mixture of proteinase K and digestion buffer for 1 h at 37°C. After washing the digested gels with Milli-Q water twice, they were fully submerged in Milli-Q water in petri dishes. The water was changed two to three times until the expansion stabilized.

4.2.7 Confocal microscopy

Pre ExM, after gelation, after digestion and post ExM confocal imaging were performed on an inverted Olympus IX71 microscope equipped with a Yokogawa CSU-X1 spinning disk. A 60×/1.42 NA oil Olympus objective or a 10×/0.30 NA air Olympus objective were used together with a 405 nm (100 mW; Cobolt) and a 561 nm (100 mW; Cobolt) laser. Final images were taken with an sCMOS camera (Hamamatsu).

For correlative pre and post ExM imaging of the same cells, overview images of a small ROI were taken with a 10× objective. Additionally, adjacent regions to the ROI were imaged using the 10× objective to generate a map for better location of the ROI after expansion. Particular attention was given to cells that were larger or had a specific shape that facilitated relocation of the area after expansion. The ROI imaged pre ExM was marked with a cross at the bottom of the coverslip. Subsequently, upon gelation and removal of the coverslip, only the marked area was cut out in an irregular triangular shape. This ensured that the ROI was expanded and the gel was kept as small as possible to make it easier to find the ROI again after the expansion. In addition, the irregular shape of the gel made it easier to find the cells in the same orientation after expansion.

To reduce drift expanded samples were mounted in 2% low melting point (LMP) agarose.

4.2.8 STED microscopy

STED microscopy was performed on an Abberior STED system with a 100×/1.4 NA oil uPlanSApo Olympus objective. Abberior Star Red was excited at 630-650 nm, Abberior Star 580 was excited at 587 nm and BG-TMR-MA was excited at 554 nm, while a 775 nm pulsed laser was utilized for depletion. Imaging of nuclear pores was performed from a single focal plane from the bottom of the nucleus and the pixel size was set to 10 nm. For imaging of TMV particles, the pixel size was set to 20 nm, and for 3D STED imaging, the step size was set to 300 nm.

4.2.9 TEM

TMV_{Lys} particles with a stock concentration of 10 µg/µL were diluted to 0.1 µg/µL in 10 mM sodium-potassium-phosphate-buffer, pH 7.2. TEM imaging was performed by Iwona Mucha-Kruczynska. Therefore, a small amount of the mixture was applied to an EM grid and air dried. Imaging was conducted using a transmission electron microscope at 11 kV and 92 kV.

4.2.10 Absorption measurement

Absorption measurement was performed using a microplate reader and a 96-well plate with three replicates for each condition. To enhance the signal-to-noise ratio, a high dye concentration of 10 µM BG-TMR-MA and 10 µM SNAP-Cell TMR-Star was employed. Measurements were taken with a microplate reader and the wavelength was set to 562 nm. SNAP-dye buffer without dye was used as background, and this value was subtracted from the absolute values accordingly. To measure the dye absorption in the polymerized gel, a polymerized gel lacking dye was utilized as the background.

4.2.11 Image analysis

Images were analyzed utilizing Fiji software (Schindelin *et al.*, 2012). Each set of images belonging to the same treatment, e.g. after gelation, have the same intensity scaling to compare fluorescence intensities. Fiji's line drawing feature was used to measure the expanded nuclear pore diameter, which was used to calculate the expansion factors. Similarly, Fiji's freehand selection tool was used to measure the nuclear area before and after expansion to calculate the expansion factors. For measuring fluorescence intensity, cells were selected and their fluorescence intensity was assessed using Fiji. A background region adjacent to the cell exhibiting no fluorescence was selected. An average background value from n=3 for each condition was calculated and subtracted from the absolute intensity values. Results were normalized to the maximum intensity value (arbitrary units) for clear comparison. Each dot on the plots represents a single cell. Cells were derived from different experiments.

For statistical analysis, the normal distribution of the data was assessed. If they were normally distributed, an unpaired T-test under the assumption of unequal variances was used to test for significant differences between two parameters. Otherwise, the Mann-Whitney test was used.

For distortion analysis images of the same cell pre and post expansion were used as input for a python code provided by (Truckenbrodt *et al.*, 2019). A slight modification to the expansion factor range was made in the code, as the cited protocol was originally intended for X10 microscopy. Therefore, the expansion factor range had to be adjusted and was set to 3-5. The resulting overlaid images were used as input into a Jupyter notebook, which generated the deformation vector map and the plots displaying the angular distribution of deformation vectors.

4.2.12 Schematic figures

Schematics were created with Inkscape and BioRender.com. ChemSketch was used to draw the chemical structures.

References

Alon, S. *et al.* (2021) 'Expansion sequencing: Spatially precise in situ transcriptomics in intact biological systems', *Science*, 371(6528). doi: 10.1126/science.aax2656.

Ambrose, E. J. (1956) 'A Surface Contact Microscope for the study of Cell Movements', *Nature 1956 178:4543*. Nature Publishing Group, 178(4543), pp. 1194–1194. doi: 10.1038/1781194a0.

Asurmendi, S. *et al.* (2007) 'Aggregation of TMV CP plays a role in CP functions and in Coat-Protein Mediated Resistance', *Virology*. NIH Public Access, 366(1), p. 98. doi: 10.1016/J.VIROL.2007.03.014.

Axelrod, D. (1981) 'Cell-substrate contacts illuminated by total internal reflection fluorescence.', *Journal of Cell Biology*. The Rockefeller University Press, 89(1), pp. 141–145. doi: 10.1083/JCB.89.1.141.

Banko, M. *et al.* (2019) 'A homozygous genome-edited Sept2-EGFP fibroblast cell line', *Cytoskeleton*, 76(1), pp. 73–82. doi: 10.1002/cm.21518.

Bastide, J. and Leibler, L. (1988) 'Large-Scale Heterogeneities in Randomly Cross-Linked Networks', *Macromolecules*. American Chemical Society, 21(8), pp. 2647–2649. doi: 10.1021/MA00186A058.

Beija, M., Afonso, C. A. M. and Martinho, J. M. G. (2009) 'Synthesis and applications of rhodamine derivatives as fluorescent probes', *Chemical Society Reviews*. The Royal Society of Chemistry, 38(8), pp. 2410–2433. doi: 10.1039/b901612k.

Betzig, E. *et al.* (2006) 'Imaging Intracellular Fluorescent Proteins at Nanometer Resolution', *Science*, 313(5793), pp. 1642–1645. doi: 10.1126/science.1127344.

Bhanu, V. A. and Kishore, K. (1991) 'Role of oxygen in polymerization reactions', *Chemical Reviews*. American Chemical Society, 91(2), pp. 99–117. doi: 10.1021/cr00002a001.

Blatchley, Michael R *et al.* (2022) 'In Situ Super-Resolution Imaging of Organoids and Extracellular Matrix Interactions via Phototransfer by Allyl Sulfide Exchange-Expansion Microscopy (PhASE-ExM)', *Advanced Materials*. John Wiley & Sons, Ltd, 34(16), p. 2109252. doi: 10.1002/ADMA.202109252.

Bruckman, M. A. and Steinmetz, N. F. (2014) 'Chemical modification of the inner and outer surfaces of Tobacco Mosaic Virus (TMV)', *Methods in Molecular Biology*. Humana Press Inc., 1108, pp. 173–185. doi: 10.1007/978-1-62703-751-8_13.

Buchholz, F. L. (1994) 'Preparation Methods of Superabsorbent Polyacrylates', in *Superabsorbent Polymers*, pp. 27–38. doi: 10.1021/bk-1994-0573.ch002.

Bürgers, J. *et al.* (2019) 'Light-sheet fluorescence expansion microscopy: fast mapping of neural circuits at super resolution', *Neurophotonics*. International Society for Optics and

Photonics, 6(01), p. 1. doi: 10.1117/1.NPh.6.1.015005.

Büttner, M. *et al.* (2021) 'Challenges of Using Expansion Microscopy for Super-resolved Imaging of Cellular Organelles', *ChemBioChem*. Wiley-VCH Verlag, 22(4), pp. 686–693. doi: 10.1002/cbic.202000571.

Chang, J. B. *et al.* (2017) 'Iterative expansion microscopy', *Nature Methods*. doi: 10.1038/nmeth.4261.

Chen, F. *et al.* (2016) 'Nanoscale imaging of RNA with expansion microscopy', *Nature Methods*. Nature Publishing Group, 13(8), pp. 679–684. doi: 10.1038/nmeth.3899.

Chen, F., Tillberg, P. W. and Boyden, E. S. (2015) 'Expansion microscopy', *Science*, 347(6221), pp. 543–548. doi: 10.1126/science.1260088.

Chen, L. *et al.* (2021) 'Applications of Super Resolution Expansion Microscopy in Yeast', *Frontiers in Physics*. Frontiers Media SA, 9, p. 650353. doi: 10.3389/fphy.2021.650353.

Chen, R. *et al.* (2021) 'Expansion tomography for large volume tissue imaging with nanoscale resolution', *Biomedical Optics Express*, 12(9), p. 5614. doi: 10.1364/BOE.431696.

Chozinski, T. J. *et al.* (2016) 'Expansion microscopy with conventional antibodies and fluorescent proteins', *Nature Methods 2016 13:6*. Nature Publishing Group, 13(6), pp. 485–488. doi: 10.1038/nmeth.3833.

Cole, N. B. (2013) 'Site-specific protein labeling with SNAP-tags', *Current Protocols in Protein Science*. Blackwell Publishing Inc., 2013, pp. 30.1.1-30.1.16. doi: 10.1002/0471140864.ps3001s73.

Cui, Y. *et al.* (2022) 'A Multifunctional Anchor for Multimodal Expansion Microscopy', *bioRxiv*. Cold Spring Harbor Laboratory. doi: 10.1101/2022.06.19.496699.

Damstra, H. G. J. *et al.* (2022) 'Visualizing cellular and tissue ultrastructure using Ten-fold Robust Expansion Microscopy (TREx)', *eLife*. eLife Sciences Publications Ltd, 11. doi: 10.7554/ELIFE.73775.

Damstra, H. G. J. *et al.* (2023) 'GelMap: intrinsic calibration and deformation mapping for expansion microscopy', *Nature Methods*. Springer Science and Business Media LLC. doi: 10.1038/s41592-023-02001-y.

Datta, P. and Genzer, J. (2016) '"Grafting through" polymerization involving surface-bound monomers', *Journal of Polymer Science Part A: Polymer Chemistry*. John Wiley and Sons Inc., 54(2), pp. 263–274. doi: 10.1002/pola.27907.

David Egger, M. and Petran, M. (1967) 'New reflected-light microscope for viewing unstained brain and ganglion cells', *Science (New York, N.Y.)*. Science, 157(3786), pp. 305–307. doi: 10.1126/SCIENCE.157.3786.305.

Davidovits, P. and Egger, M. D. (1969) 'Scanning Laser Microscope', *Nature 1969 223:5208*. Nature Publishing Group, 223(5208), pp. 831–831. doi: 10.1038/223831a0.

Day, J. H. *et al.* (2023) 'HiExM: high-throughput expansion microscopy enables scalable super-resolution imaging', *bioRxiv : the preprint server for biology*. bioRxiv. doi: 10.1101/2023.02.07.527509.

Düring, D. N. *et al.* (2019) 'Expansion Light Sheet Microscopy Resolves Subcellular Structures in Large Portions of the Songbird Brain', *Frontiers in Neuroanatomy*, 13(January), pp. 1–7. doi: 10.3389/fnana.2019.00002.

Einstein, A. (1916) 'Strahlungs-Emission und -Absorption nach der Quantentheorie', *DPhyG*, 18, pp. 318–323. Available at: https://ui.adsabs.harvard.edu/abs/1916DPhyG..18..318E/abstract (Accessed: 16 January 2024).

Freifeld, L. *et al.* (2017) 'Expansion microscopy of zebrafish for neuroscience and developmental biology studies', *Proceedings of the National Academy of Sciences of the United States of America*. National Academy of Sciences, 114(50), pp. E10799–E10808. doi: 10.1073/pnas.1706281114.

Gambarotto, D. *et al.* (2019) 'Imaging cellular ultrastructures using expansion microscopy (U-ExM)', *Nature Methods*, 16, pp. 71–74. doi: 10.1038/s41592-018-0238-1.

Gao, M. *et al.* (2018) 'Expansion Stimulated Emission Depletion Microscopy (ExSTED).', *ACS nano*, 12, pp. 4178–4185. doi: 10.1021/acsnano.8b00776.

Gao, R. *et al.* (2019) 'Cortical column and whole-brain imaging with molecular contrast and nanoscale resolution.', *Science (New York, N.Y.)*. American Association for the Advancement of Science, 363(245), pp. 1–16. doi: 10.1126/science.aau8302.

Gao, R. *et al.* (2021) 'A highly homogeneous polymer composed of tetrahedron-like monomers for high-isotropy expansion microscopy', *Nature Nanotechnology*. Nature Research, 16(6), pp. 698–707. doi: 10.1038/s41565-021-00875-7.

Geiger, F. C. *et al.* (2013) 'TMV nanorods with programmed longitudinal domains of differently addressable coat proteins', *Nanoscale*. The Royal Society of Chemistry, 5(9), pp. 3808–3816. doi: 10.1039/C3NR33724C.

Göttfert, F. *et al.* (2017) 'Strong signal increase in STED fluorescence microscopy by imaging regions of subdiffraction extent', *Proceedings of the National Academy of Sciences*, 114(9), pp. 2125–2130. doi: 10.1073/pnas.1621495114.

Götz, R., Panzer, S., *et al.* (2020) 'Expansion Microscopy for Cell Biology Analysis in Fungi', *Frontiers in Microbiology*. Frontiers Media S.A., 11, p. 574. doi: 10.3389/fmicb.2020.00574.

Götz, R., Kunz, T. C., *et al.* (2020) 'Nanoscale imaging of bacterial infections by sphingolipid expansion microscopy', *Nature Communications*. Nature Research, 11(1), pp. 1–9. doi: 10.1038/s41467-020-19897-1.

Gould, T. J. *et al.* (2012) 'Adaptive optics enables 3D STED microscopy in aberrating specimens.', *Optics express*. Optical Society of America, 20(19), pp. 20998–1009. doi: 10.1364/OE.20.020998.

Grimm, J. B. *et al.* (2020) 'A general method to optimize and functionalize red-shifted rhodamine dyes', *Nature methods*. Nat Methods, 17(8), pp. 815–821. doi: 10.1038/S41592-020-0909-6.

Günay, K. A. *et al.* (2023) 'Photo-expansion microscopy enables super-resolution imaging of cells embedded in 3D hydrogels', *Nature Materials 2023 22:6*. Nature Publishing Group, 22(6), pp. 777–785. doi: 10.1038/s41563-023-01558-5.

Gustafsson, M. G. L. (2000) 'Surpassing the lateral resolution limit by a factor of two using structured illumination microscopy. SHORT COMMUNICATION', *Journal of Microscopy*. John Wiley & Sons, Ltd, 198(2), pp. 82–87. doi: 10.1046/j.1365-2818.2000.00710.x.

Hall Vol, C. E. and Cecil Hall, B. E. (1958) 'Lengths of Tobacco Mosaic Virus from Electron Microscopy1', *Public Health Service*, 80(2), p. 2057. Available at: https://pubs.acs.org/sharingguidelines (Accessed: 14 November 2023).

Halpern, A. R. *et al.* (2017) 'Hybrid Structured Illumination Expansion Microscopy Reveals Microbial Cytoskeleton Organization', *ACS Nano*. American Chemical Society, 11(12), pp. 12677–12686. doi: 10.1021/acsnano.7b07200.

Heilemann, M. *et al.* (2008) 'Subdiffraction-Resolution Fluorescence Imaging with Conventional Fluorescent Probes', *Angewandte Chemie International Edition*. John Wiley & Sons, Ltd, 47(33), pp. 6172–6176. doi: 10.1002/anie.200802376.

Heimstaedt, O. (1911) 'Das Fluoreszenzmikroskop', *Zeitschrift für wissenschaftliche Mikroskopie und mikroskopische Technik*. Stuttgart [etc.]: S. Hirzel [etc.], bd. 28 (19, pp. 330–337. Available at: https://www.biodiversitylibrary.org/item/25024 (Accessed: 29 November 2023).

Heine, J. *et al.* (2017) 'Adaptive-illumination STED nanoscopy', *Proceedings of the National Academy of Sciences of the United States of America*, 114(37), pp. 9797–9802. doi: 10.1073/pnas.1708304114.

Hell, S. W. and Wichmann, J. (1994) 'Breaking the diffraction resolution limit by stimulated emission: stimulated-emission-depletion fluorescence microscopy', *Optics Letters*. Optical Society of America, 19(11), p. 780. doi: 10.1364/OL.19.000780.

Henze, M. *et al.* (2014) '"Grafting Through": Mechanistic Aspects of Radical Polymerization Reactions with Surface-Attached Monomers', *Macromolecules*. American Chemical Society, 47(9), pp. 2929–2937. doi: 10.1021/ma402607d.

Heuser, J. and Evans, L. (1980) 'Three-dimensional visualization of coated vesicle formation in fibroblasts', *The Journal of Cell Biology*. The Rockefeller University Press, 84(3), p. 560. doi: 10.1083/JCB.84.3.560.

Huang, S. H. *et al.* (2018) 'Whispering gallery mode resonator sensor for in situ measurements of hydrogel gelation', *Optics Express, Vol. 26, Issue 1, pp. 51-62*. Optica Publishing Group, 26(1), pp. 51–62. doi: 10.1364/OE.26.000051.

Hulett, H. R. and Loring, H. S. (1965) 'Effect of particle length distribution on infectivity of tobacco mosaic virus', *Virology*. Academic Press, 25(3), pp. 418–430. doi: 10.1016/0042-6822(65)90063-2.

Jabłonski, A. (1933) 'Efficiency of Anti-Stokes Fluorescence in Dyes', *Nature 1933 131:3319*. Nature Publishing Group, 131(3319), pp. 839–840. doi: 10.1038/131839b0.

Jiang, N. *et al.* (2018) 'Superresolution imaging of *Drosophila* tissues using expansion microscopy', *Molecular Biology of the Cell*. Edited by D. Montell. American Society for Cell Biology, 29(12), pp. 1413–1421. doi: 10.1091/mbc.E17-10-0583.

Jones, S. A. *et al.* (2011) 'Fast, three-dimensional super-resolution imaging of live cells', *Nature Methods*, 8(6), pp. 499–505. doi: 10.1038/nmeth.1605.

Jungmann, R. *et al.* (2010) 'Single-molecule kinetics and super-resolution microscopy by fluorescence imaging of transient binding on DNA origami', *Nano Letters*, 10(11), pp. 4756–4761. doi: 10.1021/nl103427w.

Kang, M. *et al.* (2021) 'Prelabeling Expansion Single-Molecule Localization Microscopy with Minimal Linkage Error', *ChemBioChem*. Wiley-VCH Verlag, p. cbic.202000772. doi: 10.1002/cbic.202000772.

Kang, S. *et al.* (2021) 'Expansion Microscopy with a Thermally Adjustable Expansion Factor Using Thermoresponsive Biospecimen-Hydrogel Hybrids', *ACS Applied Materials and Interfaces*. American Chemical Society, 13(24), pp. 28962–28974. doi: 10.1021/acsami.1c07592.

Kao, P. and Nodine, M. D. (2019) 'Transcriptional Activation of Arabidopsis Zygotes Is Required for Initial Cell Divisions', *Scientific Reports 2019 9:1*. Nature Publishing Group, 9(1), pp. 1–11. doi: 10.1038/s41598-019-53704-2.

Kao, P. and Nodine, M. D. (2021) 'Application of expansion microscopy on developing Arabidopsis seeds', in *Methods in Cell Biology*. Academic Press Inc., pp. 181–195. doi: 10.1016/bs.mcb.2020.06.004.

Keppler, A. *et al.* (2004) 'Labeling of fusion proteins of O6-alkylguanine-DNA alkyltransferase with small molecules in vivo and in vitro', *Methods*. Methods, 32(4), pp. 437–444. doi: 10.1016/j.ymeth.2003.10.007.

Kim, D., Kim, T., Lee, J. and Shim, S. (2019) 'Amplified Expansion Stimulated Emission Depletion Microscopy', *ChemBioChem*. Wiley-VCH Verlag, 20(10), pp. 1260–1265. doi: 10.1002/cbic.201800775.

Kim, D., Kim, T., Lee, J. and Shim, S. H. (2019) 'Amplified Expansion Stimulated Emission Depletion Microscopy', *ChemBioChem*, 20(10), pp. 1260–1265. doi: 10.1002/cbic.201800775.

Kizilay, M. Y. and Okay, O. (2003) 'Effect of hydrolysis on spatial inhomogeneity in poly(acrylamide) gels of various crosslink densities', *Polymer*, 44(18), pp. 5239–5250. doi: 10.1016/S0032-3861(03)00494-4.

Klar, T. A. *et al.* (2000) 'Fluorescence microscopy with diffraction resolution barrier broken by stimulated emission.', *Proceedings of the National Academy of Sciences of the United States of America*. National Academy of Sciences, 97(15), pp. 8206–10. doi: 10.1073/pnas.97.15.8206.

Klar, T. A. and Hell, S. W. (1999) 'Subdiffraction resolution in far-field fluorescence microscopy', *Optics Letters*. The Optical Society, 24(14), p. 954. doi: 10.1364/ol.24.000954.

Klimas, A. *et al.* (2023) 'Magnify is a universal molecular anchoring strategy for expansion microscopy', *Nature Biotechnology*. Nature Research, pp. 1–12. doi: 10.1038/s41587-022-01546-1.

Kraft, N. *et al.* (2023) 'Expansion microscopy in honeybee brains for high - resolution neuroanatomical analyses in social insects', *Cell and Tissue Research*. Springer Berlin Heidelberg, (0123456789). doi: 10.1007/s00441-023-03803-4.

Ku, T. *et al.* (2016) 'Multiplexed and scalable super-resolution imaging of three-dimensional protein localization in size-adjustable tissues', *Nature Biotechnology*. Nature Publishing Group, 34(9), pp. 973–981. doi: 10.1038/nbt.3641.

Laporte, M. H. *et al.* (2022) 'Visualizing the native cellular organization by coupling cryofixation with expansion microscopy (Cryo-ExM)', *Nature Methods*. Nature Research, 19(2), pp. 216–222. doi: 10.1038/s41592-021-01356-4.

Lauffer, M. A. (1938) 'The Molecular Weight and Shape of Tobacco Mosaic Virus Protein', *Science*. American Association for the Advancement of Science, 87(2264), pp. 469–470. doi: 10.1126/science.87.2264.469.

Lauffer, M. A. (1944) 'The Size and Shape of Tobacco Mosaic Virus Particles 1', *Journal of the American Chemical Society*, 66(7), pp. 1188–1194. doi: 10.1021/ja01235a037.

Lavis, L. D. (2017) 'Teaching Old Dyes New Tricks: Biological Probes Built from Fluoresceins and Rhodamines'. doi: 10.1146/annurev-biochem.

Lee, H. *et al.* (2021) 'Tetra-gel enables superior accuracy in combined super-resolution imaging and expansion microscopy', *Scientific Reports*. Nature Research, 11(1). doi: 10.1038/s41598-021-96258-y.

Lee, M. Y. *et al.* (2022) 'Fluorescent labeling of abundant reactive entities (FLARE) for cleared-tissue and super-resolution microscopy', *Nature Protocols 2022 17:3*. Nature Publishing Group, 17(3), pp. 819–846. doi: 10.1038/s41596-021-00667-2.

Li, H. *et al.* (2022) 'Expansion microscopy with ninefold swelling (NIFS) hydrogel permits cellular ultrastructure imaging on conventional microscope', *Science Advances*. American Association for the Advancement of Science, 8(18). doi: 10.1126/sciadv.abm4006.

Li, L. *et al.* (2022) 'Spatially resolved proteomics via tissue expansion', *Nature Communications 2022 13:1*. Nature Publishing Group, 13(1), pp. 1–13. doi: 10.1038/s41467-022-34824-2.

Lim, Y. *et al.* (2019) 'Mechanically resolved imaging of bacteria using expansion microscopy', *PLOS Biology*. Public Library of Science, 17(10), p. e3000268. doi: 10.1371/JOURNAL.PBIO.3000268.

Lindemann, B., Schröder, U. P. and Oppermann, W. (1997) 'Influence of the Cross-Linker Reactivity on the Formation of Inhomogeneities in Hydrogels', *Macromolecules*. American Chemical Society, 30(14), pp. 4073–4077. doi: 10.1021/ma961870x.

Di Lorenzo, F. and Seiffert, S. (2015) 'Nanostructural heterogeneity in polymer networks and gels', *Polymer Chemistry*. Royal Society of Chemistry, pp. 5515–5528. doi: 10.1039/c4py01677g.

Louvel, V. *et al.* (2023) 'iU-ExM: nanoscopy of organelles and tissues with iterative ultrastructure expansion microscopy', *Nature Communications 2023 14:1*. Nature Publishing Group, 14(1), pp. 1–18. doi: 10.1038/s41467-023-43582-8.

Lukinavičius, G., Reymond, L. and Johnsson, K. (2015) 'Fluorescent Labeling of SNAP-Tagged Proteins in Cells', in *Methods in molecular biology (Clifton, N.J.)*. Humana Press, New York, NY, pp. 107–118. doi: 10.1007/978-1-4939-2272-7_7.

M'Saad, O. and Bewersdorf, J. (2020) 'Light microscopy of proteins in their ultrastructural context', *Nature Communications*. Nature Research, 11(1), pp. 1–15. doi: 10.1038/s41467-020-17523-8.

Martínez, G. F. *et al.* (2020) 'Quantitative expansion microscopy for the characterization of the spectrin periodic skeleton of axons using fluorescence microscopy', *Scientific Reports*. Nature Research, 10(1), pp. 1–11. doi: 10.1038/s41598-020-59856-w.

Michalska, J. M. *et al.* (2023) 'Imaging brain tissue architecture across millimeter to nanometer scales', *Nature Biotechnology 2023*. Nature Publishing Group, pp. 1–14. doi: 10.1038/s41587-023-01911-8.

Min, K. *et al.* (2020) 'Multiplexed expansion microscopy of the brain through fluorophore screening', *Methods*. Academic Press Inc., 174, pp. 3–10. doi: 10.1016/j.ymeth.2019.07.017.

Minsky, M. (1957) '"Microscopy Apparatus". US Patent 3013467. USA'. Available at: https://worldwide.espacenet.com/patent/search/family/024791595/publication/US3013467A?q=pn%3DUS3013467.

Montagnac, G. *et al.* (2013) 'αTAT1 catalyses microtubule acetylation at clathrin-coated pits', *Nature 2013 502:7472*. Nature Publishing Group, 502(7472), pp. 567–570. doi: 10.1038/nature12571.

Mosca, T. J. *et al.* (2017) 'Presynaptic LRP4 promotes synapse number and function of excitatory CNS neurons', *eLife*. eLife Sciences Publications Ltd, 6. doi: 10.7554/ELIFE.27347.

Nakamoto, M. L. *et al.* (2022) 'Expansion Microscopy for Imaging the Cell–Material Interface', *ACS Nano*. American Chemical Society, 16(5), pp. 7559–7571. doi: 10.1021/acsnano.1c11015.

Nasu, T., Ozaki, Y. and Sato, H. (2021) 'Study of changes in water structure and interactions among water, CH2, and COO− groups during water absorption in acrylic acid-based super absorbent polymers using Raman spectroscopy', *Spectrochimica Acta Part A: Molecular and Biomolecular Spectroscopy*. Elsevier, 250, p. 119305. doi: 10.1016/J.SAA.2020.119305.

Nie, J., Du, B. and Oppermann, W. (2004) 'Influence of Formation Conditions on Spatial Inhomogeneities in Poly(N -isopropylacrylamide) Hydrogels', *Macromolecules*. American Chemical Society, 37(17), pp. 6558–6564. doi: 10.1021/ma049169d.

Nipkow, P. (1884) '"Elektrisches Teleskop". German patent 30105. Germany'. Available at: https://www.dpma.de/docs/dpma/veroeffentlichungen/de30105a_nipkow1884elektrischesteleskop.pdf.

Park, C. E. *et al.* (2020) 'Super-Resolution Three-Dimensional Imaging of Actin Filaments in Cultured Cells and the Brain via Expansion Microscopy', *ACS Nano*. American Chemical Society, 14(11), pp. 14999–15010. doi: 10.1021/acsnano.0c04915.

Park, H. E. *et al.* (2019) 'Scalable and Isotropic Expansion of Tissues with Simply Tunable Expansion Ratio', *Advanced Science*. Wiley-Blackwell, 6(22). doi: 10.1002/ADVS.201901673.

Patterson, G. H. and Lippincott-Schwartz, J. (2002) 'A Photoactivatable GFP for Selective Photolabeling of Proteins and Cells', *Science*. American Association for the Advancement of Science, 297(5588), pp. 1873–1877. doi: 10.1126/science.1074952.

Patton, B. R. *et al.* (2016) 'Three-dimensional STED microscopy of aberrating tissue using dual adaptive optics', *Optics Express*. Optical Society of America, 24(8), p. 8862. doi: 10.1364/OE.24.008862.

Pernal, S. P. *et al.* (2020) 'Nanoscale imaging using differential expansion microscopy', *Histochemistry and Cell Biology*. Springer Berlin Heidelberg, 153(6), pp. 469–480. doi: 10.1007/s00418-020-01869-7.

Pesce, L. *et al.* (2019) 'Measuring expansion from macro- to nanoscale using NPC as intrinsic reporter', *Journal of Biophotonics*. John Wiley & Sons, Ltd, 12(8). doi: 10.1002/jbio.201900018.

Pownall, M. E. *et al.* (2023) 'Chromatin expansion microscopy reveals nanoscale organization of transcription and chromatin', *Science*. American Association for the Advancement of Science, 381(6653), pp. 92–100. doi: 10.1126/SCIENCE.ADE5308.

Rathi, P. *et al.* (2023) 'Plasmon-Enhanced Expansion Microscopy', *Nano Letters*. American Chemical Society. doi: 10.1021/ACS.NANOLETT.3C01256.

Razzaq, A. *et al.* (2021) 'Molecular Biology Recent Developments in Halotag Technology', 10, p. 2021.

Reuss, M. *et al.* (2010) 'Birefringent device converts a standard scanning microscope into a STED microscope that also maps molecular orientation', *Optics Express, Vol. 18, Issue 2, pp. 1049-1058*. Optica Publishing Group, 18(2), pp. 1049–1058. doi: 10.1364/OE.18.001049.

Ruska, H. (1940) 'Die Sichtbarmachung der bakteriophagen Lyse im Übermikroskop', *Die Naturwissenschaften*. Springer-Verlag, 28(3), pp. 45–46. doi: 10.1007/BF01486931.

Rust, M. J., Bates, M. and Zhuang, X. (2006) 'Sub-diffraction-limit imaging by stochastic optical reconstruction microscopy (STORM).', *Nature methods*. NIH Public Access, 3(10), pp. 793–5. doi: 10.1038/nmeth929.

Saal, K. A. *et al.* (2023) 'Heat denaturation enables multicolor X10-STED microscopy', *Scientific Reports 2023 13:1*. Nature Publishing Group, 13(1), pp. 1–15. doi: 10.1038/s41598-023-32524-5.

Sarkar, D. *et al.* (2022) 'Revealing nanostructures in brain tissue via protein decrowding by iterative expansion microscopy', *Nature Biomedical Engineering*. Nature Research, 6(9), pp. 1057–1073. doi: 10.1038/s41551-022-00912-3.

Scheible, M. B. and Tinnefeld, P. (2018) 'Quantifying Expansion Microscopy with DNA Origami Expansion Nanorulers', *bioRxiv*. doi: 10.1101/265405.

Schindelin, J. *et al.* (2012) 'Fiji: an open-source platform for biological-image analysis', *Nature Methods 2012 9:7*. Nature Publishing Group, 9(7), pp. 676–682. doi: 10.1038/nmeth.2019.

Schnell, U. *et al.* (2012) 'Immunolabeling artifacts and the need for live-cell imaging', *Nature Methods 2012 9:2*. Nature Publishing Group, 9(2), pp. 152–158. doi: 10.1038/nmeth.1855.

Seehra, R. S. *et al.* (2023) 'Geometry-preserving Expansion Microscopy microplates enable high fidelity nanoscale distortion mapping', *bioRxiv*. Cold Spring Harbor Laboratory. doi: 10.1101/2023.02.20.529230.

Shaib, A. H. *et al.* (2022) 'Expansion microscopy at one nanometer resolution', *bioRxiv*. Cold Spring Harbor Laboratory. doi: 10.1101/2022.08.03.502284.

Sheard, T. M. D. *et al.* (2019) 'Three-Dimensional and Chemical Mapping of Intracellular Signaling Nanodomains in Health and Disease with Enhanced Expansion Microscopy', *ACS Nano*. American Chemical Society, 13(2), p. acsnano.8b08742. doi: 10.1021/acsnano.8b08742.

Shi, X. *et al.* (2019) 'Label-retention expansion microscopy', *bioRxiv*. Cold Spring Harbor Laboratory. doi: 10.1101/687954.

Sim, J. *et al.* (2022) 'Nanoscale resolution imaging of the whole mouse embryos and larval zebrafish using expansion microscopy', *bioRxiv*. Cold Spring Harbor Laboratory. doi: 10.1101/2021.05.18.443629.

Steib, E. *et al.* (2022) 'TissUExM enables quantitative ultrastructural analysis in whole vertebrate embryos by expansion microscopy', *Cell Reports Methods*, 2, p. 100311. doi: 10.1016/j.crmeth.2022.100311.

Sun, D. en *et al.* (2021) 'Click-ExM enables expansion microscopy for all biomolecules', *Nature Methods*. Nature Research, 18(1), pp. 107–113. doi: 10.1038/s41592-020-01005-2.

Thevathasan, J. V. *et al.* (2019) 'Nuclear pores as versatile reference standards for quantitative superresolution microscopy', *Nature Methods*. Nature Publishing Group, 16(10), pp. 1045–1053. doi: 10.1038/s41592-019-0574-9.

Thielhorn, R. *et al.* (2023) 'Controlled Grafting Expansion Microscopy', *Angewandte Chemie International Edition*. Angew Chem Int Ed Engl, 62(28). doi: 10.1002/anie.202302318.

Tillberg, P. W. *et al.* (2016) 'Protein-retention expansion microscopy of cells and tissues labeled using standard fluorescent proteins and antibodies', *Nature Biotechnology*, 34(9), pp. 987–992. doi: 10.1038/nbt.3625.

Truckenbrodt, S. *et al.* (2018) 'X10 expansion microscopy enables 25-nm resolution on conventional microscopes', *EMBO reports*. John Wiley & Sons, Ltd, 19, pp. 1–12. doi: 10.15252/embr.201845836.

Truckenbrodt, S. *et al.* (2019) 'A practical guide to optimization in X10 expansion microscopy', *Nature Protocols*. Springer US, 14(3), pp. 832–863. doi: 10.1038/s41596-018-0117-3.

Unnersjö-Jess, D. *et al.* (2016a) 'Super-resolution stimulated emission depletion imaging of slit diaphragm proteins in optically cleared kidney tissue', *Kidney International*. Elsevier B.V., 89(1), pp. 243–247. doi: 10.1038/ki.2015.308.

Unnersjö-Jess, D. *et al.* (2016b) 'Super-resolution stimulated emission depletion imaging of slit diaphragm proteins in optically cleared kidney tissue', *Kidney International*. doi: 10.1038/ki.2015.308.

Vanheusden, M. *et al.* (2020) 'Fluorescence Photobleaching as an Intrinsic Tool to Quantify the 3D Expansion Factor of Biological Samples in Expansion Microscopy', *ACS Omega*. American Chemical Society, 5(12), pp. 6792–6799. doi: 10.1021/acsomega.0c00118.

Wang, G., Moffitt, J. R. and Zhuang, X. (2018) 'Multiplexed imaging of high-density libraries of RNAs with MERFISH and expansion microscopy', *Scientific Reports 2018 8:1*. Nature Publishing Group, 8(1), pp. 1–13. doi: 10.1038/s41598-018-22297-7.

Wen, G. *et al.* (2020) 'Evaluation of Direct Grafting Strategies via Trivalent Anchoring for Enabling Lipid Membrane and Cytoskeleton Staining in Expansion Microscopy', *ACS Nano*. American Chemical Society, 14(7), pp. 7860–7867. doi: 10.1021/acsnano.9b09259.

Wen, G. *et al.* (2022) 'Improved Dye Survival in Expansion Microscopy through Stabilizer-Conjugated Linkers', *Chemistry – A European Journal*. Wiley, p. e202202404. doi: 10.1002/chem.202202404.

Wen, G. *et al.* (2023) 'Trifunctional Linkers Enable Improved Visualization of Actin by Expansion Microscopy', *ACS Nano*. American Chemical Society. doi: 10.1021/ACSNANO.3C07510.

Westphal, V. and Hell, S. W. (2005) 'Nanoscale Resolution in the Focal Plane of an Optical Microscope', *Physical Review Letters*. American Physical Society, 94(14), p. 143903. doi: 10.1103/PhysRevLett.94.143903.

White, B. M. *et al.* (2022) 'Lipid Expansion Microscopy', *Journal of the American Chemical Society*. American Chemical Society, 144(40), pp. 18212–18217. doi: 10.1021/jacs.2c03743.

Wiedenmann, J. *et al.* (2004) 'EosFP, a fluorescent marker protein with UV-inducible green-to-red fluorescence conversion', *Proceedings of the National Academy of Sciences of the United States of America*. National Academy of Sciences, 101(45), p. 15905. doi: 10.1073/PNAS.0403668101.

Wildanger, D. *et al.* (2009) 'A compact STED microscope providing 3D nanoscale resolution', *Journal of Microscopy*, 236(1), pp. 35–43. doi: 10.1111/j.1365-2818.2009.03188.x.

Winey, M. *et al.* (1997) 'Nuclear Pore Complex Number and Distribution throughout the Saccharomyces cerevisiae Cell Cycle by Three-Dimensional Reconstruction from Electron Micrographs of Nuclear Envelopes', *Molecular Biology of the Cell*. American Society for Cell Biology, 8(11), p. 2119. doi: 10.1091/MBC.8.11.2119.

Xie, J. *et al.* (2023) 'An Image-Based High-Throughput and High-Content Drug Screening Method Based on Microarray and Expansion Microscopy', *ACS Nano*. American Chemical Society, 17(16), pp. 15516–15528. doi: 10.1021/acsnano.3c01865.

Yao, L. *et al.* (2021) 'Application of SNAP-Tag in Expansion Super-Resolution Microscopy Using DNA Oligostrands', *Frontiers in Chemistry*. Frontiers Media SA, 9, p. 303. doi: 10.3389/fchem.2021.640519.

Yu, C. C. *et al.* (2020) 'Expansion microscopy of c. Elegans', *eLife*. eLife Sciences Publications Ltd, 9, pp. 1–78. doi: 10.7554/eLife.46249.

Zaitlin, M. and Palukaitis, P. (2000) 'Advances in Understanding Plant Viruses and Virus Diseases', *Annual review of phytopathology*. Annu Rev Phytopathol, 38, pp. 117–143. doi: 10.1146/ANNUREV.PHYTO.38.1.117.

Zdankowski, P. *et al.* (2019) 'Numerically enhanced adaptive optics-based 3D STED microscopy for deep-tissue super-resolved imaging', *bioRxiv*. Cold Spring Harbor Laboratory. doi: 10.1101/653394.

Zhao, Y. *et al.* (2017) 'Nanoscale imaging of clinical specimens using pathology-optimized expansion microscopy', *Nature Biotechnology*. Nature Publishing Group, 35(8), pp. 757–764. doi: 10.1038/nbt.3892.

Zohuriaan-Mehr, M. J. and Kabiri, K. (2008) 'Superabsorbent Polymer Materials: A Review', *Iranian Polymer Journal*, 17(6), pp. 451–477.

Zwettler, F. U. *et al.* (2020) 'Molecular resolution imaging by post-labeling expansion single-molecule localization microscopy (Ex-SMLM)', *Nature Communications*. Nature Publishing Group, 11(1), p. 3388. doi: 10.1038/s41467-020-17086-8.

List of publications

Gao, M., **Thielhorn, R**. et al. (2021) 'Expansion STED microscopy (ExSTED)', *Methods in cell biology*. Methods Cell Biol, 161, pp. 15–31. doi: 10.1016/BS.MCB.2020.06.001.

Thielhorn, R., Heing-Becker I. et al. (2023) 'Controlled Grafting Expansion Microscopy', *Angewandte Chemie (International ed. in English).* Angew Chem Int Ed Engl, 62(28). doi: 10.1002/ANIE.202302318.

Hümpfer, N., **Thielhorn, R.**, Ewers, H., 'Expanding boundaries, a cell biologist's guide to expansion microscopy', under review at *Journal of Cell Science.* JCS.

Appendix

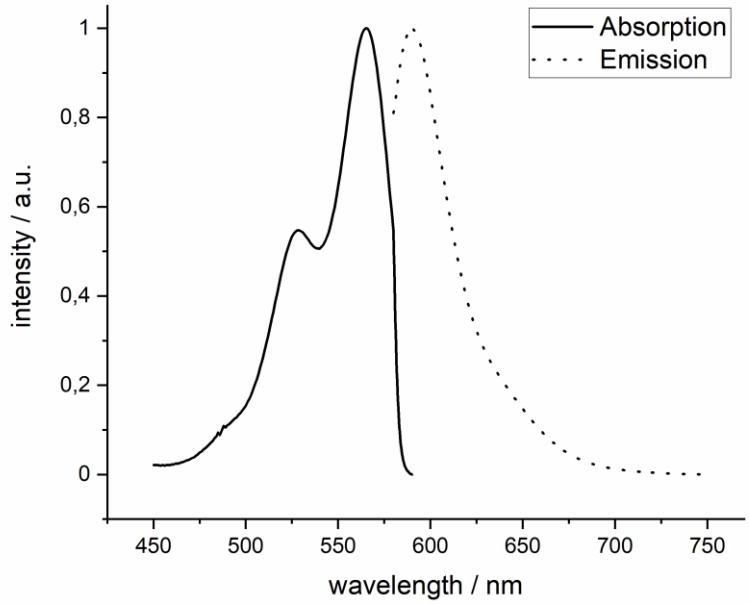

Figure S 1: Absorption and emission spectrum of BG-TMR-Boc in water.

The product absorbs at 565 nm and emits at 590 nm. Reprinted with permission from Thielhorn *et al.*, 2023.

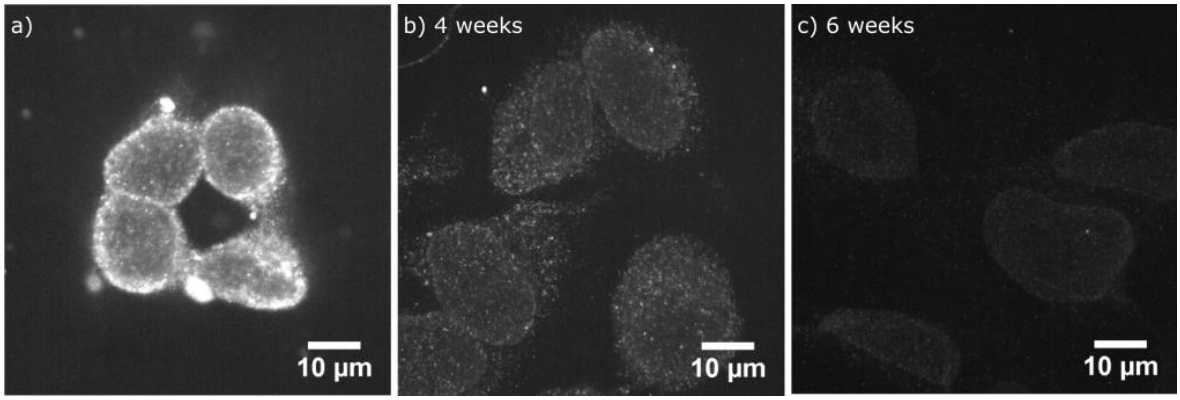

Figure S 2: Loss of signal intensity of BG-TMR-acrylate dependent on storage time.

Nuclear pores stained with BG-TMR-acrylate after a) synthesis of dye, b) 4 weeks of storage and c) 6 weeks of storage. Imaging was performed after gelation. Scale bars are 10 µm.

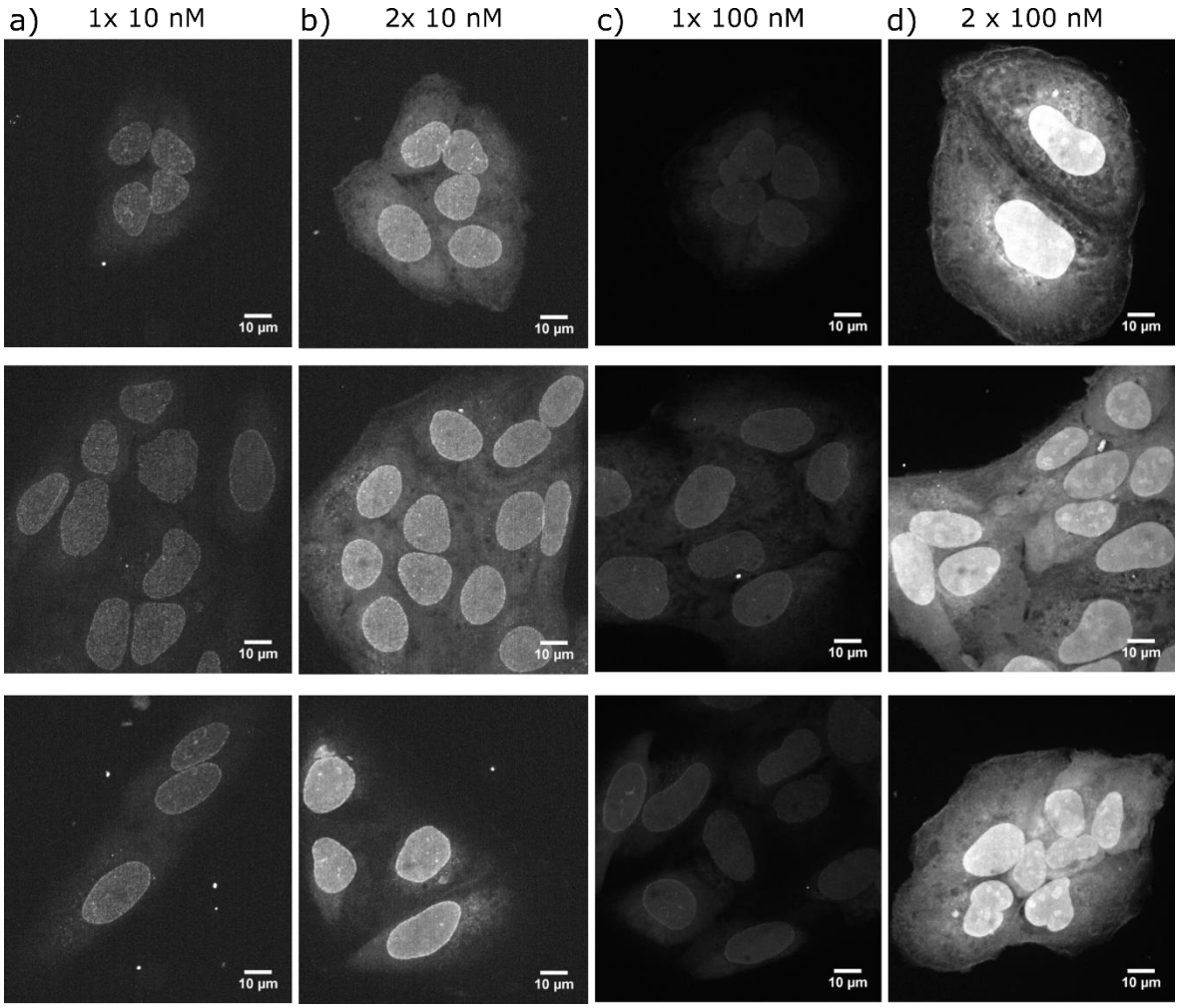

Figure S 3: Successive staining with BG-TMR-acrylate.

Successive staining with BG-TMR-acrylate to optimize staining conditions. a) Nuclear pores stained with 10 nM BG-TMR-acrylate once. b) Nuclear pores stained with 10 nM BG-TMR-acrylate twice. c) Nuclear pores stained with 100 nM BG-TMR-acrylate once. d) Nuclear pores stained with 100 nM BG-TMR-acrylate twice. Second and third row: images of different cells stained under the same conditions. Same intensity scaling for a) and b) as well as for c) and d). Scale bars are 10 µm.

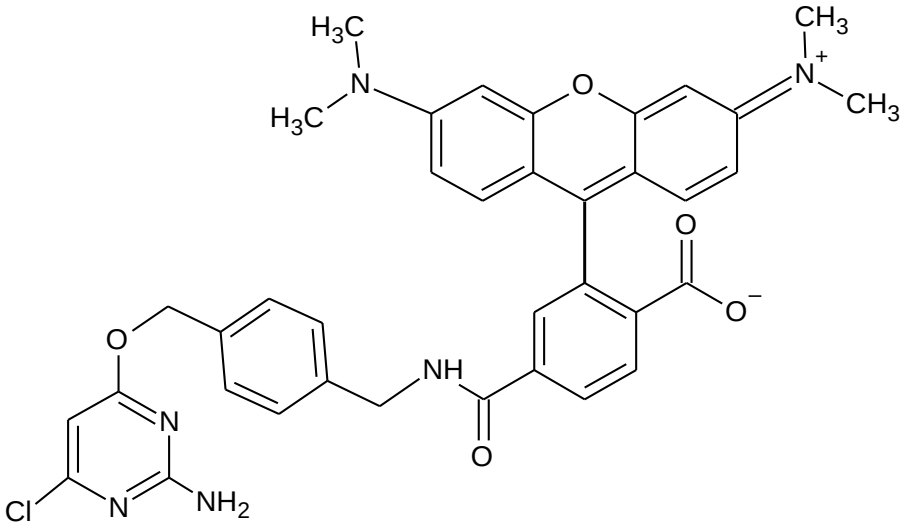

Figure S 4: Structure of SNAP-Cell TMR-Star.

SNAP-Cell TMR-Star consists of a TMR core with an amino chloropyrimidine group instead of benzylguanine.

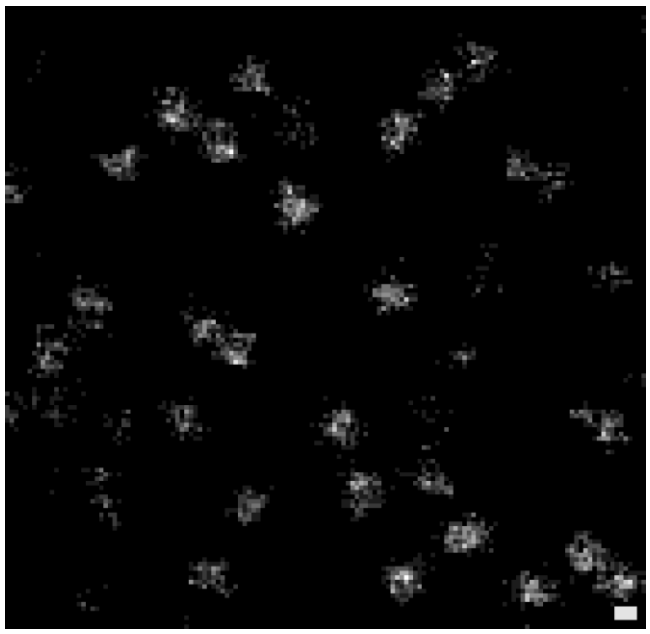

Figure S 5: STED of nuclear pores stained with BG-TMR-MA.

STED imaging of a NUP96-SNAP expressing cell labeled with BG-TMR-MA. Scale bar is 100 nm.

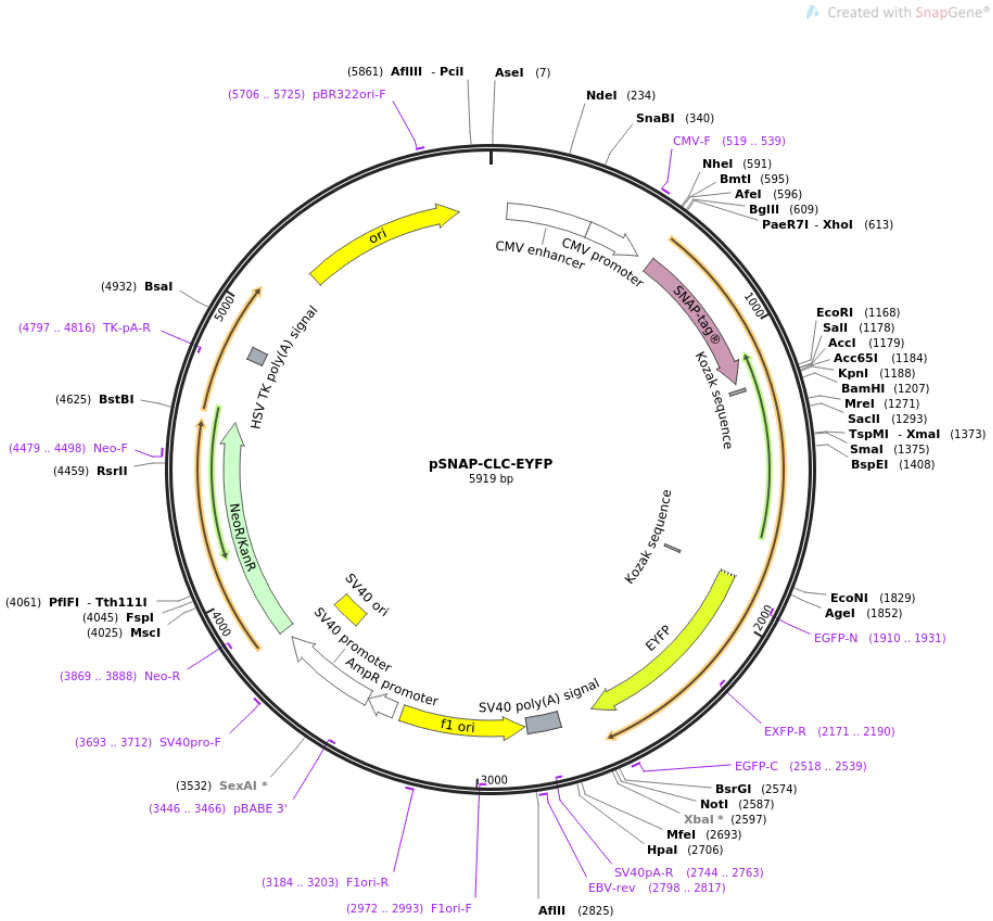

Figure S 6: Plasmid map of SNAP-CLC-YFP.

Plasmid map of SNAP-CLC-YFP. Reprinted from Addgene (https://www.addgene.org/38011/), plasmid #38011 (Jones *et al.*, 2011).

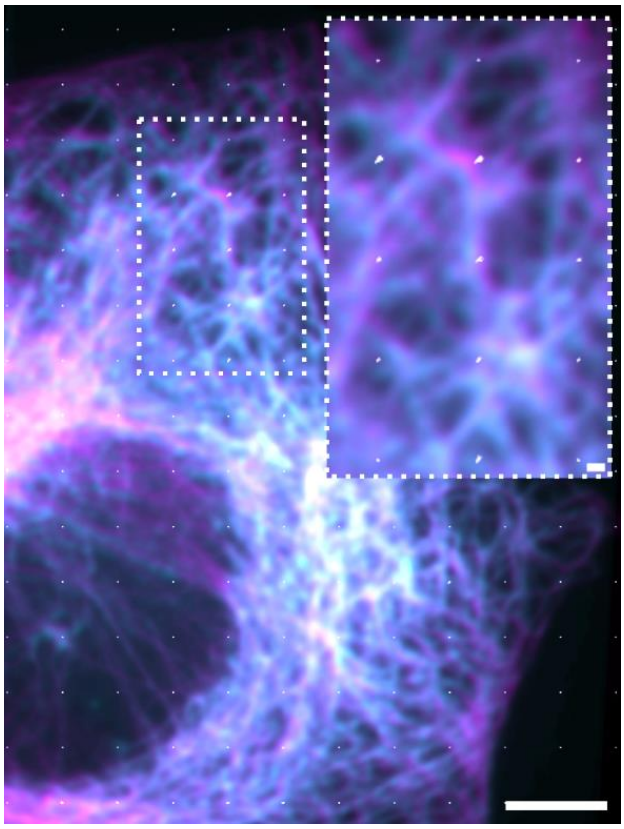

Figure S 7: Deformation vector map.

Overlay of pre and post ExM fluorescence micrographs of the same cell stained against microtubules. Immunostaining against microtubules with primary anti-alpha and anti-beta-tubulin antibodies, which were detected with a secondary anti-mouse Abberior Star Red antibody. The zoom-in box highlights the overlaid deformation vector map, showing the regions most affected by distortion, indicated by the size of the white arrows. Scale bar is 10 µm.

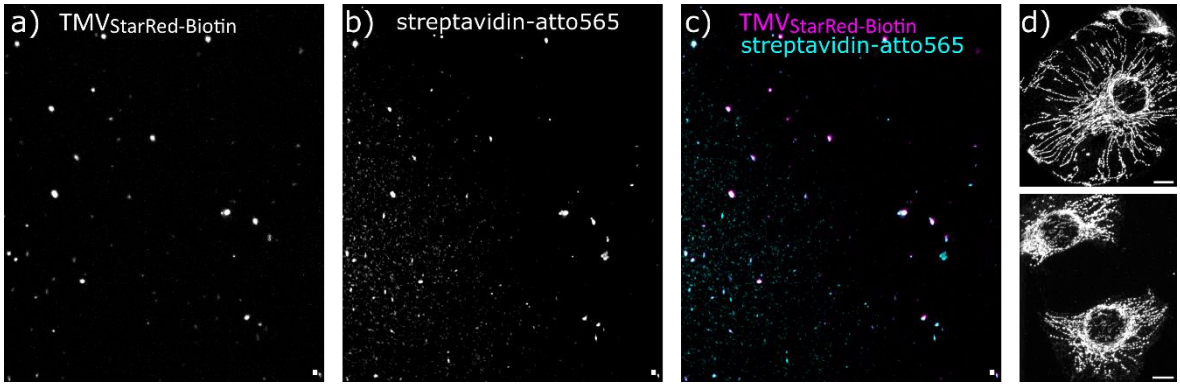

Figure S 8: Biotinylation control of $TMV_{StarRed}$ and anti-beta-tubulin antibodies.

a) Fluorescence micrograph of $TMV_{StarRed\text{-}Biotin}$ particles on a poly-L-lysine coated coverslip. b) Fluorescence micrograph of atto565-conjugated streptavidin binding to $TMV_{StarRed\text{-}Biotin}$. c) Overlay of a) and b) with $TMV_{StarRed\text{-}Biotin}$ shown in magenta and streptavidin-atto565 shown in cyan. d) Fluorescence micrograph of microtubules stained with biotinylated anti-beta-tubulin antibodies and detected with streptavidin-atto565. Scale bars are 1 µm (a-c) and 10 µm (d).

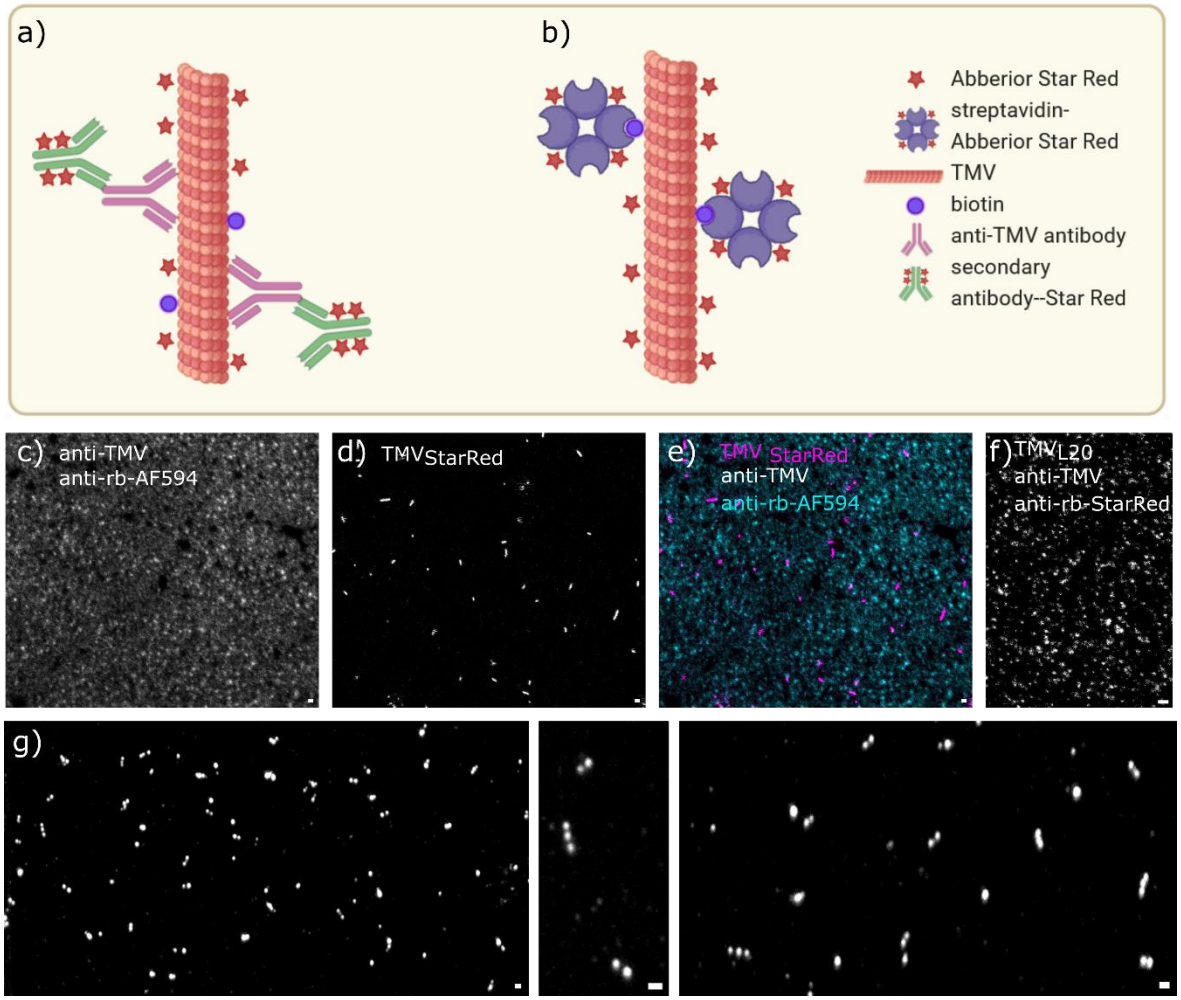

Figure S 9: Approaches to increase TMV labeling density.

a) Schematic showing labeling of biotinylated $TMV_{StarRed}$ particle with primary anti-TMV antibodies and secondary anti-rabbit Abberior Star Red antibodies. b) Schematic showing labeling of biotinylated $TMV_{StarRed}$ particle with streptavidin coupled to Abberior Star Red. c) STED imaging of TMV particles labeled with primary anti-TMV antibodies and secondary anti-rabbit-AF594 antibodies on cover glass. d) $TMV_{StarRed}$ signal of the same region of interest as in c). e) Overlay of image c) and d), which highlights that TMV antibodies do not bind specifically. f) STED imaging of unlabeled TMV_{Lys} particles using primary anti-TMV and secondary anti-rabbit Abberior Star Red antibodies revealed only unspecific signal with no TMV rods observed. g) Post ExM spinning disc imaging of $TMV_{StarRed}$ particles labeled with streptavidin coupled to Abberior Star Red showed discontinuous signal of TMV rods. Scale bars are 300 nm.

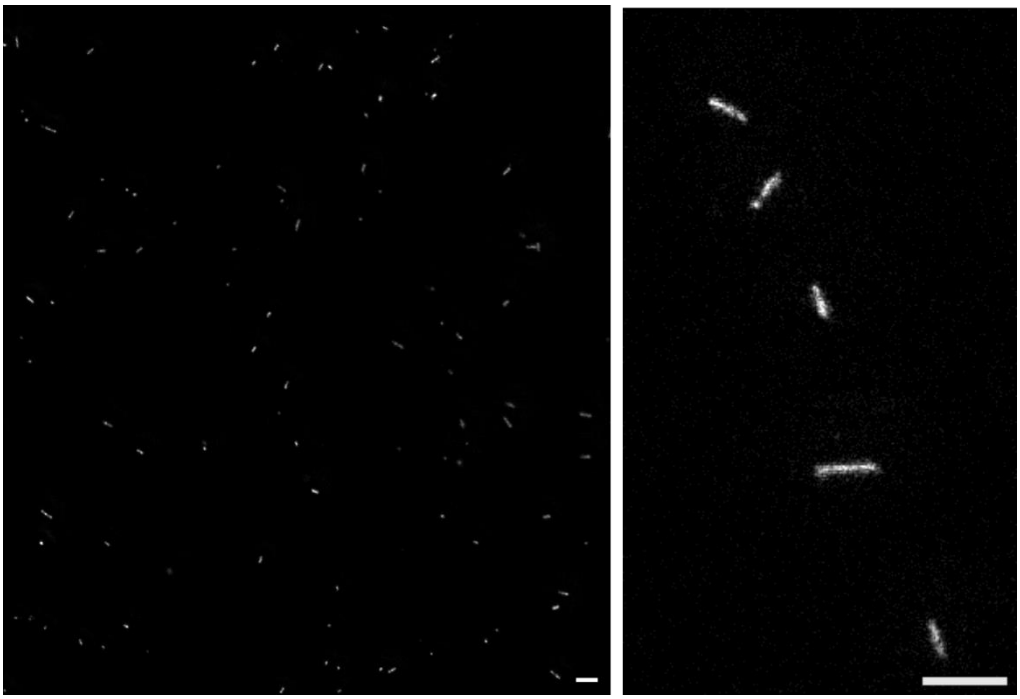

Figure S 10: ExSTED imaging of $TMV_{StarRed}$ after mild digestion.

STED imaging of expanded $TMV_{StarRed}$ particles on cover glass after a mild digestion step with proteinase K diluted 10-fold higher than usual (0.8 U/mL). Anchoring was performed with 0.25% GA. A zoomed-in image on the right emphasizes the improved signal continuity of TMV rods. Scale bars are 300 nm.

Acknowledgements

Firstly, I would like to express my gratitude to my first supervisor Prof. Dr. Helge Ewers for the opportunity to work on this project and the continuous support, immense knowledge and constructive criticism.

I thank Prof. Dr. Francesca Bottanelli, for being my second reviewer.

I would like to thank my collaborators from Prof. Dr. Rainer Haag´s group, especially Isabelle, for synthesizing the trifunctional dye that was essential to the success of the project.

I am grateful to Prof. Dr. Christina Wege for sharing TMV particles.

Thanks to Jakob for scientific discussions and for being one of my best friends and lab collegue since our Bachelor studies. Raluca and Nadja for support and helpful discussions. Andrea and Maria-Anna for technical support during my pregnancy. Iwona for performing TEM imaging. Mengfei and Ella for giving me an introduction into Expansion Microscopy. Valentin for advice in nanobody labeling. And all laboratory members of the Ewers group for helpful discussions and technical support.

Thanks to all proofreaders of this dissertation.

Last but not least, I would like to thank my family and friends for helping and encouraging me throughout the years.